A study on an interaction between an upper-layer eddy and a bottom topography using a quasi-geostrophic model

(準地衡流モデルを用いた上層の渦と海底地形の相互作用に関する研究)

Takaaki Takeuchi

Graduate School of Environmental Science,
Hokkaido University

February 2023

Abstract

This study aims to understand the fundamental aspects of the interactions between mesoscale eddies and bottom topography using the quasi-geostrophic approximation.

First, the interaction between an upper-layer vortex and a bottom topography is investigated using an f-plane two-layer quasi-geostrophic model with a point vortex and step-like topography. The contour dynamics method is used to formulate the model. A steadily propagating linear solution along the topography, known as the pseudo-image solution, is derived analytically for a weak point vortex, and the nonlinear solution is obtained numerically. The numerical experiments show that the nonlinear pseudo-image solution collapses with time, with saddle-node points in the velocity field playing a critical role in this collapse. Even after the collapse, the point vortex propagates along the topography similarly to that in the steadily propagating solution. Numerical experiments with various initial conditions show that the point vortex has two types of motion in this system: motion along the topography and motion away from the topography. In the latter case, the point vortex and lower-layer potential vorticity anomaly form a heton-like dipole structure. Moreover, the motion classification results show that an anticyclonic (cyclonic) point vortex on the deeper (shallower) side is more likely to form a dipole structure than a cyclonic (anticyclonic) vortex on the deeper (shallower) side when its initial distance from the topography is the same.

Second, we examine the influence of the finite width of the topography and the β-effect on the interactions between an upper-layer eddy and a bottom topography using the two-layer quasi-geostrophic model with a Gaussian eddy in the upper layer and sloping topography. In the f-plane, anticyclonic (cyclonic) eddies initially move along the topography in the opposite (same) direction of the topographic Rossby wave. As time elapses, the anticyclonic eddies move away from the topography even when their strength is small, whereas the cyclonic eddies continue to move along the topography even when their strength is large. These results suggest that in the f-plane, the formation of a heton-like dipole is a common phenomenon in the case of anticyclonic eddies, while an isolated eddy in the lower layer cannot strongly interact with the upper-layer eddies in the case of cyclonic eddies. In the β-plane, anticyclonic eddies move westward onto the sloping topography when their strength is small or the β-effect is large, whereas when their strength is large or the β-effect is small, they move eastward, forming the heton-like dipole. In contrast to the case of the f-plane, the dipole can move eastward long distances in the β-plane. Meanwhile, the cyclonic eddies move westward onto the topography independent of their strength. These results show that the presence of the β-effect prevents the upper-layer eddy from interacting with the bottom topography and enables the dipole moving eastward to move a long distance.

Contents

Chapter 1

Introduction

1.1 Background and observations

Ocean mesoscale eddies play an essential role in water exchange and material circulation. The motion of these eddies is affected by background currents, advection due to other eddies, and the presence of topography. In particular, mesoscale ocean eddies in open ocean largely propagate westward due to the β-effect (Chelton et al., 2011). As a result of this westward motion, the eddies reach the western boundary, and eventually interact with the western bottom topography, such as continental shelves, slopes, and rise. Since oceanic eddies transport momentum, heat, and water masses, investigating their behaviour is essential for understanding the ocean environment and its variability in the western region (Spall et al., 2008; Chelton et al., 2011; Baird and Ridgway, 2012; Dong et al., 2014). Moreover, western ocean regions have distinct topography, including continental shelves/slopes. Since distinct topography can play an essential role in the evolution of eddies, investigating the interactions between eddies and topography is critical for understanding the material transport via the movement of eddies (Spall et al., 2008; Itoh and Yasuda, 2010; Ribbe et al., 2018).

In the Kuroshio extension region, warm-core rings are frequently detached from the Kuroshio extension. Hence, many previous studies have examined the movement of warm-core rings. For example, Yasuda et al. (1992) observed the northward movement along an isobath line. Itoh and Sugimoto (2001) suggested that this movement is caused by the steep topography. Other studies (e.g., Lutjeharms and Roberts, 1988; Everett et al., 2012) pointed out that since eddies moving poleward along the topography are widely observed, this is a typical motion of eddies near the topography.

The dipole structures are observed in the global ocean (Ni et al., 2020). In the open ocean, eddies largely propagate west due to the β-effect; once eddies reach the western boundary, they typically move along that boundary as if they are trapped. However, there is an eastward-propagating solution with a dipole structure. This type of structure is known as a modon (Stern, 1975; Flierl et al., 1980). Using satellite altimeter data, Hughes and Miller (2017) recently observed modons moving eastward in the Tasman Sea and suggested that the bottom topography could play an important role in the formation process (figure 1.1). While a modon is a solution consisting of two vortices in the same density layer, a dipole structure with eddies in different layers is also possible. This type of structure is known as a heton (Hogg and Stommel, 1985). Since hetons have high heat and material transport capabilities, they are thought to be significant structures in the ocean (Richardson and Tychensky, 1998; Morel and McWilliams, 2001; Serra and Ambar, 2002; Carton et al., 2010; Serra et al., 2010).

1.2 Previous studies

The Mid-Ocean Dynamics Experiment (MODE) showed that a large number of energetic eddies exist in the ocean interior (MODE Group, 1978). Since then,

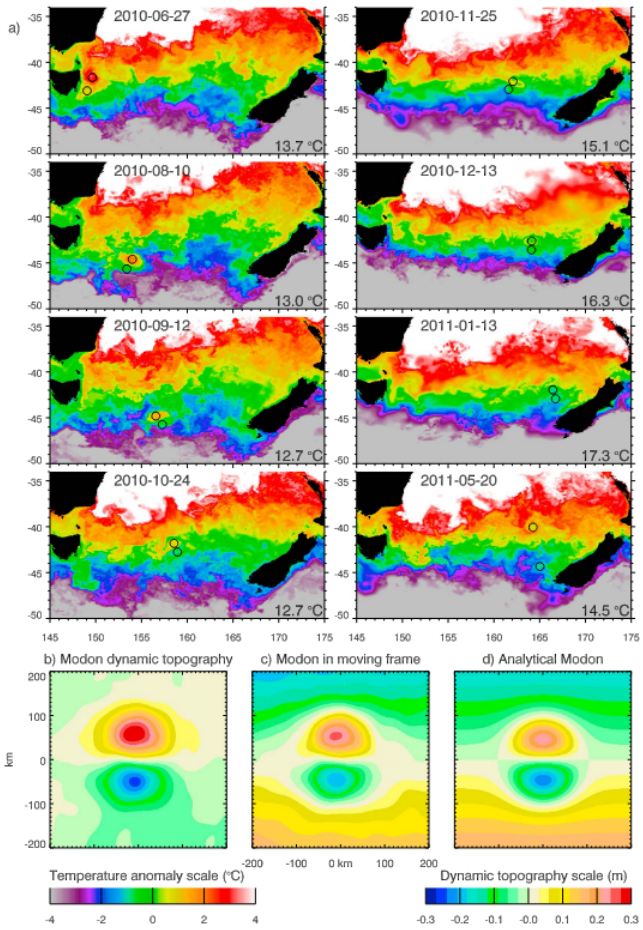

Fig. 1.1: (a) Sea surface temperature. Black circles mark the modon position. Temperatures are shown relative to the median value, which is written on each plot. (b) The mean sea level structure of this modon from along-track altimetry. (c) As in Figure b but with a north-south slope added so that contours represent the flow relative to the modon. (d) The analytical modon solution that best fits the observations. (From Hughes and Miller, 2017)

numerous studies have investigated the behaviour of isolated eddies. Additionally, researchers identified some of the important properties of mesoscale eddies; for example, they propagate westwards due to the β-effect, have an isolated structure, and are strongly nonlinear and highly baroclinic. McWilliams and Flierl (1979) investigated the influence of the planetary β and nonlinear effects on the behaviour of an isolated eddy. Their results showed that anticyclonic eddies propagate southwestward due to the combination of these effects, and that the nonlinear effect suppresses dispersion of the eddies due to the Rossby waves. Using a two-layer primitive model, Mied and Lindemann (1979) verified these results.

To explain the fact that there are many eddies in the ocean interior, as revealed by the MODE, Stern (1975) developed an exact nonlinear solution with a steady dipole structure on a barotropic β-plane. This solution results from the balance between the dispersion due to the linear Rossby waves and the nonlinear advective steepening. Stern (1975) referred to this solution as the modon. Moreover, Flierl et al. (1980) derived the nonlinear solutions to the quasi-geostrophic two-layer equations to extend this solution to include baroclinic effects and showed the existence of rider perturbations upon these solutions. Verkley (1984) demonstrated the barotropic modon solutions on a sphere. Further, other studies investigated the behaviour of modons in various systems using numerical experiments (e.g., McWilliams et al., 1981; McWilliams and Zabusky, 1982; Kizner et al., 2003; Lahaye and Zeitlin, 2012).

Hogg and Stommel (1985) investigated the behaviour of dipole structures with opposite-signed eddies in different layers using the two-layer model. Focusing on the ability of this dipole to transfer heat, they referred to this structure as a heton. For example, in situations where the hydrostatic and geostrophic approximations hold, both an anticyclonic eddy in the upper layer and a cyclonic eddy in the lower layer dent the interface between the layers downwards. If the upper layer is warmer

than the lower layer, the heat in the area containing these eddies is higher than that in the surrounding area, and the dipole is called a warm heton. Conversely, the dipole is referred to as a cold heton.

Interactions between eddies and the bottom topography, which represent the focus of this thesis, have been investigated. Smith and O'Brien (1983) studied these interactions using a two-layer primitive model on a β-plane. They showed that the behaviour of barotropic eddies on a sloping bottom topography is additively affected by the planetary and topographic β-effect. Additionally, the anticyclonic eddies are more likely to move away from the topography, whereas the cyclonic eddies are more likely to move onto the sloping topography due to their nonlinear effects. Kamenkovich et al. (1995) observed a similar behaviour of eddies using a model with a steep ridge.

Using primitive equations, Itoh and Sugimoto (2001) numerically reproduced the poleward movement of an eddy that was initially near the topography and found that the effect of the steep bottom slope is an important factor in this motion. They called this effect the equivalent image effect and showed that this effect increases as the slope becomes steeper. Frolov et al. (2004) investigated the interaction between an anticyclonic eddy, which mimics a Loop Current Eddy detached from the Loop Current, and a realistic western topography using a two-layer model on a β-plane and observed the poleward motion of the eddy, as in Itoh and Sugimoto (2001).

Using a one-layer quasi-geostrophic model on an f-plane, Wang (1992) investigated the interaction between a point vortex and a step-like bottom topography and identified the important processes in this interaction, namely the excitation of the topographic wave due to the advection of the point vortex, the formation of a vortex rotating in the opposite direction to the point vortex, and the cross-topography volume transport.

McDonald (1998) and Dunn et al. (2001) investigated the interactions between a point vortex and a step-like topography using a 1.5-layer quasi-geostrophic model. Specifically, McDonald (1998) examined the behaviour of intense point vortices, while Dunn et al. (2001) studied the behaviour of moderate and weak point vortices. Dunn et al. (2001) derived the linear solution within the limit that a point vortex is weak and a moderate point vortex can propagate away from the topography by forming the dipole structure. Other studies have also confirmed these results using various models with a vortex and a step-like topography (Dunn, 2002; Dunn et al., 2002; White and McDonald, 2004).

1.3 Outline of thesis

Previous studies using the idealised model with a point vortex and a step-like bottom topography have focused solely on situations in which vortices are located in the same layer as the topography. Moreover, in previous studies using a two-layer primitive model, the details of the formation mechanism underlying the motion caused by interactions between an upper-layer eddy and a bottom topography are not clear. Therefore, the aim of this study is to establish a comprehensive framework for understanding the interactions between upper-layer eddies and the steep bottom topography.

The remainder of this thesis is structured as follows. In chapter 2, we use a two-layer quasi-geostrophic model in an f-plane, with a point vortex in the upper layer and a step-like topography in the lower layer. In chapter 3, we use a two-layer quasi-geostrophic model in a β-plane, with a Gaussian eddy in the upper layer and a sloping bottom topography. The summary of this thesis is presented in chapter 4.

Chapter 2

Point Vortex and Step-like Topography Interactions

2.1 Introduction

Interactions between Oceanic eddies and bottom topography seem complex due to the deformation of eddies and topographic complexity such as an irregular continental slope/shelf shape. In this chapter, we simplify the problem as interactions between a point vortex in the upper layer and a step-like topography in the lower layer, to clarify a fundamental behavior in this system. An infinitely long and straight escarpment is adopted in this model as the bottom topography. When the fluid is at rest, a potential vorticity front is along the topography, and the displacement of this front from the topography generates relative vorticity due to the potential vorticity conservation. Since the flow field in this system is determined only by the point vortex and the displacement of this front, we investigate interactions between the point vortex and the potential vorticity front in this chapter.

The models close to our system are that of Wang (1992), McDonald (1998), and Dunn et al. (2001). Especially, McDonald (1998) and Dunn et al. (2001) studied

the motion of a point vortex near a step-like topography in a 1.5-layer quasi-geostrophic model in the f-plane. McDonald (1998) found that intense vortices cause a potential vorticity front, which is located along the topography, to wrap around themselves. They defined an intense vortex as one in which the time scale for vortex circulation, T_a, is much shorter than the time scale for topographic wave generation, T_w. Dunn et al. (2001) investigated moderate, $T_w \approx T_a$, and weak, $T_w \ll T_a$, point vortices. They found that a moderate vortex forms a dipole structure consisting of a point vortex and the vortex caused by potential vorticity conservation, while a weak vortex propagates steadily along the topography. They analytically showed that a weak vortex propagates parallel to the topography. They referred to this phenomenon as the pseudoimage of the vortex and derived its linear solution. Other studies have also confirmed that the interaction of a vortex with a step-like topography causes propagating vortices along the topography and the formation of dipole structures (Dunn 2002; Dunn et al. 2002; White and McDonald 2004). In this chapter, to investigate the behavior of our system, we use a non-dimensional circulation of the point vortex, equivalent to the ratio of T_a to T_w in the previous studies. Moreover, since it is reasonable to hypothesize that the distance between the topography and the vortex is an important parameter for controlling the system, we use the initial distance between the point vortex and the topography as the parameter

After formulating the problem in section 2.2, we show the analytical results based on linear theory at the limit of a weak point vortex in section 2.3. A finite-amplitude pseudoimage solution is derived in section 2.4. In section 2.5, we numerically investigate the temporal evolution of both the pseudoimage solution and the system. The conclusions are presented in section 2.6.

2.2 Model formulation

2.2.1 Potential vorticity and point vortex equations

In this chapter, we used a two-layer quasi-geostrophic model in the f-plane, with the point vortex in the upper layer and the step-like topography in the lower layer (see figure 2.1). Our model has two layers with an average thickness of H_j and a density of ρ_j, where $j = 1, 2$ denotes the upper and lower layers, respectively. The density in each layer is written in terms of the reference density of the fluid, ρ_0, and the density difference between the two layers, $\Delta\rho$, as $\rho_1 = \rho_0$ and $\rho_2 = \rho_0 + \Delta\rho$. The point vortex in the upper layer has a circulation of Γ and is located at a distance of Y_0 from the topography. In the lower layer, h_B, which denotes the bottom topography, is written as $h_B = -\Delta H \mathrm{sgn}(y)$, where ΔH is the amplitude of the bottom topography and $\mathrm{sgn}(y)$ is the sign function. Assuming that $\Delta H/H_2 \ll 1$, we can use the quasi-geostrophic approximation to formulate this system. The governing equation and the quasi-geostrophic potential vorticity, q_j, in each layer can be written in nondimensional forms as

$$\frac{\partial q_j}{\partial t} + J(\psi_j, q_j) = 0, \tag{2.1}$$

$$q_1 = \nabla^2\psi_1 - \gamma_L\psi_1 - (\psi_1 - \psi_2), \tag{2.2}$$

$$q_2 = \nabla^2\psi_2 + \gamma_H(\psi_1 - \psi_2) + h_B, \tag{2.3}$$

where t is the time, J is the Jacobian, and ψ_j is the streamfunction in the jth layer. The equations in this system were nondimensionalized using the length scale $L = \sqrt{g'H_1}/f$ and the time scale $T = (f\Delta H/H_2)^{-1}$, where g' is the reduced gravity and f is the Coriolis parameter. We scaled the relative vorticity by $T^{-1} = f\Delta H/H_2$ and the stream functions by $L^2T^{-1} = (g'H_1/f)(\Delta H/H_2)$. The nondimensional amplitude of the point vortex circulation is $\varepsilon = |\Gamma|T/L^2 = |\Gamma|f/(g'H_1)/(\Delta H/H_2)$. The remaining nondimensional parameters in the equations are $\gamma_H = H_1/H_2$

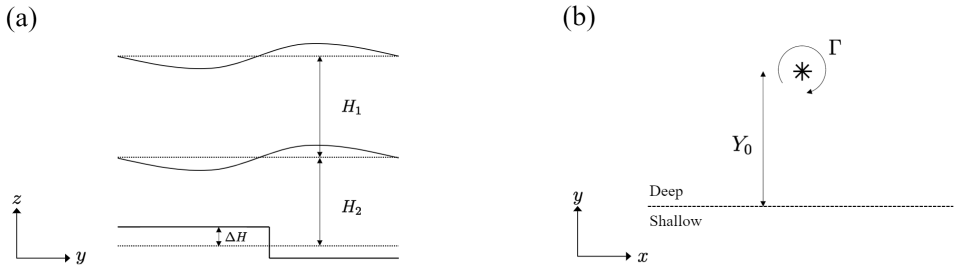

Fig. 2.1: Schematic illustration of the model configuration. (a) The cross-section of the two-layer fluid. (b) The initial condition for this problem. The point vortex indicated by $*$ is located at $y = Y_0$ and has a circulation of Γ.

and $\gamma_L = \Delta\rho/\rho_0$. In addition to these nondimensional parameters, the initial y-coordinate of the point vortex, Y_0, contributes to the behaviour of this system. Y_0 is also nondimensionalized by L. It should be noted that the streamfunction in the jth layer is invariant under the transformation $\psi_j(x, y) \to -\psi_j(x, -y)$.

Our model has a point vortex in the upper layer and a potential vorticity front that initially lies along the step-like topography, $y = 0$, in the lower layer. Based on the locations of the point vortex, $(X(t), Y(t))$, and the potential vorticity front, $y = \eta(t, x)$, we can write the nondimensional potential vorticity in each layer as

$$q_1 = \varepsilon \mathrm{sgn}(\Gamma)\delta(x - X, y - Y), \tag{2.4}$$

$$q_2 = -\mathrm{sgn}(y - \eta). \tag{2.5}$$

The velocity caused by the topography can be determined based on the potential vorticity anomaly in the lower layer, Δq_2. This anomaly occurs because of the displacement between the potential vorticity front and the topography and is given

by

$$\Delta q_2 = \begin{cases} +2, & 0 < y < \eta \\ -2, & \eta < y < 0 \\ 0, & \text{otherwise} \end{cases} . \tag{2.6}$$

In terms of $\eta(t,x)$, $X(t)$ and $Y(t)$, the governing equation in this system can be written as,

$$\frac{\partial \eta}{\partial t} + u_2(t,x,\eta)\frac{\partial \eta}{\partial x} = v_2(t,x,\eta), \tag{2.7}$$

$$\frac{\mathrm{d}X}{\mathrm{d}t} = u_1(t,X,Y), \quad \frac{\mathrm{d}Y}{\mathrm{d}t} = v_1(t,X,Y), \tag{2.8}$$

where u_j and v_j are the horizontal components of the velocity and are given by

$$u_j = -\frac{\partial \psi_j}{\partial y}, \qquad v_j = \frac{\partial \psi_j}{\partial x}. \tag{2.9}$$

The streamfunction is determined by the equations

$$\nabla^2 \begin{pmatrix} \psi_1 \\ \psi_2 \end{pmatrix} - M \begin{pmatrix} \psi_1 \\ \psi_2 \end{pmatrix} = \begin{pmatrix} \varepsilon \mathrm{sgn}(\Gamma)\delta(x-X, y-Y) \\ \Delta q_2 \end{pmatrix}, \tag{2.10}$$

written in vector form, where the coefficient matrix, M, can be written as

$$M = \begin{pmatrix} \gamma_L + 1 & -1 \\ -\gamma_H & \gamma_H \end{pmatrix}. \tag{2.11}$$

2.2.2 Vertical mode decomposition

The steamfunctions in each layer can be decomposed into vertical modes. The eigenvalues and eigenvectors of M are denoted by $\lambda_\pm$ and $\overrightarrow{V}_\pm = (U_\pm, V_\pm)$, which can be written as

$$\lambda_\pm = \frac{1 + \gamma_L + \gamma_H \pm \sqrt{(1+\gamma_L+\gamma_H)^2 - 4\gamma_H\gamma_L}}{2}, \tag{2.12}$$

$$\overrightarrow{V}_\pm = (U_\pm, V_\pm) = \left(1, \frac{1+\gamma_L-\lambda_\pm}{\gamma_H}\right). \tag{2.13}$$

We note that the quantities $\lambda_+^{-1/2}$ and $\lambda_-^{-1/2}$ correspond to the nondimensional internal and external Rossby radii of deformation, respectively. We can define the streamfunctions of the + and − modes as

$$\psi_\pm = U_\pm \psi_1 + V_\pm \psi_2. \tag{2.14}$$

By substituting (2.14) into (2.10) and using Green's function, we can write $\psi_\pm$ as

$$\psi_\pm(t,x,y) = U_\pm \varepsilon \mathrm{sgn}(\Gamma) G_\pm(x,X,y,Y) + 2V_\pm \int_{-\infty}^{\infty} \mathrm{d}x' \int_0^{\eta(t,x')} \mathrm{d}y' G_\pm(x,x',y,y'), \tag{2.15}$$

where Green's function in each mode, $G_\pm$, is given by

$$G_\pm(x,x',y,y') = -\frac{1}{2\pi} K_0\left(\sqrt{\lambda_\pm}\sqrt{(x-x')^2+(y-y')^2}\right). \tag{2.16}$$

The streamfunction in each layer, ψ_j, can be obtained from (2.14) and (2.16). We can decompose the streamfunction ψ_j into the point vortex effect, Ψ_j, and the topographic effect, ϕ_j. According to (2.16) and (2.15), the streamfunctions caused by the point vortex can be written as

$$\Psi_1 = \frac{-\varepsilon \mathrm{sgn}(\Gamma)}{V_- - V_+} \left\{V_+ G_-(x,X,y,Y) - V_- G_+(x,X,y,Y)\right\}, \tag{2.17}$$

$$\Psi_2 = \frac{\varepsilon \mathrm{sgn}(\Gamma)}{V_- - V_+} \left\{G_-(x,X,y,Y) - G_+(x,X,y,Y)\right\}, \tag{2.18}$$

while those caused by the topography can be written as

$$\phi_1 = \frac{2V_+V_-}{V_- - V_+} \int_{-\infty}^{\infty} \mathrm{d}x' \int_0^{\eta(t,x')} \mathrm{d}y' \left\{G_-(x,x',y,y') - G_+(x,x',y,y')\right\}, \tag{2.19}$$

$$\phi_2 = \frac{2}{V_- - V_+} \int_{-\infty}^{\infty} \mathrm{d}x' \int_0^{\eta(t,x')} \mathrm{d}y' \left\{V_- G_-(x,x',y,y') - V_+ G_+(x,x',y,y')\right\}, \tag{2.20}$$

where $U_\pm = 1$.

2.2.3 Contour dynamics

The flow field in this system is given by (2.9) and (2.17)-(2.20). The horizontal velocity in the jth layer, $\boldsymbol{u}_j = (u_j, v_j)$, is the sum of the velocity due to the point vortex, $\boldsymbol{u}_j^p$, and the velocity due to the topography, $\boldsymbol{u}_j^t$. According to (2.17) and (2.18), the velocity in the upper layer due to the point vortex can be written as

$$u_1^p(t,x,y) = \frac{\varepsilon \mathrm{sgn}(\Gamma)}{V_- - V_+}\left\{V_+ \frac{\partial G_-}{\partial y}(x,X,y,Y) - V_- \frac{\partial G_+}{\partial y}(x,X,y,Y)\right\}, \tag{2.21}$$

$$v_1^p(t,x,y) = -\frac{\varepsilon \mathrm{sgn}(\Gamma)}{V_- - V_+}\left\{V_+ \frac{\partial G_-}{\partial x}(x,X,y,Y) - V_- \frac{\partial G_+}{\partial x}(x,X,y,Y)\right\}, \tag{2.22}$$

while the velocity in the lower layer due to the point vortex can be written as

$$u_2^p(t,x,y) = -\frac{\varepsilon \mathrm{sgn}(\Gamma)}{V_- - V_+}\left\{\frac{\partial G_-}{\partial y}(x,X,y,Y) - \frac{\partial G_+}{\partial y}(x,X,y,Y)\right\}, \tag{2.23}$$

$$v_2^p(t,x,y) = \frac{\varepsilon \mathrm{sgn}(\Gamma)}{V_- - V_+}\left\{\frac{\partial G_-}{\partial x}(x,X,y,Y) - \frac{\partial G_+}{\partial x}(x,X,y,Y)\right\}. \tag{2.24}$$

According to (2.19) and (2.20), the velocity in the upper layer due to the topography can be written as

$$u_1^t(t,x,y) = \frac{2V_+V_-}{V_- - V_+}\int_{-\infty}^{\infty} \mathrm{d}x' \left\{G_-(x,x',y,\eta) - G_+(x,x',y,\eta) - G_-(x,x',y,0) + G_+(x,x',y,0)\right\} \tag{2.25}$$

$$v_1^t(t,x,y) = \frac{2V_+V_-}{V_- - V_+}\int_{-\infty}^{\infty} \mathrm{d}x' \left\{G_-(x,x',y,\eta) - G_+(x,x',y,\eta)\right\}\frac{\partial \eta}{\partial x'}(t,x'), \tag{2.26}$$

while the velocity in the lower layer due to the topography can be written as

$$u_2^t(t,x,y) = \frac{2}{V_- - V_+}\int_{-\infty}^{\infty} \mathrm{d}x' \left\{V_-G_-(x,x',y,\eta) - V_+G_+(x,x',y,\eta) - V_-G_-(x,x',y,0) + V_+G_+(x,x',y,0)\right\} \tag{2.27}$$

$$v_2^t(t,x,y) = \frac{2}{V_- - V_+}\int_{-\infty}^{\infty} \mathrm{d}x' \left\{V_-G_-(x,x',y,\eta) - V_+G_+(x,x',y,\eta)\right\}\frac{\partial \eta}{\partial x'}(t,x'). \tag{2.28}$$

According to (2.7) and (2.8), we can determine the evolution of the system by using (2.23)-(2.28) to calculate the advection velocity at the front and at the point vortex.

The method of contour dynamics was used in this chapter to calculate the temporal evolution of the system (Zabsusky et al. 1979). The contour dynamics method allows for an accurate treatment of inviscid fluid dynamics and has been used in numerous studies on the interaction between vortices and potential vorticity fronts (Stern and Flierl, 1987; Bell 1989; Wang 1991; McDonald 1998; Dunn et al. 2001; Dunn et al. 2001; Dunn 2002; White and McDonald 2004; Baker-Yeboah et al. 2010; Zhang et al. 2011).

2.3 Linear dynamics and pseudoimage solutions

2.3.1 Linearized equations

If we assume that the displacement of the potential vorticity front is small, $|\eta| \ll 1$, and we maintain $|\eta| \ll 1$, we can also assume that $\varepsilon \leq O(|\eta|)$. Then, the governing equation (2.7) becomes

$$\frac{\partial \eta}{\partial t} = v_2^p(t, x, 0) + v_2^t(t, x, 0), \tag{2.29}$$

where the $O(|\eta|^2)$ terms are neglected. In this approximation, the velocities caused by the topography can be written as

$$u_1^t(t, x, y) = \frac{2V_-V_+}{V_- - V_+} \int_{-\infty}^{\infty} \mathrm{d}x' \left\{ \frac{\partial G_-}{\partial y'}(x, x', y, 0) - \frac{\partial G_+}{\partial y'}(x, x', y, 0) \right\} \eta(t, x'), \tag{2.30}$$

$$v_1^t(t, x, y) = \frac{2V_-V_+}{V_- - V_+} \int_{-\infty}^{\infty} \mathrm{d}x' \left\{ G_-(x, x', y, 0) - G_+(x, x', y, 0) \right\} \frac{\partial \eta}{\partial x'}(t, x'), \tag{2.31}$$

in the upper layer and

$$u_2^t(t,x,y) = \frac{2}{V_- - V_+}\int_{-\infty}^{\infty} \mathrm{d}x' \left\{ V_- \frac{\partial G_-}{\partial y'}(x,x',y,0) - V_+ \frac{\partial G_+}{\partial y'}(x,x',y,0) \right\} \eta(t,x'), \tag{2.32}$$

$$v_2^t(t,x,y) = \frac{2}{V_- - V_+}\int_{-\infty}^{\infty} \mathrm{d}x' \left\{ V_- G_-(x,x',y,0) - V_+ G_+(x,x',y,0) \right\} \frac{\partial \eta}{\partial x'}(t,x'), \tag{2.33}$$

in the lower layer.

2.3.2 Linear topographic wave

In the absence of a point vortex, we examined the waves governed by linearized equations (2.29). Substituting the form of the wave solution, $\eta = \hat{\eta}_0 \exp\{\mathrm{i}(kx - \omega t)\}$, where $\hat{\eta}_0$ is a constant amplitude, k is the wavenumber in the x-direction and ω is the frequency, into the governing equation, we obtain the condition for the existence of a nontrivial solution, $\hat{\eta}_0 \neq 0$, as

$$\omega = \frac{k}{V_- - V_+}\left(\frac{V_-}{\sqrt{k^2+\lambda_-}} - \frac{V_+}{\sqrt{k^2+\lambda_+}} \right), \tag{2.34}$$

where we used both (2.16) and the relation

$$\int_{-\infty}^{\infty} \mathrm{d}x\, \mathrm{e}^{-\mathrm{i}kx} K_0\left(\sqrt{\lambda_\pm (x^2+y^2)} \right) = \frac{\pi \mathrm{e}^{-|y|\sqrt{k^2+\lambda_\pm}}}{\sqrt{k^2+\lambda_\pm}}. \tag{2.35}$$

This relation (2.34) is the dispersion relation for linear topographic Rossby waves propagating along a step-like topography which has been derived by Rhines (1977). According to (2.34), the phase speed and group velocity are

$$c = \frac{1}{V_- - V_+}\left(\frac{V_-}{\sqrt{k^2+\lambda_-}} - \frac{V_+}{\sqrt{k^2+\lambda_+}} \right), \tag{2.36}$$

$$c_g = \frac{1}{V_- - V_+}\left(\frac{\lambda_- V_-}{(k^2+\lambda_-)^{3/2}} - \frac{\lambda_+ V_+}{(k^2+\lambda_+)^{3/2}} \right), \tag{2.37}$$

respectively. Since $\lambda_- < \lambda_+$ and $V_+ < V_-$ hold for any value of k, c and c_g are always positive.

2.3.3 Linear pseudoimage solutions

In a previous study, Dunn et al. (2001) used a 1.5-layer model to show the motion of a point vortex propagating steadily along a step-like topography and referred to this phenomenon as the pseudoimage of the vortex. In this study, we sought to determine the linear solution, referred to as the linear pseudoimage solution, and to investigate the properties of the solution.

To determine the steadily propagating solution of (2.29) that progresses with the point vortex, we assumed that the solution was in the form $\eta = \eta(x - c_{pse}t)$, where the propagating speed, c_{pse}, is given as $c_{pse} \equiv \mathrm{d}X/\mathrm{d}t$. Since $\mathrm{d}X/\mathrm{d}t = u_1^t(t, X, Y) = O(\varepsilon)$, we can consider a situation in which the point vortex is fixed at $(0, Y_0)$. According to (2.29), the governing equation then becomes

$$\begin{aligned} -c_{pse}\frac{\partial \eta}{\partial x} =& \frac{\partial \Psi_2}{\partial x}(x,0) \\ &+ \frac{2}{V_- - V_+}\int_{-\infty}^{\infty} \mathrm{d}x' \left\{V_- G_-(x,x',0,0) - V_+ G_+(x,x',0,0)\right\} \frac{\partial \eta}{\partial x'}(t,x'), \end{aligned} \tag{2.38}$$

where $v_2^p = \partial \Psi_2/\partial x$. Although the term on the left side in the above equation has an order of $O(\varepsilon^2)$, to investigate the asymmetry of the solution due to the sign of c_{pse}, we leave this term explicitly in the equation. Using both Fourier transform methods and (2.16) and (2.35), we can obtain the solution to equation (2.38) as

$$\eta(x - c_{pse}) = \frac{1}{2\pi}\int_{-\infty}^{\infty} \mathrm{d}k \, \frac{\mathrm{e}^{\mathrm{i}k(x - c_{pse}t)}}{c - c_{pse}} \mathcal{F}[\Psi_2(x,0)], \tag{2.39}$$

where c is the phase speed of the topographic Rossby waves (2.36), and $\mathcal{F}[\Psi_2]$ is the Fourier transform of Ψ_2,

$$\mathcal{F}[\Psi_2(x,0)] = -\frac{1}{2}\frac{\varepsilon \mathrm{sgn}(\Gamma)}{V_- - V_+}\left\{\frac{\mathrm{e}^{-|Y_0|\sqrt{k^2+\lambda_-}}}{\sqrt{k^2+\lambda_-}} - \frac{\mathrm{e}^{-|Y_0|\sqrt{k^2+\lambda_+}}}{\sqrt{k^2+\lambda_+}}\right\}. \tag{2.40}$$

By substituting (2.39) into the linearized streamfunction caused by the topography,

ϕ_j, we can obtain the linear pseudoimage solution in the two-layer model:

$$\phi_1 = \frac{-1}{2\pi}\frac{V_-V_+}{V_- - V_+}\int_{-\infty}^{\infty} \mathrm{d}k\, \frac{\mathrm{e}^{\mathrm{i}k(x-c_{pse}t)}}{c-c_{pse}} \left(\frac{\mathrm{e}^{-|y|\sqrt{k^2+\lambda_-}}}{\sqrt{k^2+\lambda_-}} - \frac{\mathrm{e}^{-|y|\sqrt{k^2+\lambda_+}}}{\sqrt{k^2+\lambda_+}} \right) \mathcal{F}[\Psi_2(x,0)], \tag{2.41}$$

$$\phi_2 = \frac{-1}{2\pi}\frac{1}{V_- - V_+}\int_{-\infty}^{\infty} \mathrm{d}k\, \frac{\mathrm{e}^{\mathrm{i}k(x-c_{pse}t)}}{c-c_{pse}} \left(\frac{V_-\mathrm{e}^{-|y|\sqrt{k^2+\lambda_-}}}{\sqrt{k^2+\lambda_-}} - \frac{V_+\mathrm{e}^{-|y|\sqrt{k^2+\lambda_+}}}{\sqrt{k^2+\lambda_+}} \right) \mathcal{F}[\Psi_2(x,0)]. \tag{2.42}$$

The propagating velocity, c_{pse}, is given as

$$\begin{aligned} c_{pse} &= -\frac{\partial \phi_1}{\partial y}(0, Y_0) \\ &= \frac{\mathrm{sgn}(Y_0)}{2\pi}\frac{V_-V_+}{V_- - V_+}\int_{-\infty}^{\infty} \mathrm{d}k \frac{\mathrm{e}^{-|Y_0|\sqrt{k^2+\lambda_-}} - \mathrm{e}^{-|Y_0|\sqrt{k^2+\lambda_+}}}{c-c_{pse}} \mathcal{F}[\Psi_2(0,0)]. \end{aligned} \tag{2.43}$$

The sign of c_{pse} is equal to the sign of $Y_0\Gamma$. The fields of the streamfunction, ϕ_j and $\phi_j + \Psi_j$, are shown in figure 2.2. Although the ϕ_j field is similar to its counterpart in the 1.5-layer model, the $\phi_j + \Psi_j$ field differs from its counterpart. In the 1.5-layer model, the fluid on the opposite side of the point vortex is at rest because the pseudoimage solution completely cancels any effects from the point vortex on this side. In a two-layer model, this cancellation is achieved only in the vicinity of the topography in the lower layer.

2.3.4 Small but nonzero amplitude pseudoimage solution

If we suppose that $0 < \varepsilon \ll 1$ but ε is finite, we can examine the properties of a two-layer pseudoimage with a finite amplitude. In this parameter region, ϕ_j may have poles at the wavenumbers, k_c, that satisfy $c = c_{pse}$. The integrations (2.41) and (2.42) do not include k_c when the point vortex moves in the opposite direction of the topographic waves, i.e., $c_{pse} < 0$. In contrast, if $c_{pse} > 0$, the solutions include a singularity because the path must contain k_c. In the 1.5-layer model,

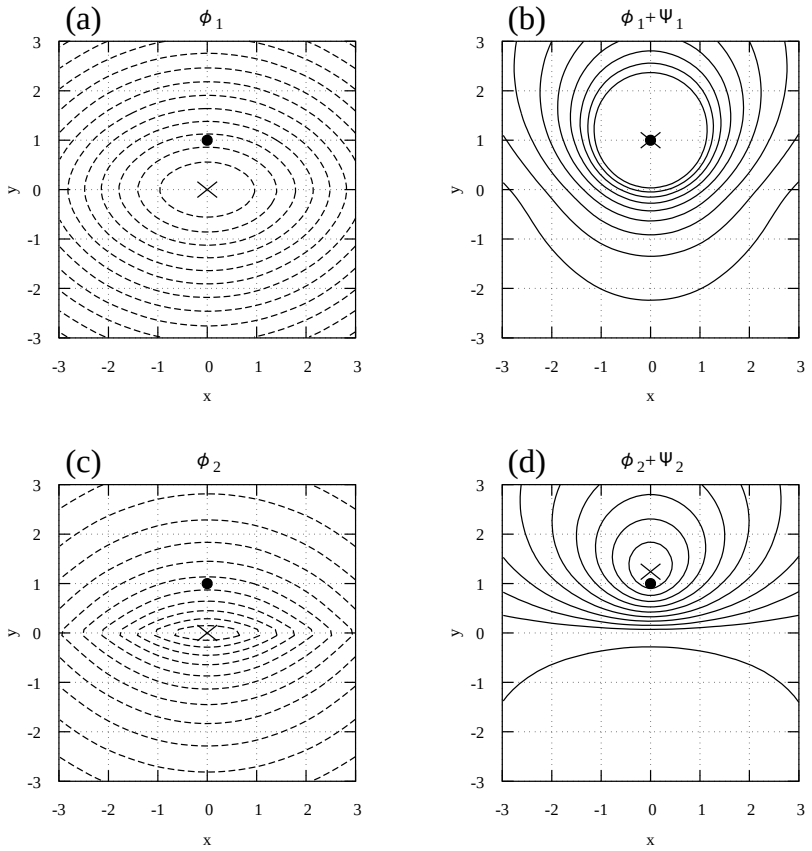

Fig. 2.2: The ϕ_j field (left column) and the $\phi_j + \Psi_j$ field (right column) of the linear pseudoimage solution in the upper layer (top row) and lower layer (bottom row). The positive and negative streamlines are indicated by the solid and dashed lines, respectively. The positions of the maximum or minimum value are denoted by the cross. In the left panels, the contour interval is 0.005, and the minimum values are -0.0235 in the upper layer and -0.0292 in the lower layer. In the right panels, the contour interval is 0.001, and the maximum values are 0.0694 in the upper layer and 0.0098 in the lower layer. In all the cases shown here, $\mathrm{sgn}(\Gamma) = -1$, $\varepsilon = 0.1$, $Y_0 = 1$, $\gamma_L = 10^{-3}$, and $\gamma_H = 1$. The point vortex is indicated by the closed circle at (0,1). The topography is located along $y = 0$.

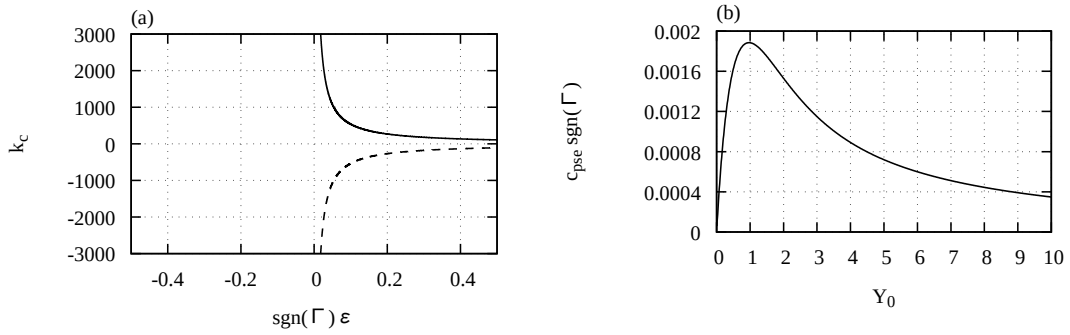

Fig. 2.3: (a) The dependencies of the wavenumbers, k_c, which satisfy $c = c_{pse}$ on $\mathrm{sgn}(\Gamma)\varepsilon$ for $Y_0 = 1$ and is calculated from (2.36) and (2.43). Since c is a function of k^2, there are both positive and negative k_c. As $\mathrm{sgn}(\Gamma)\varepsilon \to 0$, $|k_c|$ diverges to infinity. (b) The dependence of the propagation velocity, c_{pse}, on Y_0. The propagation velocity has a maximum at approximately $Y_0 = 0.7$. In both panels, $\gamma_H = 1$ and $\gamma_L = 10^{-3}$.

Dunn et al. (2001) confirmed that a finite length wave train in the wake of the vortex is excited and that the point vortex drifts towards the topography due to the presence of the singularity. Similar behaviours are expected in the two-layer model. However, since the poles k_c correspond to short waves, the singularity only has a small influence on the pseudoimage solution (see figure 2.3 (a)).

Figure 2.3 (b) shows the Y_0 dependence of c_{pse} in the parameter region $0 < \varepsilon \ll 1$. The propagation speed, $|c_{pse}|$, does not monotonically decrease along Y_0, and it has an extreme value at $Y_0 \approx 0.7$. This corresponds to the radial distance in the lower layer where the upper-point vortex has its maximum azimuthal velocity, i.e., the internal Rossby radius of deformation, $\lambda_+^{-1/2} \approx 0.7$. Another feature is that c_{pse} is non-singular as $Y_0 \to 0$. This nonsingularity occurs because the lower layer lacks a singular point at the location of the point vortex.

2.4 Finite-amplitude pseudoimage solution

It is difficult to obtain analytical expressions for finite-amplitude, nonlinear solutions. In this section, we determined finite-amplitude steadily propagating solutions by numerically solving equation (2.7) with (2.21)-(2.28). According to the linear arguments, the finite-amplitude pseudoimage solutions can exist only when $\mathrm{sgn}(\Gamma Y_0) = -1$. Hence, in this section, we focus on the case of an anticyclonic point vortex at the deeper side.

First, we use the Galilean transformation,

$$x \to \xi = x - c_{pse}t. \tag{2.44}$$

Then, the governing equation can be written as

$$-c_{pse}\frac{\partial \eta}{\partial \xi} + u_2\frac{\partial \eta}{\partial \xi} = v_2. \tag{2.45}$$

As a result, the pseudoimage solutions satisfy the equation

$$\frac{\partial \eta}{\partial \xi} = \frac{v_2}{u_2 - c_{pse}}. \tag{2.46}$$

The boundary condition can be written as

$$\eta \to 0 \quad \text{as} \quad |\xi| \to \infty. \tag{2.47}$$

Furthermore, we assume that the solution is symmetric with $\xi = 0$. Therefore, we have

$$\eta(-\xi) = \eta(\xi). \tag{2.48}$$

We compute η only for $\xi \leq 0$.

To perform the numerical calculations, we discretize the potential vorticity front into N nodes for $-\xi_\infty \leq \xi_n \leq 0$, where $\xi_1 = -\xi_\infty$ and $\xi_N = 0$. Since the contribution of the far field is weak in the integration (2.28) and (2.29), the node

spacing near the crest should be fine, whereas the spacing in the far field can be rough. Therefore, we set $\xi_n = \mu_0(n - N)$ for $n \geq N_1$ and $\xi_n = -W + 1 - \mu_0(N_1 - n) - \exp[\mu_0(N_1 - n)/5]$ for $n < N_1$, where $W = \mu_0(N - N_1)$ and $\xi_\infty = W - 1 + \mu_0(N_1 - 1) + \exp[\mu_0(N_1 - 1)/5]$. In this study, we set $\mu_0 = 0.02$, $N = 2650$ and $N_1 = 1150$; thus, we have $W = 30$ and $\xi_\infty \simeq 151$. The finite-difference form of (2.46) is

$$\frac{\eta_{n+1} - \eta_{n-1}}{\xi_{n+1} - \xi_{n-1}} = \frac{v_{2,n}}{u_{2,n} - c_{pse}}, \qquad n = 1, ..., 2N - 1. \tag{2.49}$$

The boundary conditions at $\xi = \xi_1, \xi_N$ are

$$\eta_1 = 0, \tag{2.50}$$

$$\eta_N = \frac{\eta_{N-1} - \eta_{N-2}}{\xi_{N-1} - \xi_{N-2}}(\xi_N - \xi_{N-1}) + \eta_{N-1}, \tag{2.51}$$

where (2.50) corresponds to (2.47), and (2.51) indicates that the front can be approximated as a quadratic function near the origin. As a result, we can obtain the frontal displacement, η_n, and the propagation velocity, c_{pse}, for the given values of ε by solving the equations (2.49), (2.50), (2.51), with the condition that the solution propagates with the point vortex, $c_{pse} = u_1(0, Y_0)$, where the point vortex is located at $(0, Y_0)$. We used MINPACK (Moreé et al. 1980) to solve the nonlinear simultaneous equations, with the front displacement of the linear solution (2.39) as the initial value in the iterative calculation. In this study, the midpoint method was used for the numerical integration. The validity of the obtained solutions was confirmed by conducting numerical experiments with the solutions as initial conditions. In the following subsections, we set the remaining parameter values as $\gamma_H = 1$, $\gamma_L = 10^{-3}$, and $Y_0 = 1$.

2.4.1 Dependency on ε

Figure 2.4 shows the frontal displacement and propagation speeds for various values of ε obtained by solving the simultaneous equations. As ε increases, both the

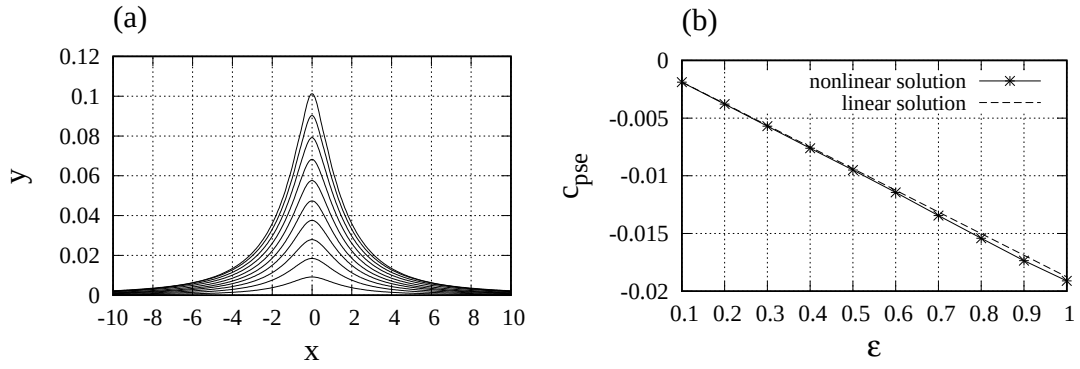

Fig. 2.4: (a) The potential vorticity front and (b) its propagation speed for each value of ε. ε ranges from 0.1 to 1 in steps of 0.1. The front with the maximum displacement was observed for $\varepsilon = 1$. The propagation speed obtained by the linear solution is indicated by the dashed line in the right panel.

displacement and the propagation speed, $|c_{pse}|$, increase. Figure 2.4 (b) suggests that the linear solution is valid for small values of ε. Figure 2.5 shows that the nonlinearity sharpens the peak of the frontal displacement.

2.4.2 The saddle-node point

Figure2.6 shows the current vectors caused by the frontal displacement and the point vortex in ξ-y coordinates. There are two saddle-node points in the front with $u_2 - c_{pse} = 0$. Since these points also exist when ε is small, the existence of these points is believed to be a common feature of the pseudoimage solutions. The existence of this point may affect the time evolution of the front as in eddy-jet interactions (Bell and Pratt 1992; Capet and Carton 2004); this will be investigated with numerical experiments in Section 2.5.1.

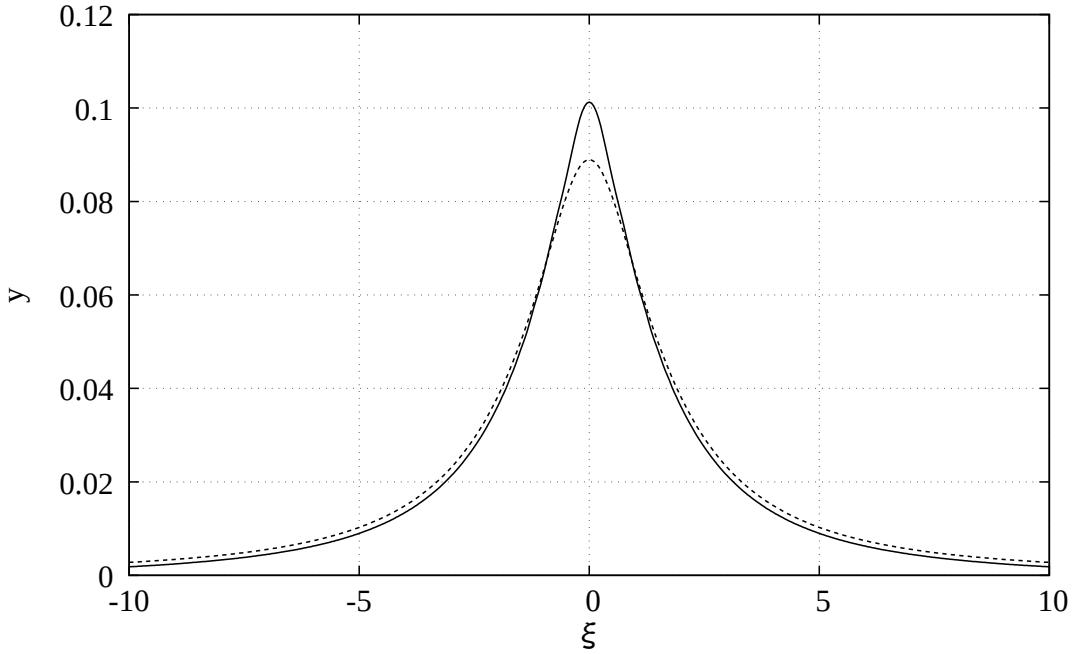

Fig. 2.5: The potential vorticity front of the linear (dashed line) and nonlinear (solid line) solutions for $\varepsilon = 1$.

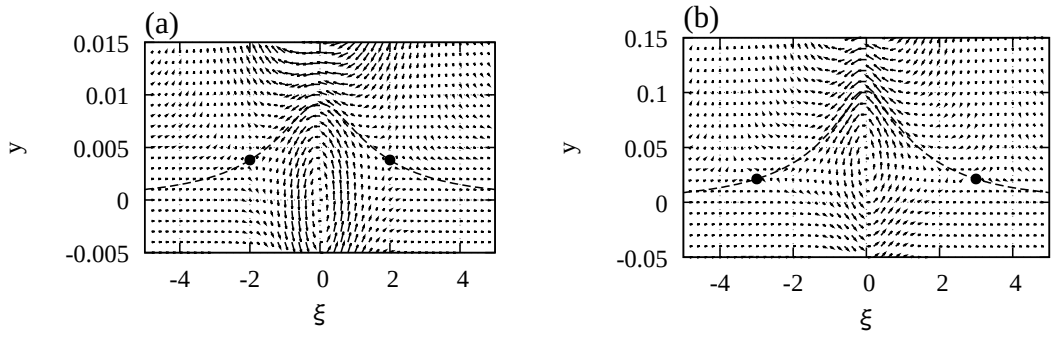

Fig. 2.6: The potential vorticity front of the nonlinear solution and the current vectors caused by the nonlinear solution and the point vortex in ξ-y coordinates. Panel (a) shows the case $\varepsilon = 0.1$, and panel (b) shows the case $\varepsilon = 1$. The closed circles on the front represent the saddle points.

2.5 Numerical experiments for nonlinear evolution

In this section, we perform numerical experiments. First, we consider the temporal evolution of the pseudoimage solution obtained in the previous section. Then, to investigate the temporal evolution of the system in the parameter space consisting of ε and Y_0, we perform numerical experiments with various initial conditions.

As in the previous section, we resolve the front into discrete nodes with positions (x_n, η_n). From the Lagrangian perspective, the temporal evolution of these nodes can be written as

$$\frac{\mathrm{d}x_n}{\mathrm{d}t} = u_2(t, x_n, \eta_n), \tag{2.52}$$

$$\frac{\mathrm{d}\eta_n}{\mathrm{d}t} = v_2(t, x_n, \eta_n). \tag{2.53}$$

We can determine the temporal evolution of the system by calculating (2.8), (2.52), and (2.53). The velocities advecting the point vortex and the front can be evaluated numerically by calculating (2.21)-(2.28). The numerical integration scheme used to calculate the velocities is the same as in the previous section. The initial node distribution is the same as that in Section 4. Since the front near the point vortex elongates with time in its evolution, a new node is added by linear interpolation to keep a spatial resolution when the distance between the adjacent nodes, μ, is $\mu > 1.5\mu_0$, where $\mu_0 = 0.02$. This interpolation is performed in the region of $|x| \leq W$ because the elongation of the front is negligibly small in the region of $|x| > W$, where $W = 30$. When filamentation structures appear, the number of nodes in the front rapidly increases. To avoid calculating a large number of nodes, we use a contour surgery algorithm (Dritschel 1988; Shimada and Kubokawa 1997). In particular, we employ the algorithm described in Shimada and Kubokawa (1997). The validity of the predefined parameter μ_c, the minimum distance between two

segments on the front, was verified by comparing the area surrounded by the front and the topography in surgery and no-surgery experiments for several different parameters. The fourth-order Runge-Kutta method was used for time integration in the numerical experiments. The accuracy of the calculation was verified by comparing the phase speed of a small amplitude sine wave in the absence of a point vortex calculated by the numerical experiment with the analytical result (2.36). All the numerical experiments in this section used $\gamma_L = 10^{-3}$, $\gamma_H = 1$, $\mu_c = 0.002$, and a time step of $\Delta t = 0.01$. The parameters ε and Y_0 are shown for each experiment.

2.5.1 Temporal evolution of the pseudoimage

Figure 2.7 shows the evolution of the nonlinear pseudoimage solution for $\varepsilon = 1$. Figure 2.7 (a) demonstrates that a frontal wave was generated, and that the wavenumber increased as the wave approached the saddle-node point in the direction of movement. Figure 2.7 (b) shows that the frontal wave is stationary and grows near the saddle-node points in the coordinate system that moves with the pseudoimage. These features suggest that the symmetry of the pseudoimage solutions is unstable and likely to collapse (see figure 2.8 (a)). On the other hand, the propagation speed of the point vortex remains nearly constant for some time, as shown in figure 2.8 (b), suggesting that the interaction between the vortex and the potential vorticity anomaly is insensitive to the shape of the front. The frontal wave dynamics are the same as those of the topographic waves. The phase speed along the front, c_f, can be written as

$$c_f = u_2 + c, \tag{2.54}$$

where u_2 is the velocity along the front and c is given by (2.36). Since the waves are stationary in the moving coordinate system, i.e., $c_f - c_{pse} = 0$, we can calculate

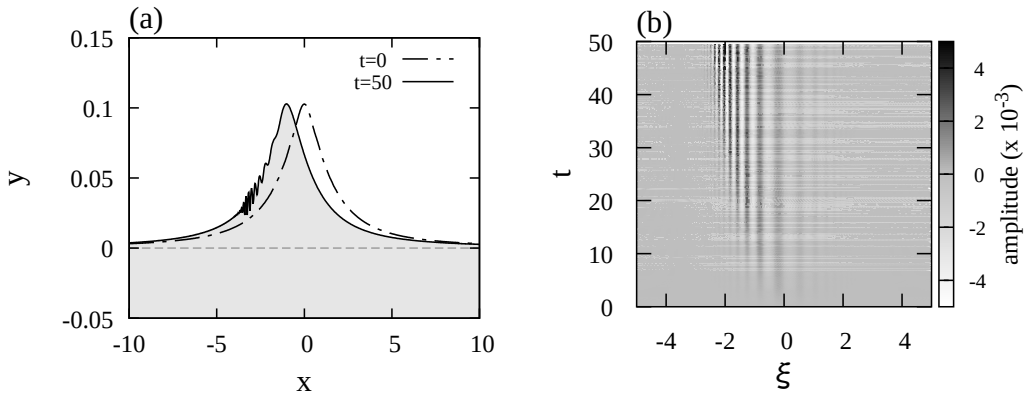

Fig. 2.7: (a) Temporal evolution of the front of the nonlinear solution for $\varepsilon = 1$. The solid line corresponds to the front at $t = 50$, while the dash-dotted line corresponds to the front at $t = 0$. The fluid in the shaded area has a higher potential vorticity. (b) Temporal evolution of the amplitude of the frontal wave in the coordinate system moving at c_{pse}. The remaining parameter is $Y_0 = 1$.

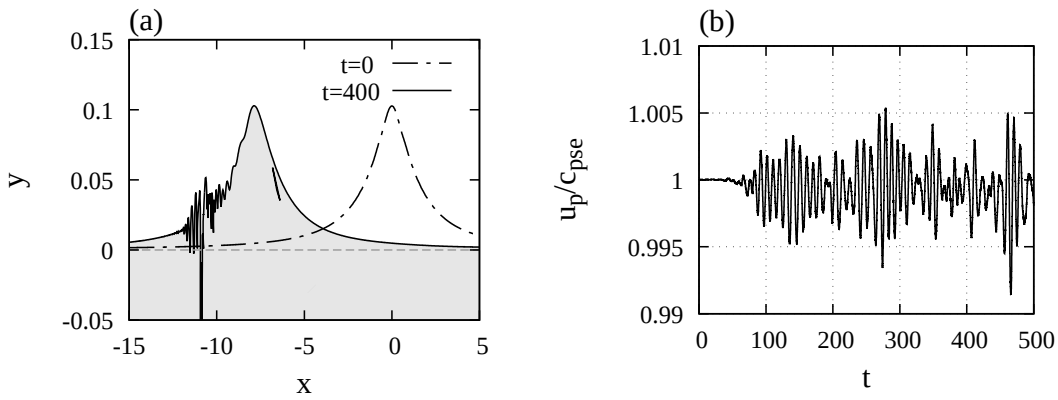

Fig. 2.8: (a) Temporal evolution of the front of the nonlinear solution for $\varepsilon = 1$. The solid line corresponds to the front at $t = 400$, while the dash-dotted line corresponds to the front at $t = 0$. The fluid in the shaded area has a higher potential vorticity. (b) Temporal evolution of the ratio of the propagation velocity of the point vortex, u_p, to the propagation velocity obtained from the nonlinear solution, c_{pse}. The parameters used in the numerical experiment are the same as those in figure 2.7.

the wavenumber as

$$0 = u_2 + c - c_{pse}, \tag{2.55}$$

which shows that k is infinitely large at the stagnation point. Figure 2.9 (a) shows the frontal displacement of the frontal wave at $t = 50$, which we can use to estimate the local wavenumber as a function of the moving coordinate, $\zeta = x - c_{pse}t$. Figure 2.9 (b) shows that the wavenumbers calculated by (2.54) agree well with those estimated from the experiment. The theoretical group velocity based on the wavenumber in the moving coordinate system, $c_{gf} = u_2 - c_{pse} + c_g$, where c_g is given by (2.37), is shown in figure 2.9 (c). The group velocity in the ξ-direction is negative and vanishes at the stagnation point. Therefore, according to the experimental result shown in figure 2.7, the wave energy converges at the stagnation point.

2.5.2 Generation of a heton-like vortex pair and the classification of the motion based on ε

We show the results of experiments in which the parameter ε was varied, and we reveal the typical temporal evolution patterns of this system. In all the experiments in this subsection, the initial position of the point vortex was fixed at $(0, 1)$, and there was initially no frontal displacement.

An anticyclonic point vortex

We first consider the case of an anticyclonic point vortex, i.e., $\mathrm{sgn}(\Gamma) = -1$. Figure 2.10 shows the temporal evolution of the potential vorticity front interacting with the point vortex with $\varepsilon = 0.1$. The temporal evolution of the velocity of the point vortex, (u_p, v_p), is shown in figure 2.11. The point vortex moves steadily along the topography, combining with the vortex caused by the small frontal displacement.

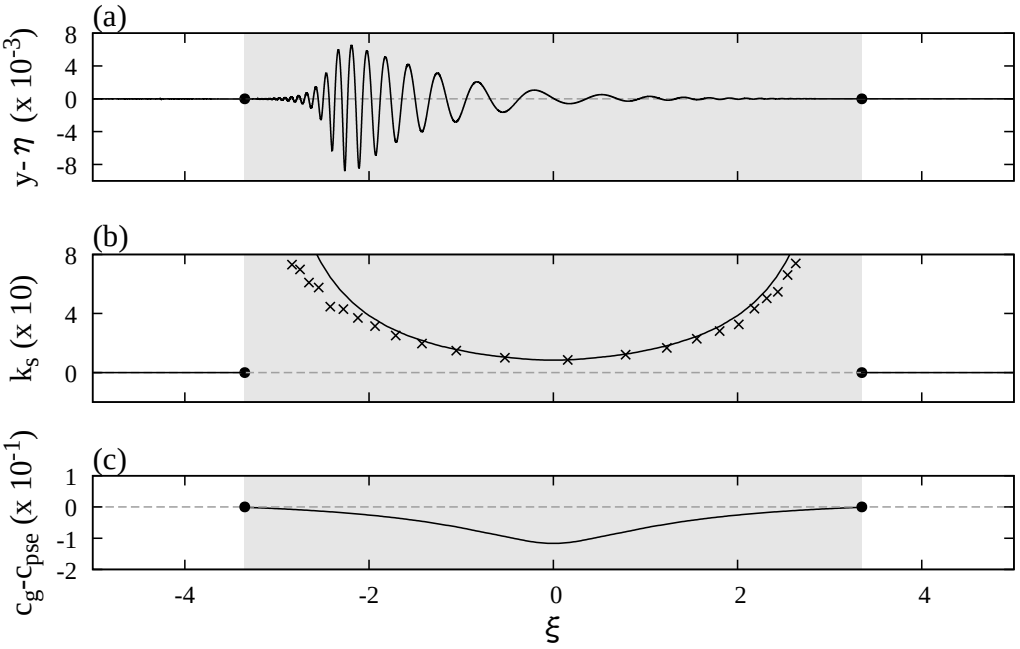

Fig. 2.9: (a) The frontal disturbance caused by the difference between the η obtained from the numerical experiment at $t = 50$ and that obtained from the nonlinear pseudoimage solution. (b) The distribution of the stationary wavenumber. The solid line indicates the stationary local wavenumber obtained from the phase velocity of the linear frontal wave, while the crosses indicate the local wavenumber estimated from (a). (c) The group velocity of the stationary wavenumber as a function of ε. In all panels, the closed circles on the zero vertical coordinate denote the ξ coordinate of the saddle-node points, and the shaded area corresponds to the region where $u_2 - c_{pse} < 0$. The parameters used in the numerical experiment are the same as those in figure 2.7.

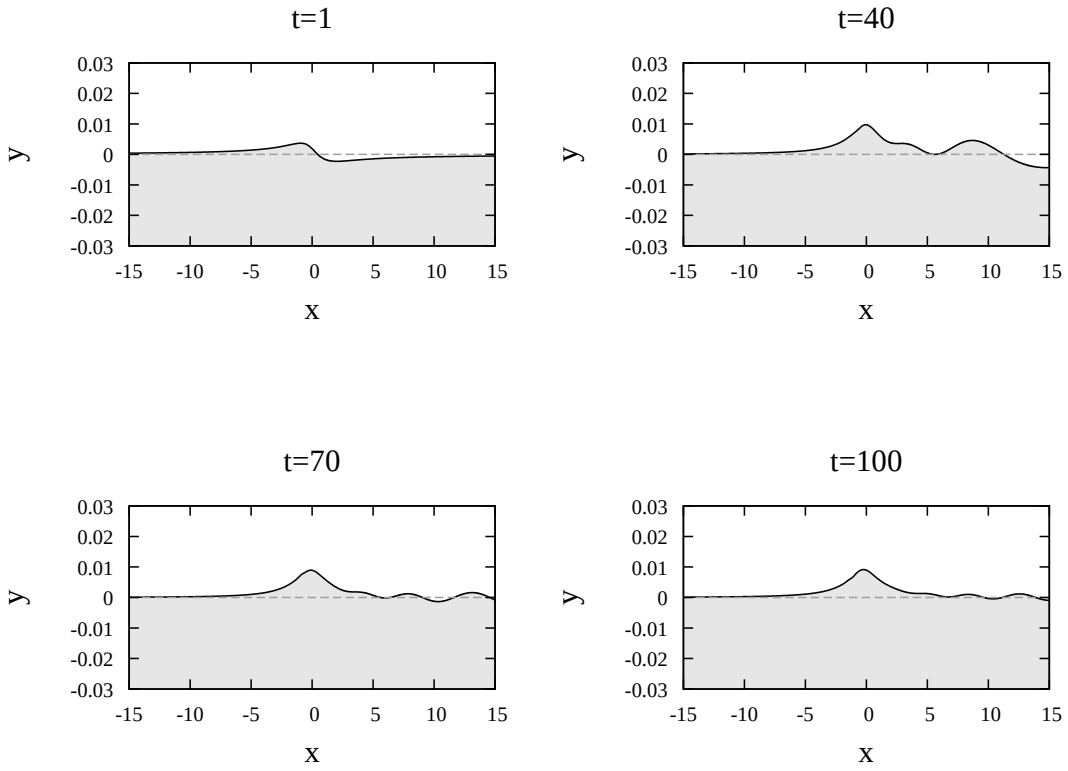

Fig. 2.10: The temporal evolution of the potential vorticity front interacting with the anticyclonic point vortex. The parameter values are $\varepsilon = 0.1$ and $Y_0 = 1$.

We refer to the behaviour in which the point vortex moves along the topography as pseudoimage-type behaviour. Figures 2.12 and 2.14 show the temporal evolution of the front in the case that $\varepsilon = 1, 2$. When $\varepsilon = 1$, the disturbances collapse, similar to those shown in figure 2.8 (b). In the case of $\varepsilon = 2$, the intrusion of the front to the opposite side of the point vortex forms, causing the peak structure to become a topographic vortex, which is caused by the potential vorticity conservation. However, they are classified as pseudoimages if they move along the topography.

Figure 2.16 shows the evolution of the front and the point vortex for $\varepsilon = 10$. The temporal evolution of (u_p, v_p) is shown in figure 2.17. The point vortex attracts the high potential vorticity fluid from the shallow side, forming a dipole structure. Due to the formation of this dipole structure, the point vortex has a velocity

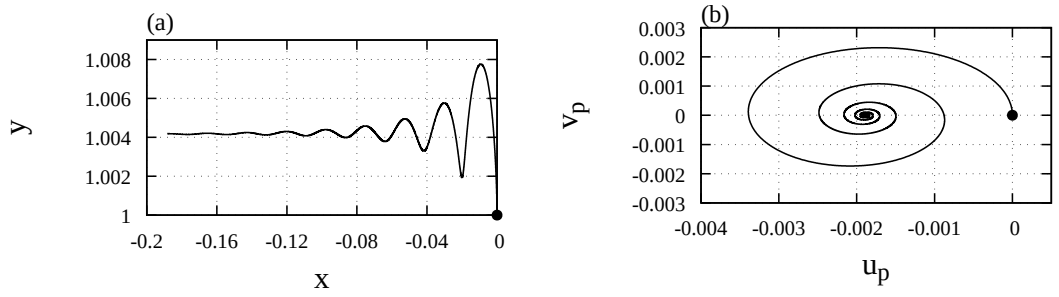

Fig. 2.11: The trajectory of the point vortex in (a) x-y space and (b) u_p-v_p space for the case shown in figure 2.10, obtained by computing from $t = 0$ to $t = 100$. The starting points at $t = 0$, which are located at $(0, 1)$ on the left and $(0, 0)$ on the right, are indicated by the closed circles.

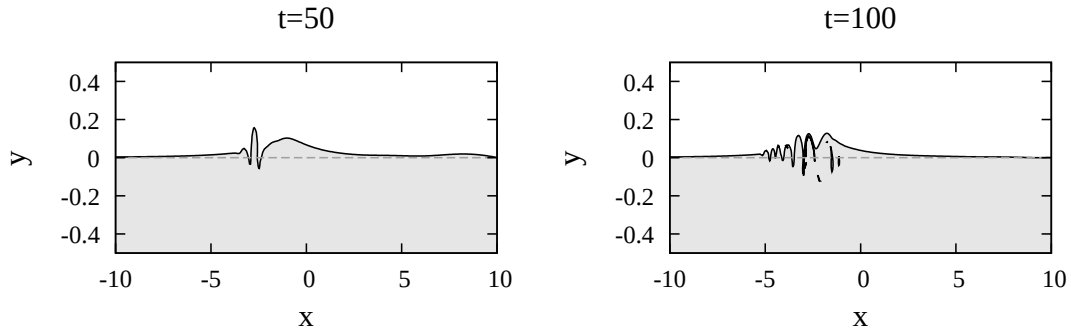

Fig. 2.12: The temporal evolution of the potential vorticity front interacting with the anticyclonic point vortex. The parameter values are $\varepsilon = 1.0$ and $Y_0 = 1$.

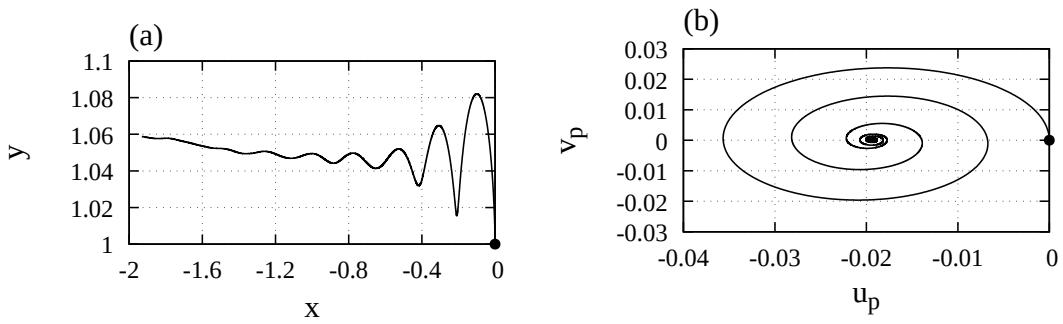

Fig. 2.13: The trajectory of the point vortex in (a) x-y space and (b) u_p-v_p space for the case shown in figure 2.12, obtained by computing from $t = 0$ to $t = 100$. The starting points at $t = 0$, which are located at $(0, 1)$ on the left and $(0, 0)$ on the right, are indicated by the closed circles.

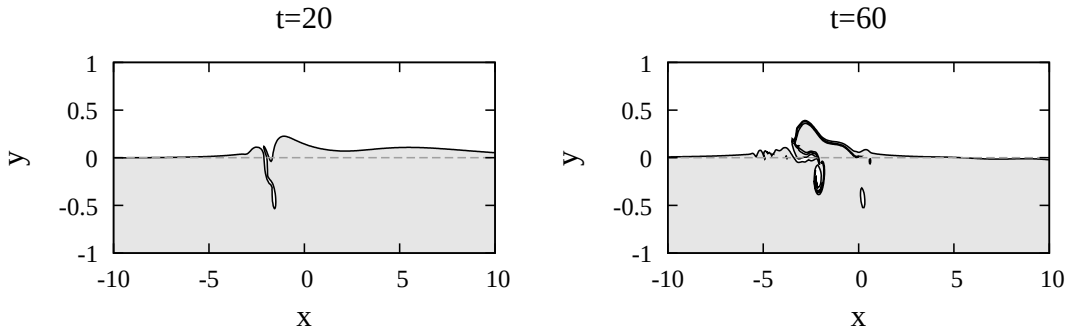

Fig. 2.14: The temporal evolution of the potential vorticity front interacting with the anticyclonic point vortex. The parameter values are $\varepsilon = 2$ and $Y_0 = 1$.

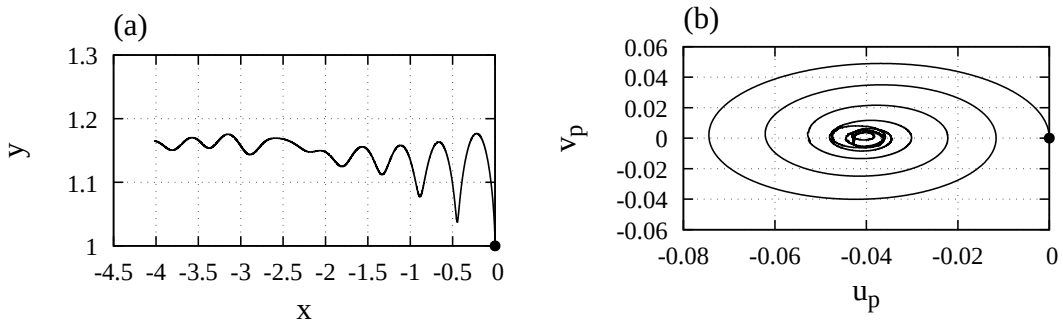

Fig. 2.15: The trajectory of the point vortex in (a) x-y space and (b) u_p-v_p space for the case shown in figure 2.14, obtained by computing from $t = 0$ to $t = 100$. The starting points at $t = 0$, which are located at $(0, 1)$ on the left and $(0, 0)$ on the right, are indicated by the closed circles.

component perpendicular to the topography, v_p (see figure 2.17). Since the dipole structure includes both the upper-layer point vortex and the lower-layer vortex created by the potential vorticity patch, we hereafter refer to this behaviour as heton-type behaviour (Hogg and Stommel 1985).

McDonald (1998) used a 1.5-layer model to describe the existence of motion types other than those described above when the point vortex is intense, i.e., $\varepsilon \gg 1$. Figures 2.18 and 2.19 show the temporal evolution for $\varepsilon = 100$. During the early stages of the temporal evolution, the point vortex draws a large amount of fluid from the shallower side and wraps the fluid around itself. However, as more time passes, the filament wrapped around the point vortex has a weaker effect on the point vortex, and the system resembles a system with a moderate ε, forming a hetonic structure consisting of the filament-wrapped point vortex and the high potential vorticity patch from the shallower side.

A cyclonic point vortex

We next consider a cyclonic point vortex, i.e., $\mathrm{sgn}(\Gamma) = 1$. Figures 2.20 and 2.21 show the temporal evolution of the front and the point vortex, as well as the evolution of the velocity, (u_p, v_p), for $\varepsilon = 1$. The point vortex moves in the same direction as the topographic waves, and the small-scale wave train behind the peak of the front is confirmed. As discussed in Section 2.3.4, this wave train occurs only for cyclonic point vortices, and it is excited by the singularity in (2.41) and (2.42) in linear theory, which was shown mathematically in Dunn et al. (2001). Although wave radiation was expected to weaken the isolated structure, it propagated similarly to the anticyclonic vortex, at least in our computation time. Therefore, we refer to this behaviour as pseudoimage-type behaviour. The point vortex did not drift towards the topography, as discussed by Dunn et al. (2001). However, the behaviour for longer computation times remains unknown.

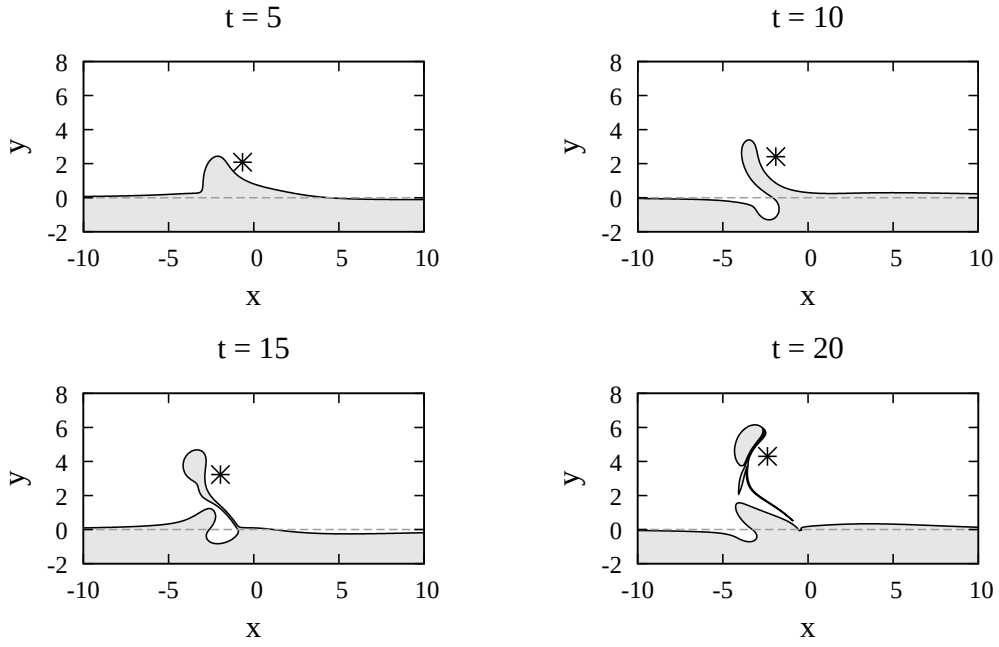

Fig. 2.16: The temporal evolution of the potential vorticity front and the anticyclonic point vortex. The parameter values are $\varepsilon = 10$ and $Y_0 = 1$.

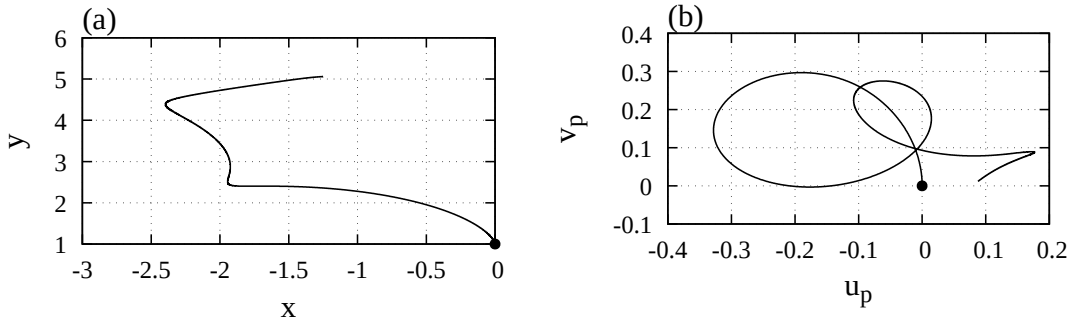

Fig. 2.17: The trajectory of the point vortex in (a) x-y space and (b) u_p-v_p space for the case shown in figure 2.16, obtained by computing from $t = 0$ to $t = 30$. The starting points at $t = 0$ are indicated by the closed circles.

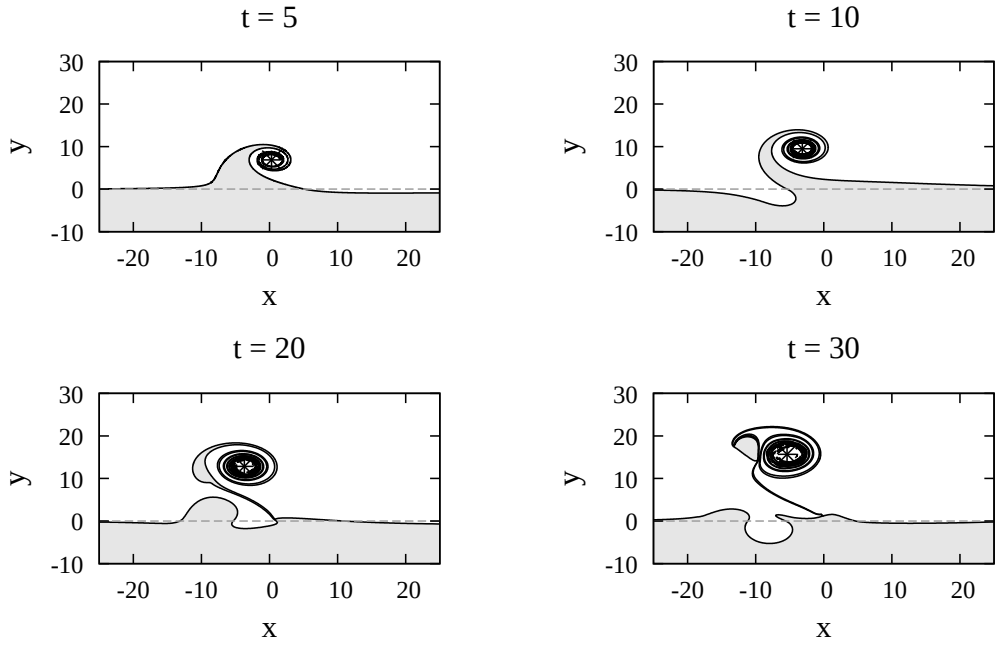

Fig. 2.18: The temporal evolution of the potential vorticity front and the anticyclonic point vortex. The parameter values are $\varepsilon = 100$ and $Y_0 = 1$.

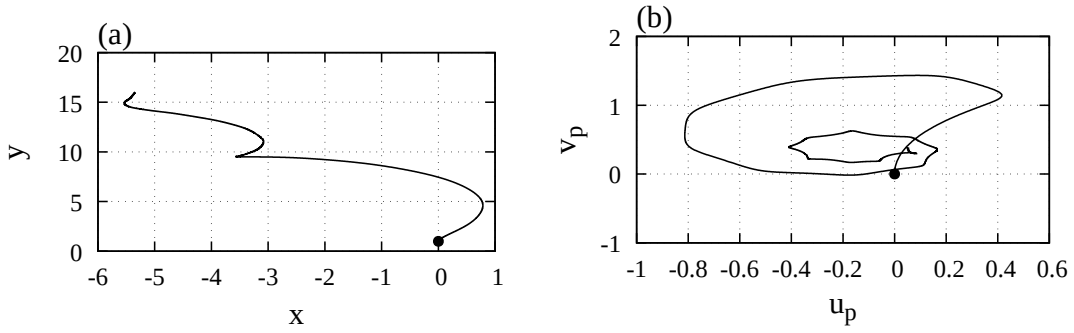

Fig. 2.19: The trajectory of the point vortex in (a) x-y space and (b) u_p-v_p space for the case shown in figure 2.18, obtained by computing from $t = 0$ to $t = 30$. The starting points at $t = 0$ are indicated by the closed circles.

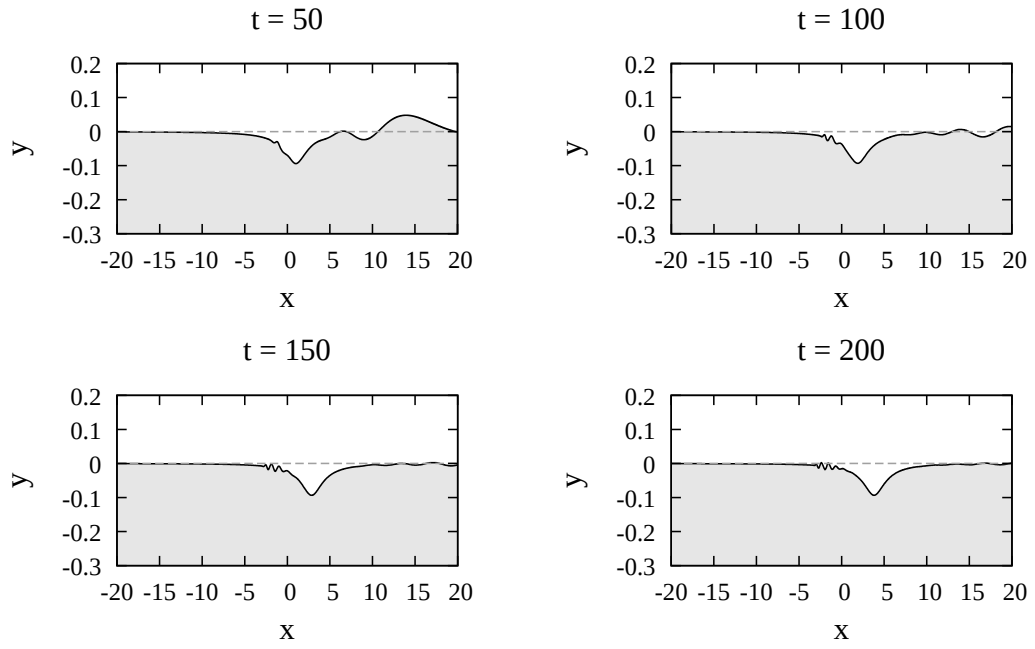

Fig. 2.20: The temporal evolution of the potential vorticity front for a cyclonic point vortex. The parameter values are $\varepsilon = 1$ and $Y_0 = 1$.

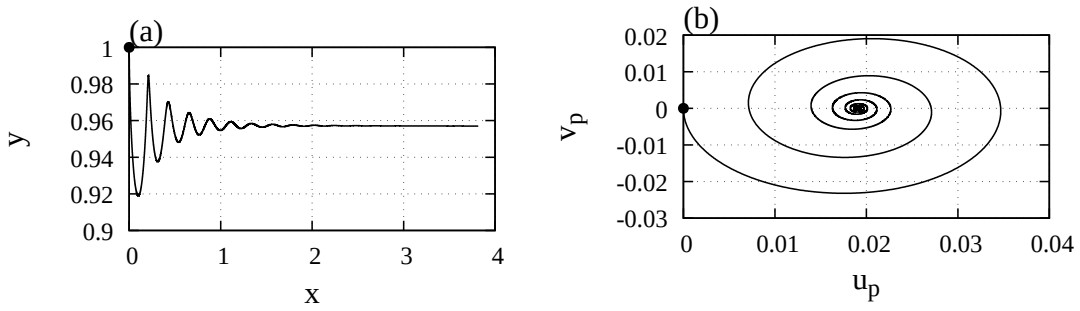

Fig. 2.21: The trajectory of the cyclonic point vortex in (a) x-y space and (b) u_p-v_p space for the case shown in figure 2.20, obtained by computing from $t = 0$ to $t = 200$. The starting points at $t = 0$ are indicated by the closed circles.

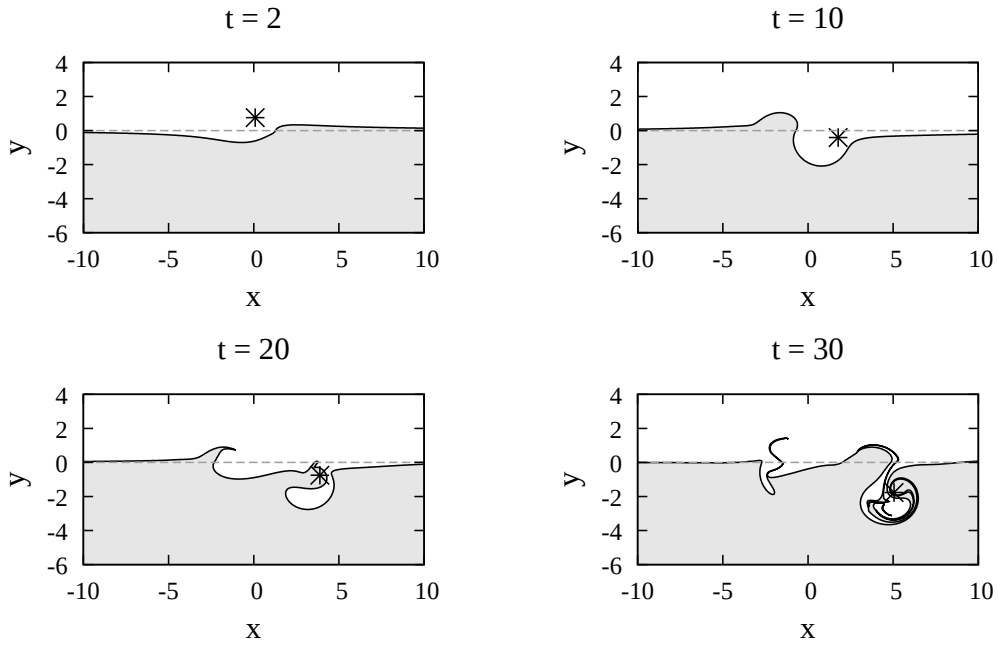

Fig. 2.22: The temporal evolution of the potential vorticity front and the cyclonic point vortex. The parameter values are $\varepsilon = 10$ and $Y_0 = 1$.

Figures 2.22 and 2.23 show the results for $\varepsilon = 10$. With this parameter value, the point vortex moves towards the topography in the deeper region, attracting low potential vorticity fluid. As a result, the point vortex approaches and then passes the topography, forming a dipole structure with the low potential vorticity fluid. After the dipole structure is formed, the vortices move away from the topography. We classify this behaviour as heton-type behaviour. The behaviour for $\varepsilon = 100$ is shown in figures 2.24 and 2.25. Similar to the anticyclonic case, the cyclonic point vortex initially wraps the filament around itself; however, as more time passes, the filament stops wrapping, and the vortex couples with the low potential vorticity patch in the deeper region, resulting in a heton-type motion.

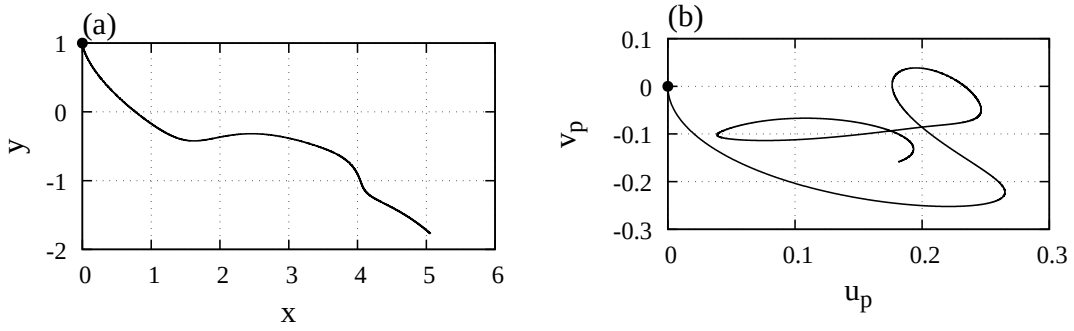

Fig. 2.23: The trajectory of the cyclonic point vortex in (a) x-y space and (b) u_p-v_p space for the case shown in figure 2.22, obtained by computing from $t = 0$ to $t = 30$. The starting points at $t = 0$ are indicated by the closed circles.

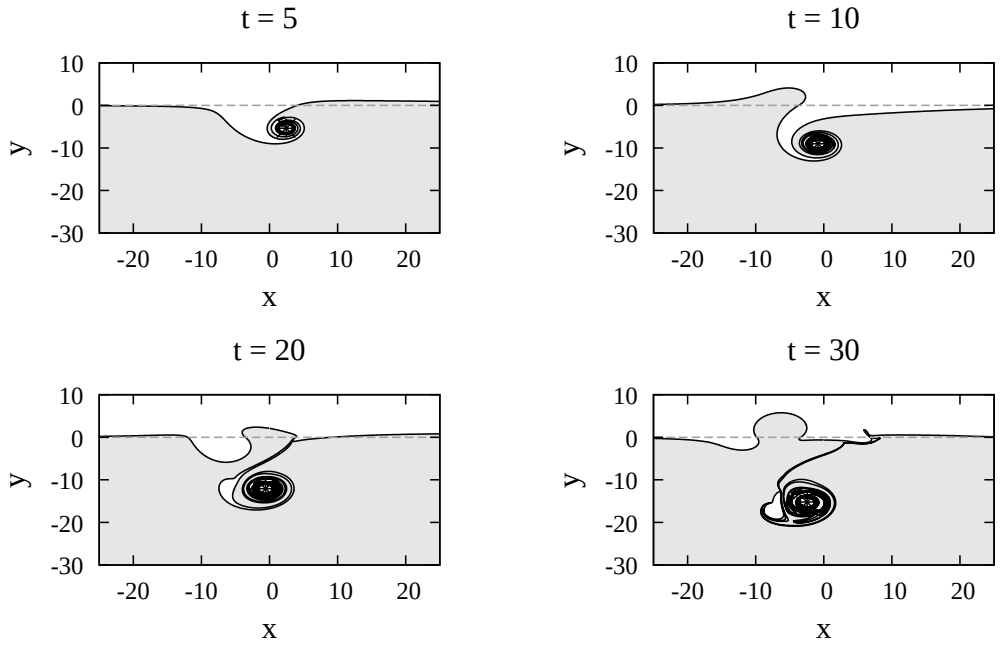

Fig. 2.24: The temporal evolution of the potential vorticity front and the cyclonic point vortex. The parameter values are $\varepsilon = 100$ and $Y_0 = 1$.

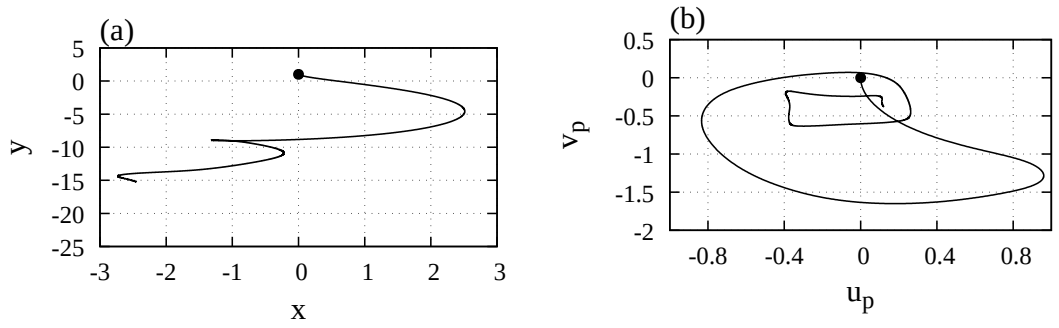

Fig. 2.25: The trajectory of the cyclonic point vortex in (a) x-y space and (b) u_p-v_p space for the case shown in figure 2.24, obtained by computing from $t = 0$ to $t = 30$. The starting points at $t = 0$ are indicated by the closed circles.

2.5.3 Classification of the motion based on ε and Y_0

In the previous subsection, we used numerical experiments with the strength of the point vortex, ε, as a parameter to demonstrate that there are two types of motions that commonly occur in our model. Previous studies have observed the formation of dipole structures in various systems and have identified the regions where the dipole structures form in parameter space (e.g. Shimada and Kubokawa 1997; Vandermeirsch et al. 2003; Capet and Carton 2004). In this subsection, we conduct numerical experiments with ε and the initial location of the point vortex, Y_0, as parameters and classify the motion types in ε-Y_0 space. Based on the trajectory in u_p-v_p space, we classified pseudoimage-type motions as those where the temporal evolution of v_p asymptotically approached zero or oscillated near zero after a sufficiently long calculation, while other motions were classified as hetonic. The numerical experiments were conducted until $t = 100$. In the case that

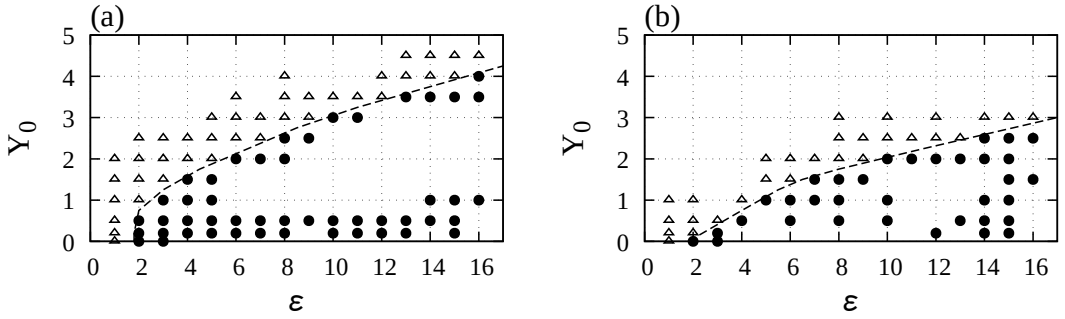

Fig. 2.26: The diagram of the motion classification in ε-Y_0 space. The circulation of the point vortex is (a) $\mathrm{sgn}(\Gamma) = -1$ and (b) $\mathrm{sgn}(\Gamma) = 1$. The triangles and circles in the diagram indicate pseudoimage-type and heton-type motions, respectively.

$f = 10^{-4}\,\mathrm{s}^{-1}$, $H_2 = 2000\,\mathrm{m}$ and $\Delta H = 1000\,\mathrm{m}$, $T = f^{-1}(\Delta H/H_2)^{-1} = 2 \times 10^4\,\mathrm{s}$, so that $t = 100$ corresponds to approximately 200 days.

Figure 2.26 (a) depicts the phase diagram for the anticyclonic case, showing the distribution of the typical motion types in ε-Y_0 space. The ε-Y_0 relation at the boundary between the two motion types can be divided into two regions. For $Y_0 < 1$, the value of Y_0 changes rapidly and approaches zero at small but finite ε. This feature occurs because the point vortex and the topography are in different layers. When $Y_0 = 0$, a point vortex with negative Γ moves towards the deeper side ($Y > 0$), and if ε is small, the pseudoimage propagates along the topography with $Y \neq 0$. For $Y_0 > 1$, the slope of the boundary between the two motion types in ε-Y_0 space becomes gentler, and the slope becomes linear for sufficiently large Y_0. This feature occurs because when the value of Y_0 is initially large, the point vortex and the front interact primarily through the barotropic

mode. Since the nondimensional internal Rossby deformation radius, $\lambda_+^{-1/2}$, is approximately 0.7 in this model, the barotropic mode dominates the interaction when $Y_0 > \lambda_+^{-1/2}$. Because the frontal self-advection component has a baroclinic component even when Y_0 is large, the results of our model do not exactly match those of a barotropic model.

Figure 2.26 (b) shows the phase diagram for the cyclonic case. When $Y_0 = 0$, the motion is symmetric about the x-axis, similar to the case of the anticyclonic point vortex, since $\psi_j(x, y) = -\psi_j(x, -y)$. Therefore, in the pseudoimage motion starting from $Y_0 = 0$ with $\varepsilon = 1$ shown in figure 2.26 (b), the cyclonic point vortex moves to the shallower side of $y < 0$ and propagates in the opposite direction to the topographic wave, in contrast to the behaviour shown in figures 2.20 and 2.21. Although the border that divides the behaviour is unclear, all of the pseudoimages with $Y_0 > 0.25$ in our experiments have a similar structure to that shown in figure 2.20. The boundary between pseudoimage-type and heton-type motions is almost the same as that in the anticyclonic case. However, in the cyclonic case, the slope of this boundary is smaller than that in the anticyclonic case for $Y_0 < 1$. This difference occurs due to the difference in the direction of the displacement of the front. In the cyclonic case, as ε increases, the front tends to move away from the point vortex in the y direction , whereas in the anticyclonic case, the front approaches the point vortex as ε increases. This result indicates that for the same value of Y_0, the anticyclonic vortex is more likely to interact with the topography than the cyclonic vortex.

2.6 Summary

In this study, the interaction between a point vortex in the upper layer and the step-like topography in the lower layer was investigated using a two-layer quasi-

geostrophic model in the f-plane. The results can be summarised as follows.

- We derived the linear pseudoimage solution that steadily propagates along the topography in the two-layer system and discussed the properties of the solution. The results suggested that the steadiness of the finite-amplitude solution is lost when the solution propagates in the same direction as the topographic waves, and that the point vortex can move along the topography even when the point vortex and topography are close because they are in different layers.

- The finite-amplitude, steadily propagating nonlinear pseudoimage solution was calculated numerically. We found that the flow field of the system, which includes the solution, always has saddle-node points on the potential vorticity front in a coordinate system that moves with the solution. In the numerical experiments where the nonlinear solution was used as the initial condition, short frontal waves appeared near the saddle-node point, and the symmetric structure of the front collapsed. Even after the collapse, the point vortex moved in the same manner as in the steadily propagating solutions.

- We showed that the point vortex has two types of motion in this system: motion along the topography due to the pseudoimage when the strength of the point vortex, ε, is small, and motion away from the topography due to the formation of a heton-like structure when ε is large. In addition to ε, we treated the initial distance between the point vortex and the topography, Y_0, as a parameter and classified the motion types in ε-Y_0 space. We found that pseudoimage-type motion exists in the region where Y_0 is large or ε is small, while heton-type motion exists in the region where Y_0 is small or ε is large. The boundary in parameter space that separates these motions behaves differently in relation to Y_0 and the internal deformation radius. When

the diagrams of the anticyclonic and cyclonic point vortices are compared, it can be seen that the anticyclonic vortex is more likely to move away from the topography than the cyclonic vortex for the same value of Y_0.

Chapter 3

Gaussian Vortex and Sloping Bottom Topography Interactions

3.1 Introduction

The model with a point vortex and a step-like topography, which is treated in the previous chapter, can capture the fundamental features of the interactions between an eddy and a bottom topography. However, this model is highly idealised and has a few unrealistic aspects. For example,

- In contrast to the discontinuous potential vorticity produced by a step-like topography, a more realistic topography has a continuous one. Additionally, a group velocity of the topographic wave governed by the step-like topography can propagate in only one direction and its property is unrealistic;
- Whereas the f-plane approximation is used, the motion of an eddy in real ocean is strongly influenced by a β-effect.

In this chapter, we investigate the interactions between an upper-layer eddy and a bottom topography using a Gaussian eddy and a sloping bottom topography.

In particular, we classify the motion types occurring in this system and explore their individual properties.

After describing the model configuration in section 3.2, we show the results using an f-plane in section 3.3, and a β-plane in section 3.4. The summary of this chapter is presented in section 3.5.

3.2 Model formulation

In this chapter, we use the two-layer quasi-geostrophic equation in the β-plane. The non-dimensionalised equation and the quasi-geostrophic potential vorticity in the jth layer, q_j, can be written as

$$\frac{\partial q_j}{\partial t} + J(\psi_j, q_j) = -\nu\nabla^6\psi_j + \nabla\cdot(R\nabla\psi_j) \tag{3.1}$$

$$q_1 = \nabla^2\psi_1 - \gamma_L\psi_1 - (\psi_1 - \psi_2) + \beta y, \tag{3.2}$$

$$q_2 = \nabla^2\psi_2 + \gamma_H(\psi_1 - \psi_2) + \beta y + h_B, \tag{3.3}$$

where β is the meridional gradient of the Coriolis parameter, ν is a biharmonic eddy viscosity acting on the relative vorticity to suppress numerical noise at the grid scale, and R is a linear friction coefficient and is only non-zero in the sponge layer. As in the previous chapter, the equations are non-dimensionalised using the length scale $L = \sqrt{g'H_1}/f_0$ and the time scale $T = (f_0\Delta H/H_2)^{-1}$. We scaled the meridional gradient of the Coriolis parameter by $(LT)^{-1} = (f^2/\sqrt{g'H_1})/(\Delta H/H_2)$, the biharmonic eddy viscosity by $L^4T^{-1} = (g'H_1)^2\Delta H/(f^3H_2)$, and the linear friction coefficient by $T^{-1} = f\Delta H/H_2$. Other variables and parameters are the same as in the previous chapter. The model domain is a 25×25 square bounded by slip boundaries. The box is limited at $x = 0$ and $x = 25$ in the x-direction and at $y = -12.5$ and $y = 12.5$ in y-direction. In this model, the no-normal flow and

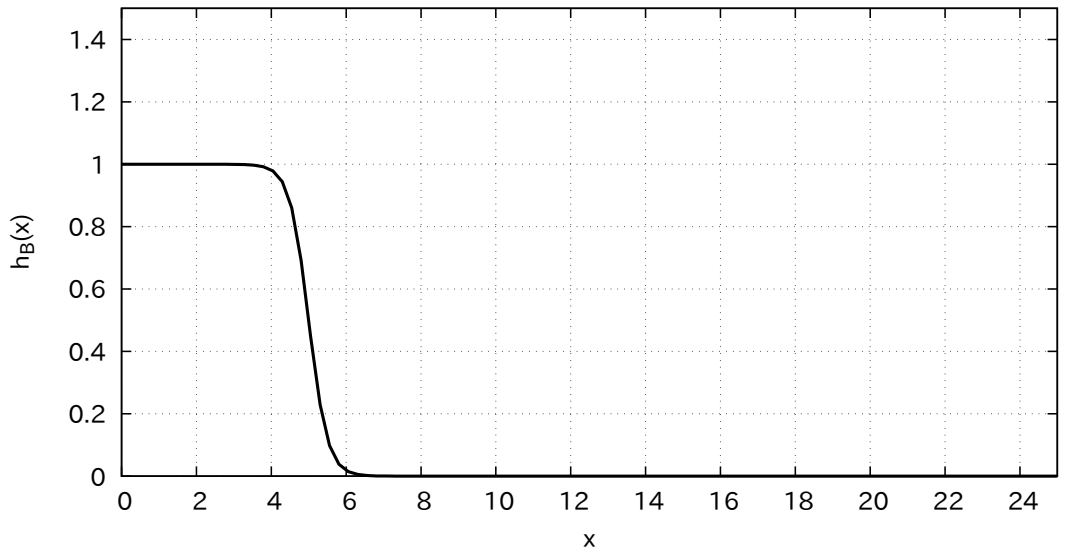

Fig. 3.1: Hyperbolic tangent profile to mimic a bottom topography. The bottom topography idealised by (3.5), where $x_h = 5$, $L_s = 0.5$.

slip boundary conditions are used on all boundaries;

$$\psi_j = 0, \quad \nabla^2 \psi_j = 0, \quad \text{and} \quad \nabla^4 \psi_j = 0 \qquad j = 1, 2. \tag{3.4}$$

We consider an eddy approaching the western region from the open ocean and focus on the interaction between the eddy and a steeply sloping topography. To explore this interaction, we use a hyperbolic tangent function as the bottom topography, so that h_B is written in a non-dimensional form as

$$h_B(x) = -\frac{1}{2}\tanh\left(\frac{x - x_h}{L_s}\right) + \frac{1}{2}, \tag{3.5}$$

where x_h is the centre of the bottom topography and L_s is half of the slope width. We scaled the height of the topography by ΔH. The profile of h_B is shown in figure 3.1.

The eddy is a Gaussian potential vorticity anomaly, and we consider an initial condition q_j satisfying

$$q_1(t=0,x,y) = \varepsilon\,\mathrm{sgn}(\Gamma)\exp\left(-\frac{(x-X_{c,0})^2+(y-Y_{c,0})^2}{L_e^2}\right), \tag{3.6}$$

$$q_2(t=0,x,y) = 0, \tag{3.7}$$

where ε is the non-dimensional amplitude of the Gaussian eddy at the initial time, $(X_{c,0}, Y_{c,0})$ is the initial position of the eddy centre, and L_e is the non-dimensional radius of eddy at initial time. We define $L_d = X_{c,0} - x_h$ as the initial distance between the eddy centre and the centre of the bottom topography. In each layer, the initial streamfunction, ψ_j, is determined to satisfy

$$\nabla^2\psi_1 - \gamma_L\psi_1 - (\psi_1 - \psi_2) = q_1(t=0,x,y), \tag{3.8}$$

$$\nabla^2\psi_2 + \gamma_H(\psi_1 - \psi_2) = q_2(t=0,x,y). \tag{3.9}$$

Figure 3.2 shows the distribution of q_j, ψ_j and the eddy-induced velocity, $\partial\psi_j/\partial x$. A different way of giving an initial eddy in the upper layer is described in appendix A. The controlling non-dimensional parameters in this system are

$$\varepsilon,\ L_s,\ L_d,\ \beta,$$

and we set the remaining parameter values as $\gamma_H = 1$, $\gamma_L = 10^{-3}$, $L_e = 0.5$.

We consider typical values of parameters. In the case that $f = 10^{-4}\,\mathrm{s}^{-1}$, $H_1 = H_2 = 2000\,\mathrm{m}$, $\Delta H = 1000\,\mathrm{m}$, and $g' = 9.8\times10^{-3}\,\mathrm{m/s^2}$, $L \sim 44\,\mathrm{km}$, and $T \sim 2\,\mathrm{day}$. Based on these scales, the dimensional model domain is approximately $1000\,\mathrm{km}\times1000\,\mathrm{km}$. The eddy radius is typically defined as the radius of a closed contour with maximum average speed (e.g., Kurian et al., 2011; Chen and Han., 2019; Ji et al., 2018) and corresponds to L_e. In this study, We set $L_e = 0.5$, which is approximately $22\,\mathrm{km}$. From figure 3.2, the maximum velocity induced by the eddy associated with (3.6) and (3.7) is approximately 0.15ε in the upper

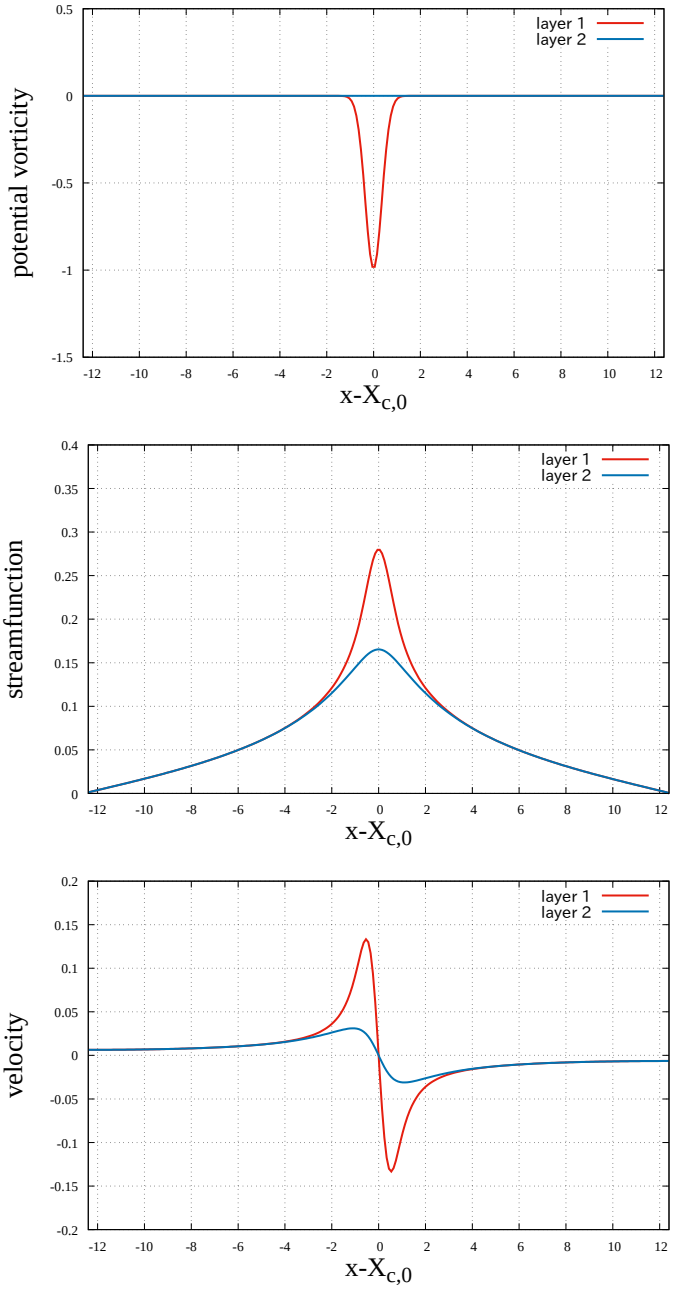

Fig. 3.2: Initial profiles of q_j, ψ_j, and the eddy-induced velocity given by (3.6), (3.7), (3.8), and (3.9) in the section at $y = Y_{c,0}$. The value of $|x - X_{c,0}|$ represents the distance from the eddy centre. The eddy-induced velocity is obtained by $\partial\psi_j/\partial x$. In all panels, the red (blue) lines indicate a profile in the upper (lower) layer. In this case, $\varepsilon = 1$, $L_e = 0.5$, and $(X_{c,0}, Y_{c,0}) = (12.5, 0)$.

layer. Since $L/T \sim 2.2$, the dimensional eddy-induced velocity in this model is approximately $0.33\varepsilon\,\mathrm{ms}^{-1}$. Since realistic swirl velocity ranges are from $0.5\,\mathrm{ms}^{-1}$ to $1.0\,\mathrm{ms}^{-1}$, we set $1 \leq \varepsilon \leq 4$. We estimate the value of L_s based on the slope of the bottom topography used in Itoh and Sugimoto (2001). The bottom topography introduced by them has a height of 3 km and a width of 100 km; thus, the gradient of this slope is 0.03. Since the dimensional gradient of the slope in our model is $\Delta H/(2LL_s)$, by solving $\Delta H/(2LL_s) = 0.03$, the non-dimensional slope-width, L_s, is approximately 0.4. Accordingly, we assume that L_s ranges from 0.25 to 0.5 in this study. Since the meridional gradient of the Coriolis parameter at 40° is approximately $1.6 \times 10^{-11}\,\mathrm{m}^{-1}\mathrm{s}^{-1}$, β is approximately 1.3×10^{-2} in our scaling. Thus, we assume that β ranges from 0.5×10^{-2} to 3×10^{-2} in this study.

3.2.1 Linear waves

In this subsection, we consider a periodic channel in y-direction limited at $x = 0$ and $x = 25$, and examine the waves governed by the linearised equations of (3.1) in the absence of the upper-layer eddy and the β-effect. Wave solutions which are periodic in y and t can be sought in the form

$$\psi_j = \mathrm{Re}\,\phi_j(x)\exp\left\{i(ly - \omega t)\right\}, \quad j = 1, 2. \tag{3.10}$$

where $\phi_j(x)$ is wave amplitudes which vary in x-direction, l is the wave number in y-direction, and ω is the frequency. By substituting the wave solutions into the linearised governing equation, we obtain the equations for ϕ_j,

$$\frac{\mathrm{d}^2\phi_1}{\mathrm{d}x^2} - l^2\phi_1 - (1+\gamma_L)\phi_1 + \phi_2 = 0, \tag{3.11}$$

$$\frac{\mathrm{d}^2\phi_2}{\mathrm{d}x^2} - l^2\phi_2 + \gamma_H\phi_1 - \gamma_H\phi_2 - \frac{l}{\omega L_s}\mathrm{sech}^2\left(\frac{x - x_h}{L_s}\right)\phi_2 = 0. \tag{3.12}$$

These equations with boundary conditions $\phi_j = 0$ at $x = 0$ and $x = 25$ pose an eigenvalue problem with eigenvalues ω^n and eigenfunction ϕ_j^n, where $n =$

$0, 1, 2, 3, \ldots$. By solving this problem numerically using LAPACK (Anderson et al., 1999), we obtain the dispersion relation for the linear topographic Rossby wave in this system. The dispersion curves for this wave, the phase speed, and the group velocity are shown in figure 3.3 and the eigenfunctions are shown in figure 3.4. Unlike the case with the step-like topography in the previous chapter, the group velocity can be positive. The eigenfunctions show that the waves are bottom trapped.

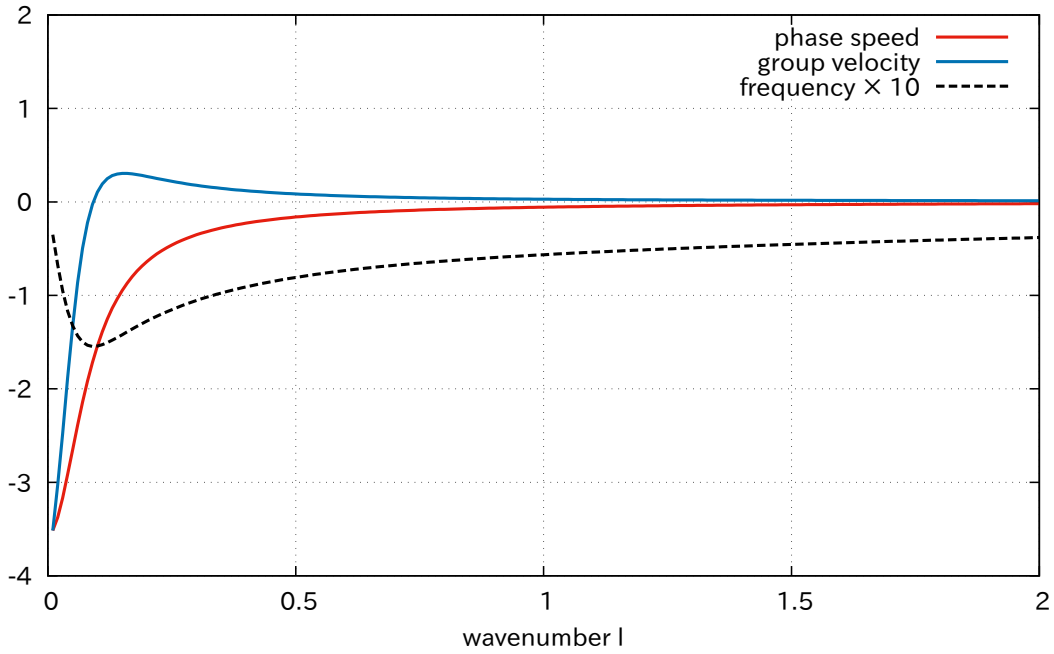

Fig. 3.3: The phase speed (red line), group velocity (blue line), and dispersion curve multiplied by 10 (dashed line) of the topographic Rossby wave ($n = 0$), which are obtained by solving an eigenvalue problem (3.11), (3.12), in the case that $L_s = 0.5$, $x_h = 12.5$. The long topographic Rossby wave speed is approximately -3.52. The maximum group velocity is approximately 0.31 at the wave number $l \approx 0.16$.

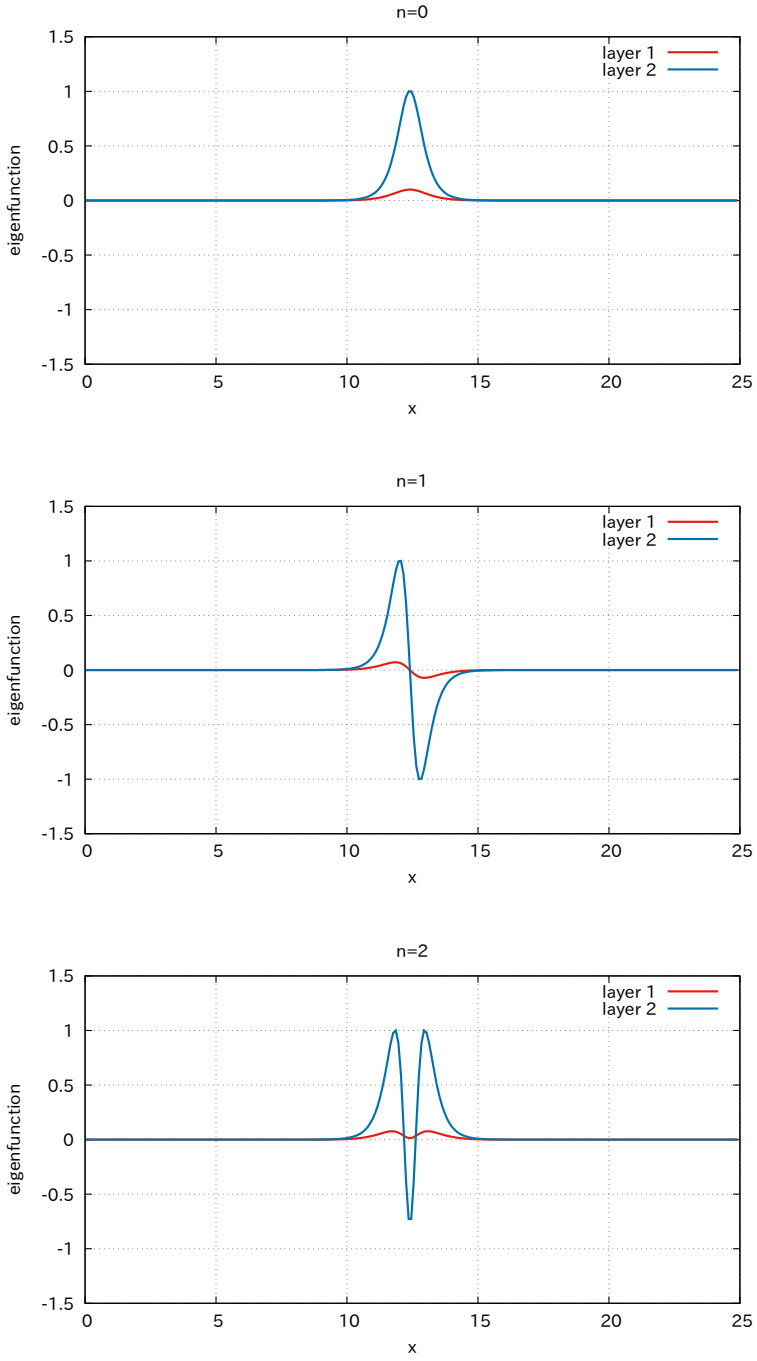

Fig. 3.4: Numerical solutions, ϕ_j^n, of (3.11) and (3.12) in the case that $x_h = 12.5$, $L_s = 0.5$, and $l = 4\pi/5$. These solutions are normalised by the maximum value of ϕ_2^n. The red (blue) lines indicate the upper (lower) layer.

3.2.2 Numerical scheme

In this subsection, we describe the numerical methods used in the following numerical experiments. We solve (3.1) on a 256×256 grid. The fourth-order Runge–Kutta scheme is used for time integration, with a time step of $\Delta t = 0.01$. The Arakawa Jacobian is used for the expression of the advective term (Arakawa, 1966). At each time step, the streamfunction, ψ_j, must be obtained from the potential vorticity, q_j by solving (3.8) and (3.9). By defining the potential vorticity anomaly, $q_1' \equiv q_1 - \beta y$ and $q_2' \equiv q_2 - \beta y - h_B$, we obtain

$$q_1' = \nabla^2 \psi_1 - \gamma_L \psi_1 - (\psi_1 - \psi_2), \tag{3.13}$$

$$q_2' = \nabla^2 \psi_2 + \gamma_H (\psi_1 - \psi_2). \tag{3.14}$$

The potential vorticity anomaly can be decomposed into vertical modes by using eigenvalues and eigenvectors, $\lambda_\pm$ and $\vec{V}_\pm$, as in (2.12) and (2.13). We define the potential vorticity anomaly and the streamfunction of $+$ and $-$ modes as

$$q_\pm' = U_\pm q_1' + V_\pm q_2', \tag{3.15}$$

$$\psi_\pm = U_\pm \psi_1' + V_\pm \psi_2'. \tag{3.16}$$

Using $q_\pm'$ and $\psi_\pm$, we obtain

$$q_\pm' = \nabla^2 \psi_\pm - \lambda_\pm \psi_\pm, \tag{3.17}$$

which are known as the Helmholtz equations. We can obtain $\psi_\pm$ by solving these Helmholtz equations in each mode. This calculation is performed using the same method as in Q-GCM, as described in Hogg et al. (2003). We use LAPACK and FFTPACK (Swarztrauber 1982) to calculate the Helmholtz equations numerically. Using (3.16), we can obtain ψ_j.

In numerical experiments, a sponge layer is introduced a short distance from the boundary to the interior. The purpose of the sponge layer is to remove the

wave reflection and to reduce the influence of the boundary on the interior flow field. The structure of the sponge layer is represented by the distribution of R in (3.1). In this study, the sponge layers are 2.5 non-dimensional distances from the boundary to the interior. In the sponge layer, the linear friction coefficient, R, has a non-zero value, as shown in figure 3.5. After conducting a series of experiments with different widths of the sponge layer, we determined this value.

The accuracy of the calculation is verified by comparing the phase speed of a small-amplitude topographic Rossby wave in the absence of an upper-layer eddy calculated by the numerical experiment with the results in subsection 3.2.1 (figure 3.3). To verify the accuracy, we conduct a few numerical experiments using a 512×512 grid and $\Delta t = 0.005$. A few numerical experiments with fixed grid interval and doubled domains confirm that the boundaries have little influence on the results.

3.3 Numerical experiments on an f-plane

In this section, we show the results of numerical experiments on an f-plane. The numerical experiments were conducted until $t = 600$.

3.3.1 An anticyclonic Gaussian eddy

We consider the case of an anticyclonic eddy, that is, $\mathrm{sgn}(\Gamma) = -1$, with $\varepsilon = 1$. Figure 3.6 shows the temporal evolution of the potential vorticity, q_2, in the lower layer. The trajectories of the upper-layer eddy with $\varepsilon = 1, 3$ are obtained by tracking the minima of q_1, as shown in figure 3.7.

In the early stage, the advection due to the upper-layer eddy exists in the direction towards the deep side for $y > Y_c$ and in the direction towards the shallow side for $y < Y_c$, where (X_c, Y_c) denotes the location of the minima of q_1, that

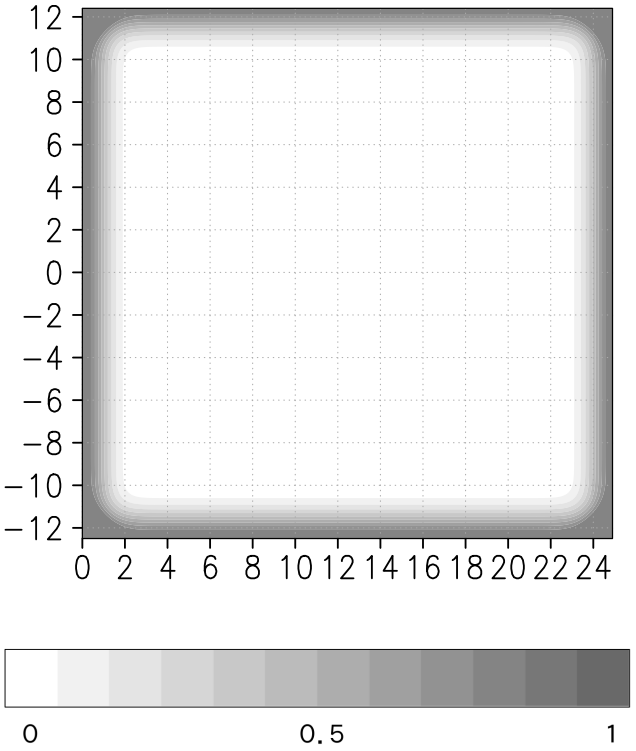

Fig. 3.5: The distribution of the non-dimensional value of the linear friction coefficient, R, in this model. R has the value in both layers. The width of the sponge layer is 2.5.

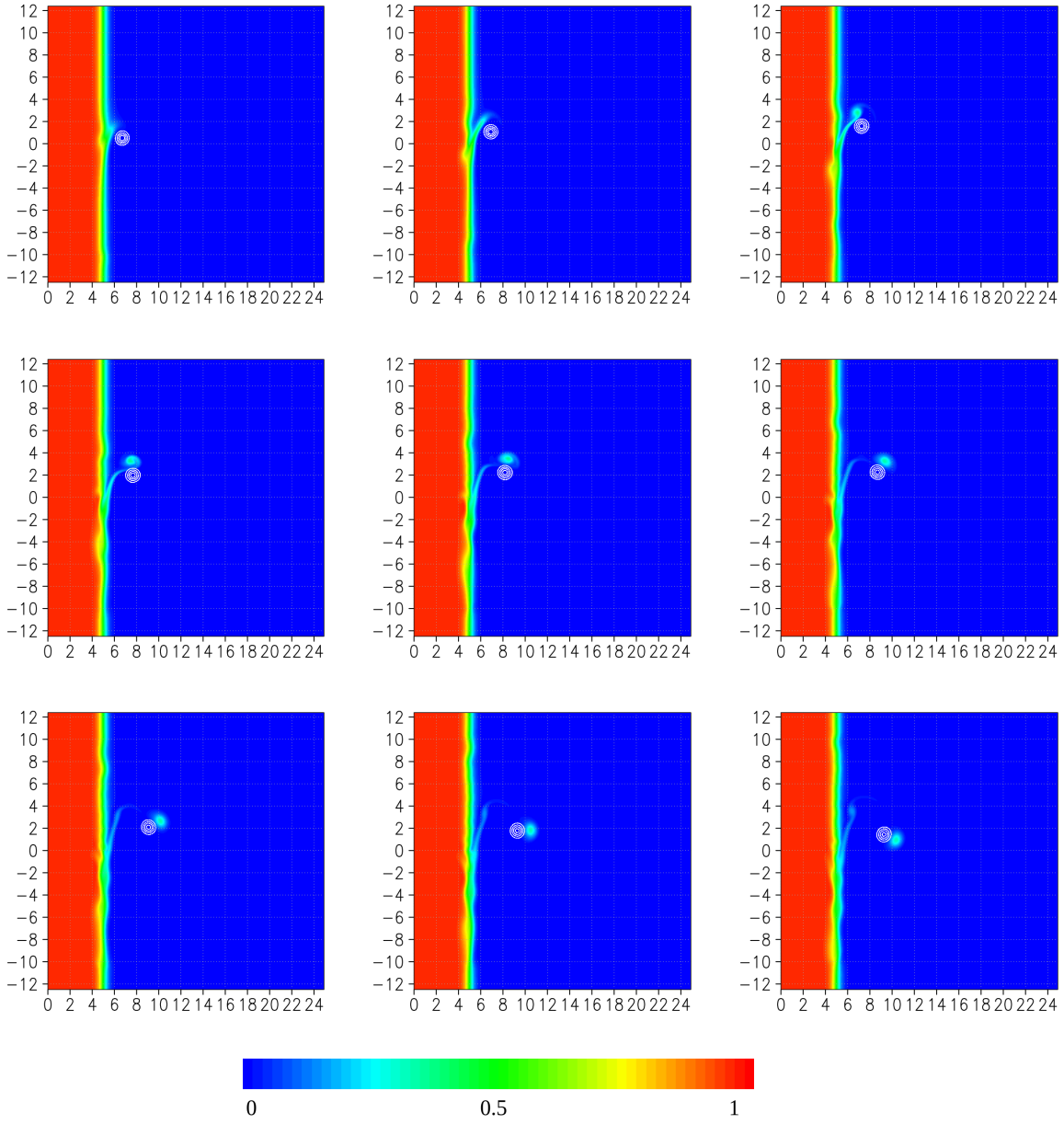

Fig. 3.6: The temporal evolution of the potential vorticity field in the lower layer, q_2, and the anticyclonic eddy with $\varepsilon = 1$ in the upper layer. White lines indicate the contour of $q_1 = -0.8, -0.6, -0.4, -0.2$. From left to right, (top) $t = 40$, $t = 80$, $t = 120$; (middle) $t = 160$, $t = 200$, $t = 240$; (bottom) $t = 280$, $t = 320$, $t = 360$. In this case, $x_h = 5$, $L_s = 0.5$, $L_d = 1.5$ and $\beta = 0$.

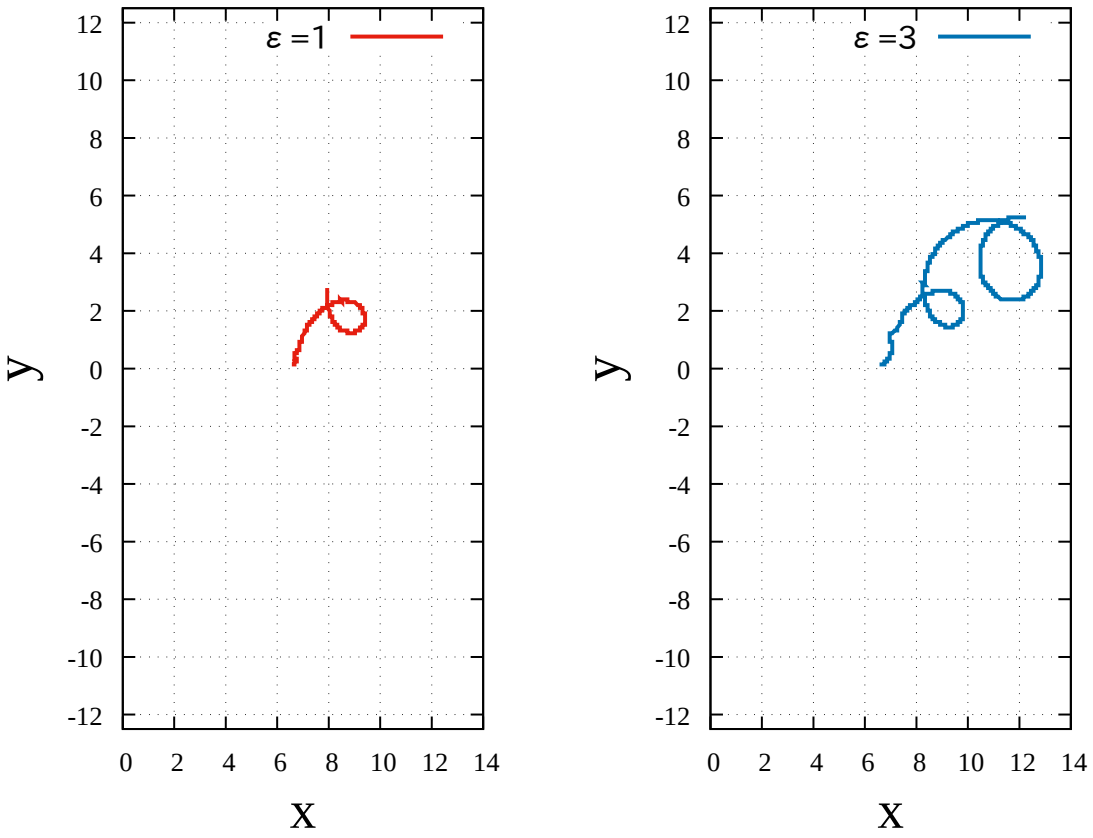

Fig. 3.7: The trajectory of the anticyclonic upper-layer eddy in the case of $\varepsilon = 1$ (left) and $\varepsilon = 3$ (right). Other parameters are the same as in figure 3.6. In both panels, the initial position of the upper-layer eddy is $(X_{c,0}, Y_{c,0}) = (6.5, 0)$.

is, the location of the upper-layer eddy. The potential vorticity anomaly on the deeper side of the slope is trapped on the slope region, i.e., this anomaly cannot propagate in the negative y direction as the topographic Rossby wave, but one on the shallower side of the slope propagates as the topographic Rossby wave. After this stage, the high potential vorticity fluid in the deeper side of the slope is elongated by the upper-layer eddy, becoming an isolated eddy out of the slope region. This isolated eddy forms a dipole structure with the upper-layer eddy. Further, this dipole structure causes the upper-layer eddy to move away from the topography. Figure 3.7 shows the trajectory of the upper-layer eddy. The dipole structure propagates in the opposite direction to the topographic Rossby wave along the topography with anticyclonic rotation, since the two eddies consisting of the dipole structure are not balanced in their strength. The dipole formation always occurs on the f-plane in the parameter, ε, within the range of this study.

These results indicate that the interaction between the upper-layer eddy and the sloping bottom topography forms heton-type motion independent of the strength of the eddy. This differs from the results in the previous chapter in the case of interactions between the point vortex and step-like topography, which suggest that the ratio of the strength of the point vortex and the height of the topography determines the motion type occurring in the system. The sloping topography is interpreted as a stair-step (figure 3.8). In other words, the distribution of q_2 can be interpreted as a situation in which a large number of the potential vorticity fronts are parallel to each other. Based on this interpretation, the heton-type motion can form even for weak eddies, as there are fronts corresponding to the small topography. Therefore, the results suggest that the formation of heton-type motion is a common phenomenon in the interaction between the upper-layer eddy and the sloping bottom topography.

Figure 3.9 shows the trajectories of the upper-layer eddy for the sloping width,

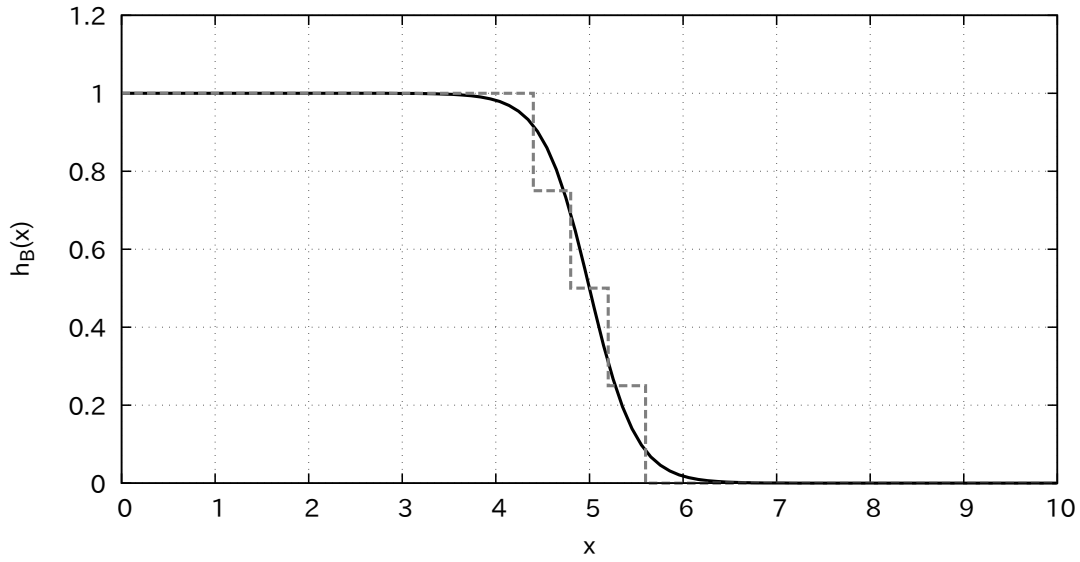

Fig. 3.8: Example of representing the sloping bottom topography as a stair-step. The solid line is the bottom topography, $h_B(x)$, where $x_h = 5$ and $L_s = 0.5$, and the dashed line is the stair-step profile.

$L_s = 0.25, 0.5$, and for the initial distance between the upper-layer eddy and the sloping topography, $L_d = 1.5, 3, 4.5$. The results indicate that the upper-layer eddy moves along the topography over a longer distance when L_s is smaller, that is, the behaviour of the upper-layer eddy approaches that of the case with the step-like topography when the slope becomes steeper. Decreasing L_s corresponds to reducing the difference in velocity due to the upper-layer eddy at the deep and shallow sides of the slope. The results also indicate that the upper-layer eddy moves along the topography over a longer distance when L_d is larger. From Fig. 3.2, the further away from the eddy, the slower the spatial variation in the eddy-induced velocity in the low layer becomes since the barotropic mode dominates at a large distance from the centre of the upper-layer eddy. As a consequence,

increasing L_d reduces the difference in velocity due to the upper-layer eddy across the topography and leads to the same result as decreasing L_s. Hence, the behaviour of the upper-layer eddy approaches that of the case with the step-like topography when L_s is smaller and L_d is larger.

3.3.2 A cyclonic Gaussian eddy

We consider the case of the cyclonic eddy in the upper layer, that is, $\mathrm{sgn}(\Gamma) = 1$. Figure 3.10 shows the temporal evolution of the potential vorticity, q_2, while figure 3.11 shows the trajectories of the upper-layer eddy with $\varepsilon = 1, 3$. In this case, the upper-layer eddy propagates along the topography in the same direction of the topographic Rossby wave, forming a low-potential vorticity anomaly on the slope, similar to the pseudoimage in a previous chapter (see also figure 2.20). The propagation speed is approximately 1.5×10^{-2}, which is much smaller than that of the long topographic Rossby wave, $|\omega^0/l| \approx 3.5$. From figure 3.11, the upper-layer eddy approaches the topography initially but cannot move onto the slope region in the computational time. From the results of the previous chapter, when the upper-layer eddy enters the shallow side, this forms the dipole structure with the lower-layer eddy generated by the advection of the low potential vorticity fluid across the topography. However, in the present case, the width of the slope prevents the upper-layer eddy from advecting the low potential vorticity fluid to the shallow side before the lower-layer structure is adjusted by the topographic Rossby wave. Therefore, the upper-layer eddy cannot move into the shallow side, propagating in the only direction along the topography.

Figure 3.12 shows the trajectories of the upper-layer eddy for the slope widths, $L_s = 0.25, 0.5$, and for the initial distance between the upper-layer eddy and the sloping topography, $L_d = 1.5, 3, 4.5$. The tendency of the eddy to approach the topography becomes smaller when L_s is smaller (i.e., the slope becomes steeper),

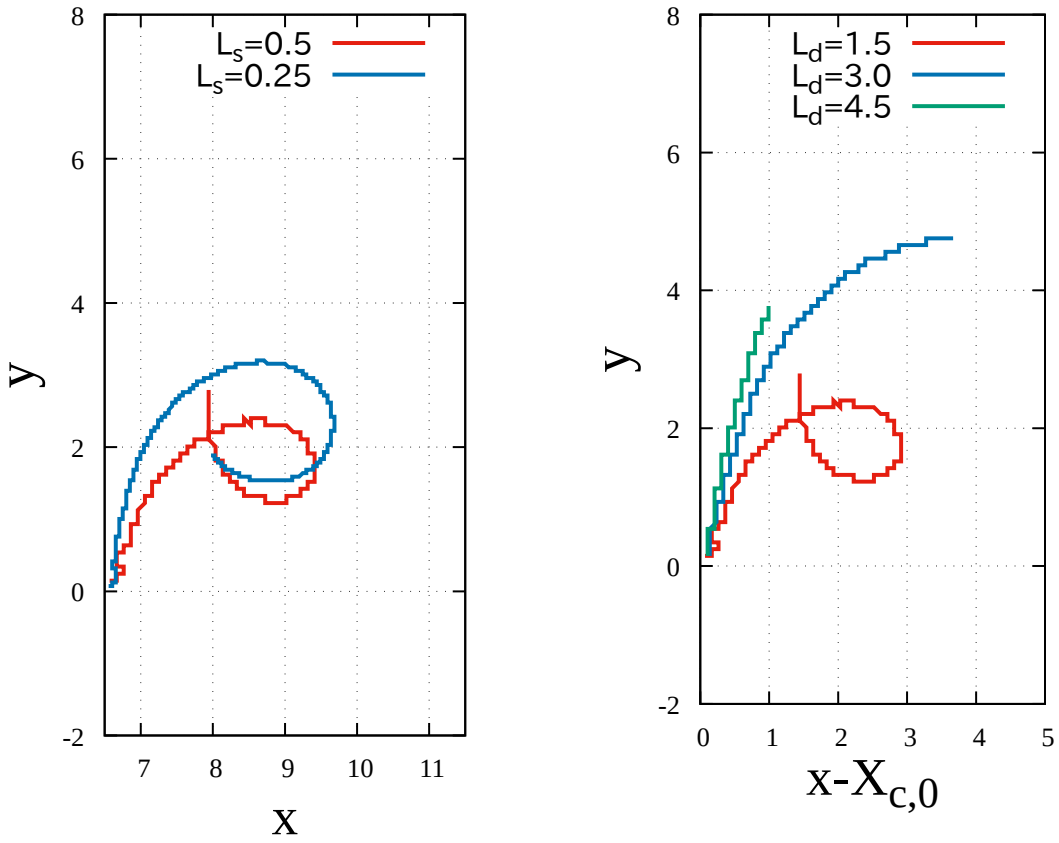

Fig. 3.9: The trajectory of the anticyclonic upper-layer eddy with $\varepsilon = 1$ in the case of $L_s = 0.25, 0.5$ are indicated by the red and blue lines, respectively (left); and $L_d = 1.5, 3, 4.5$ are indicated by the red, blue, and green lines, respectively (right). The calculation with $L_s = 0.25$ in the left panel is conducted with $\Delta x = \Delta y = 25/512$ and $\Delta t = 0.005$ to maintain the resolution of the sloping topography. Other parameters are the same as in figure 3.6. The horizontal axis in the right panel is set by $x - X_{c,0}$ to the starting points of the upper-layer eddy in each experiment.

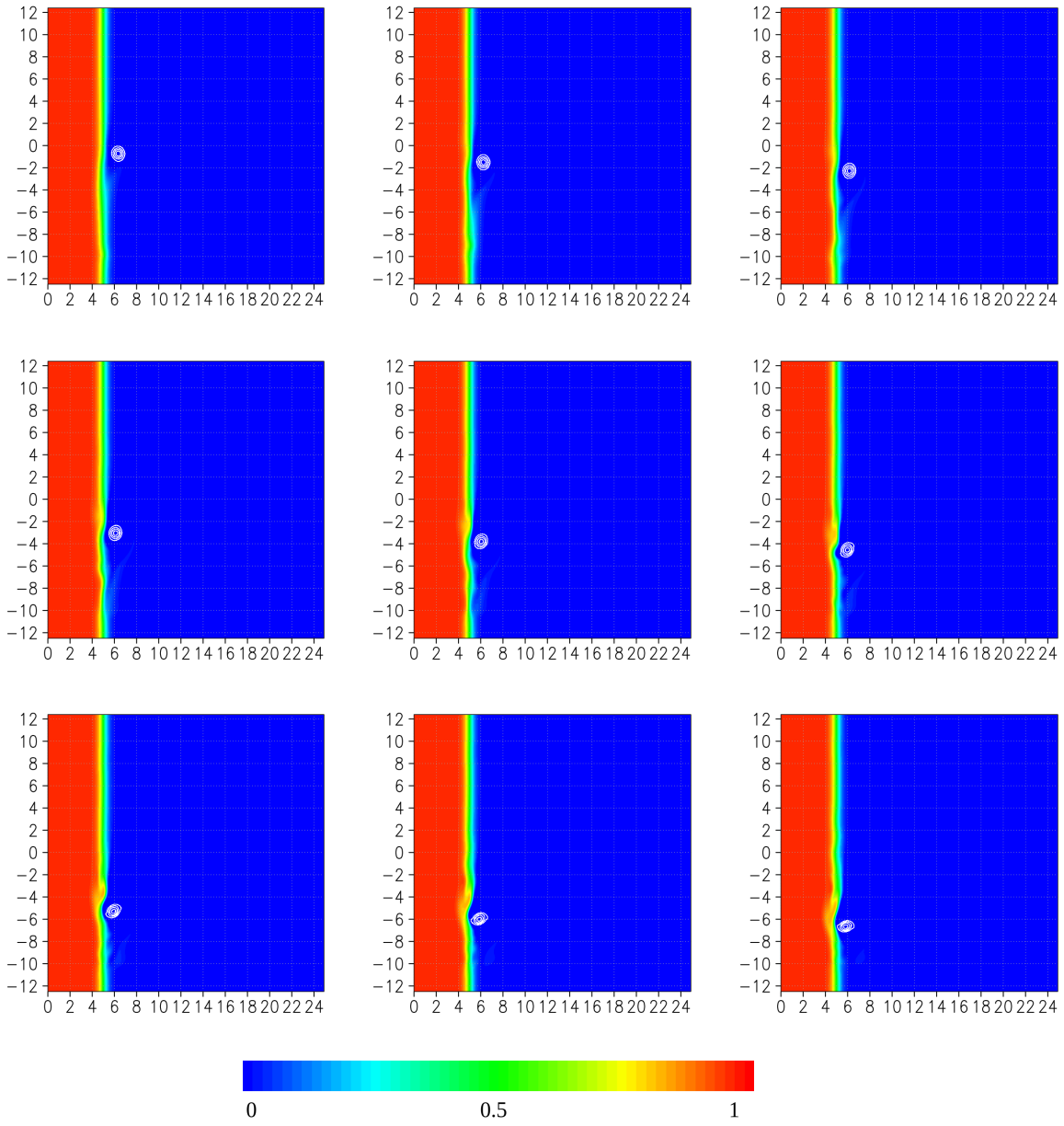

Fig. 3.10: The temporal evolution of the potential vorticity field in the lower layer, q_2, and the cyclonic eddy with $\varepsilon = 1$ in the upper layer. White lines indicate the contour of $q_1 = 0.2, 0.4, 0.6, 0.8$. From left to right, (top) $t = 50$, $t = 100$, $t = 150$; (middle) $t = 200$, $t = 250$, $t = 300$; (bottom) $t = 350$, $t = 400$, $t = 450$. In this case, $x_h = 5$, $L_s = 0.5$, $L_d = 1.5$ and $\beta = 0$.

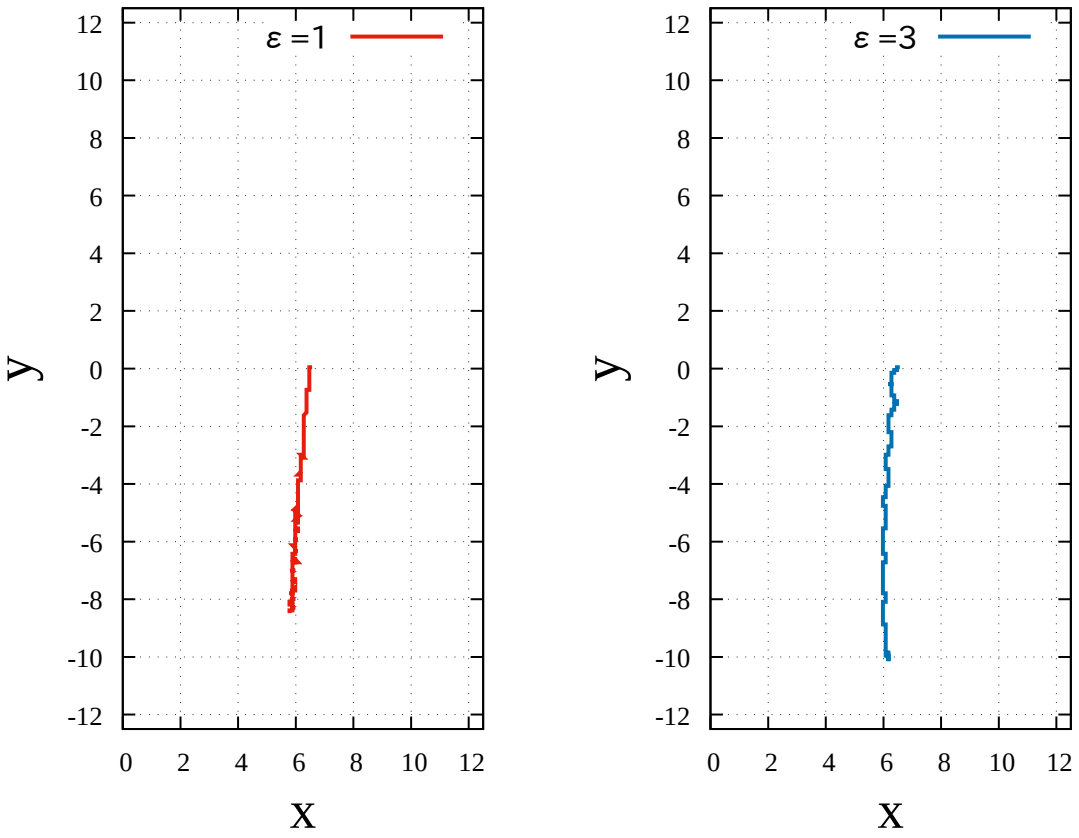

Fig. 3.11: The trajectory of the cyclonic upper-layer eddy in the case of $\varepsilon = 1$ (left) and $\varepsilon = 3$ (right). Other parameters are the same as in figure 3.10. The initial position of the upper-layer eddy is $(X_{c,0}, Y_{c,0}) = (6.5, 0)$

or L_d is larger. As in the case of the anticyclonic eddy, both decreasing L_s and increasing L_d correspond to reducing the difference in velocity due to the upper-layer eddy at deep and shallow sides of the topography. Thus, the behaviour of the upper-layer eddy approaches that of the case with the step-like topography when L_s is small and L_d is large, regardless of the sign of the eddy rotation.

3.4 Numerical experiments on a β-plane

In this section, we investigate interactions between the upper-layer eddy and the sloping bottom topography on a β-plane.

3.4.1 An anticyclonic Gaussian eddy

We consider the case of an anticyclonic eddy, that is, $\mathrm{sgn}(\Gamma) = -1$, and show two typical motions in the interactions on a β-plane. Figure 3.13 shows the temporal evolution of the potential vorticity, $q_2 - \beta y$, in the lower layer for $\varepsilon = 1$, $\beta = 10^{-2}$, $L_d = 3$. Figure 3.14 shows the trajectory of the upper-layer eddy in this case. The propagation tendency of the anticyclonic nonlinear eddy associated with the planetary β effect is southwestward. Even after approaching the topography, the upper-layer eddy maintains this propagation tendency and eventually reaches the western boundary. As the eddy approaches the topography, the high potential vorticity fluid on the slope is advected to the deeper side. In this case, since the upper-layer eddy cannot obtain a sufficient amount of the high-potential vorticity fluid for the dipole structure propagating eastward to form, the eddy moves onto the slope region and the potential vorticity anomaly in the lower layer propagates as the topographic Rossby wave. Consequently, the eddy cannot propagate away from the topography and reaches the western boundary.

Figures 3.15 and 3.16 show the results for $\varepsilon = 3$, $\beta = 10^{-2}$, $L_d = 3$. As in the

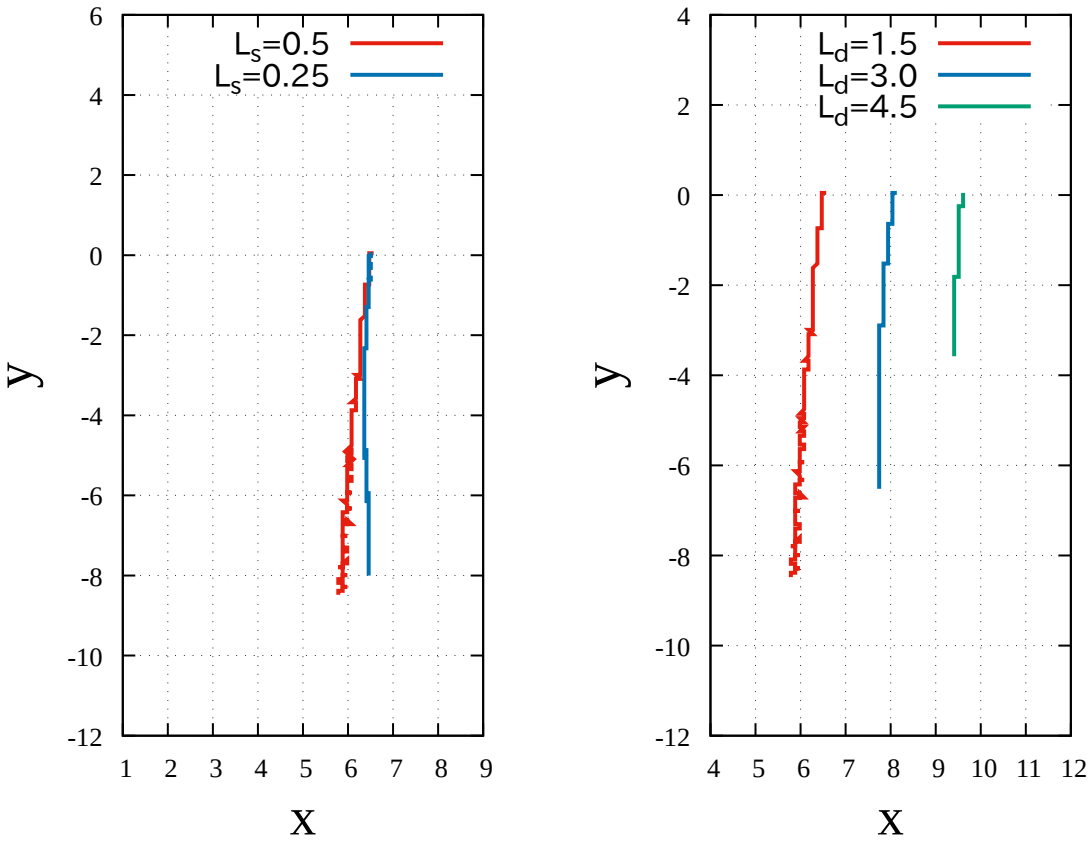

Fig. 3.12: The trajectory of the cyclonic upper-layer eddy with $\varepsilon = 1$ in the case of $L_s = 0.25, 0.5$ are indicated by the red and blue lines, respectively (left) and $L_d = 1.5, 3, 4.5$ are indicated by red, blue, and green lines, respectively (right). The calculation with $L_s = 0.25$ in the left panel is conducted with $\Delta x = \Delta y = 25/512$ and $\Delta t = 0.005$ to maintain the resolution of the sloping topography. Other parameters are the same as in figure 3.10.

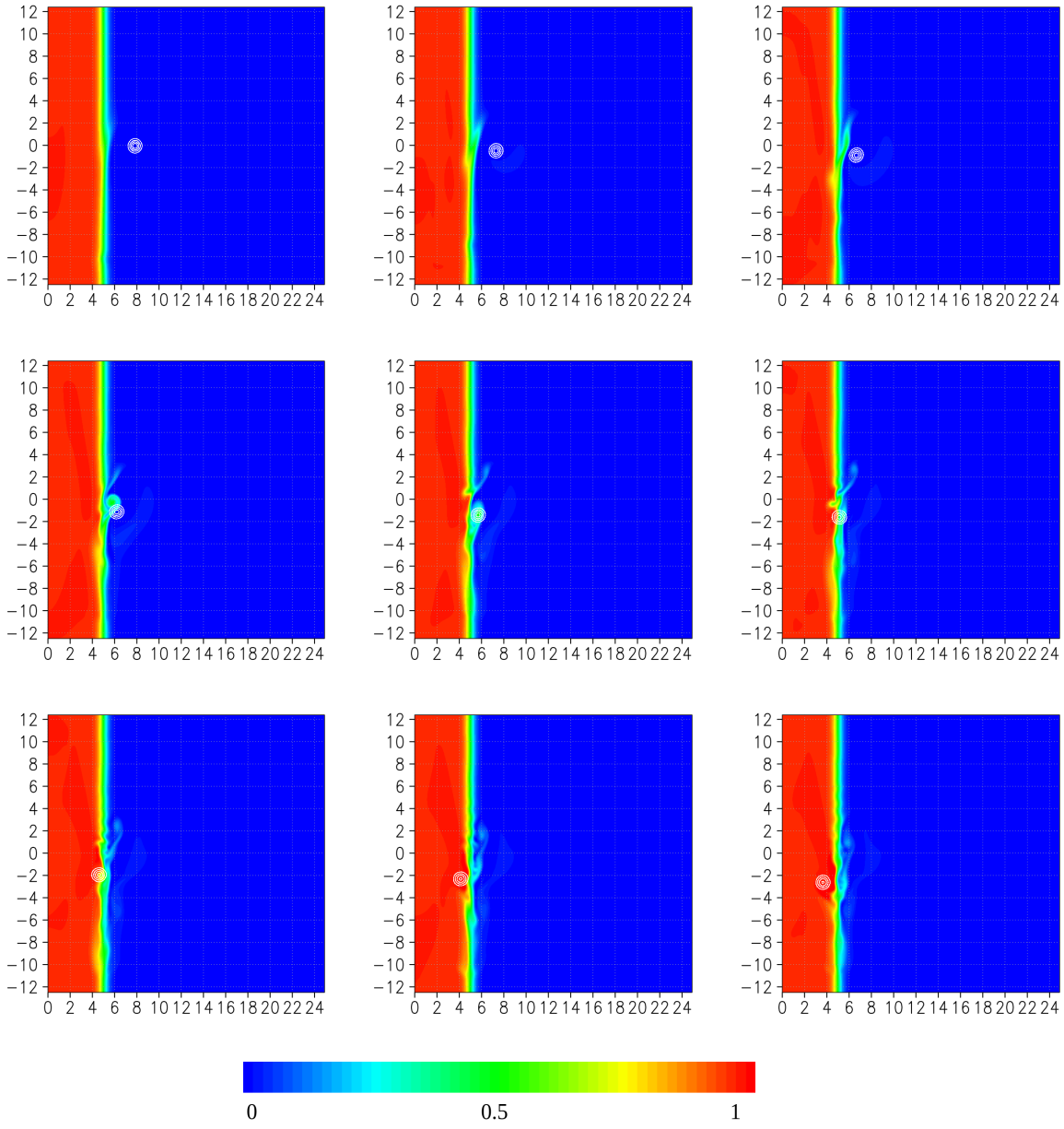

Fig. 3.13: The temporal evolution of the potential vorticity field in the lower layer, $q_2 - \beta y$, and the anticyclonic eddy with $\varepsilon = 1$ in the upper layer. White lines indicate the contour of $q_1 - \beta y = -0.8, -0.6, -0.4, -0.2$. From left to right, (top) $t = 50$, $t = 100$, $t = 150$; (middle) $t = 200$, $t = 250$, $t = 300$; (bottom) $t = 350$, $t = 400$, $t = 450$. In this case, $x_h = 5$, $L_s = 0.5$, $L_d = 3$ and $\beta = 10^{-2}$.

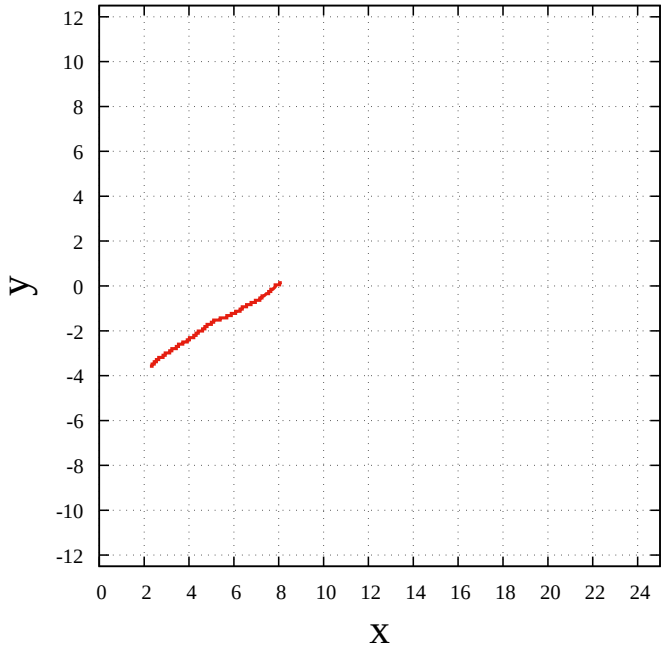

Fig. 3.14: The trajectory of the upper-layer eddy in figure 3.13. The initial position of the eddy is $(0, 8)$.

case that $\varepsilon = 1$, the upper-layer eddy initially moves westward. However, it forms a dipole structure on the east of the topography with a cyclonic eddy generated by potential vorticity conservation, moving eastward as the heton-like eddy pair. This dipole propagates eastward and reaches the eastern boundary. Therefore, the heton-type motion can exist on the β-plane. This motion is identical to the heton-type motion on the f-plane, except that it can propagate eastward over a long distance. The existence of the β effect (i.e., background potential vorticity gradient) and the nonlinear effect seem essential for the long-distance eastward motion of the heton-like dipole, as in the eastward motion of modons.

3.4.2 A cyclonic Gaussian eddy

We consider the case of a cyclonic eddy, that is, $\mathrm{sgn}(\Gamma) = 1$, on a β-plane. Figure 3.17 shows the temporal evolution of the potential vorticity, $q_2 - \beta y$ for $\varepsilon = 1$, $\beta = 10^{-2}$, $L_d = 3$. Figure 3.18 shows the trajectory of the upper-layer eddy in this case. The upper-layer eddy propagates northwestward, crossing the topography. Before crossing the topography, the eddy advects the fluid on the slope; however, the anticyclonic eddy in the lower layer generated by the upper-layer eddy is small, propagating as the topographic Rossby wave. Figures 3.19 and 3.20 show the case that $\varepsilon = 3$. Unlike the case with $\varepsilon = 1$, the strong interaction with the bottom topography causes the southward propagation, as seen in the f-plane case (Fig. 3.10), while it continuously propagates westward due to the β-effect. Immediately after entering the shallow side, the upper-layer eddy attracts the low potential vorticity fluid. Simultaneously, the dipole structure observed in the previous chapter is present (see figure 2.22). However, since the lower-layer potential vorticity anomaly propagates as the topographic Rossby wave, the upper-layer eddy can attract only a small amount of the low-potential vorticity fluid in the lower layer so that the lower-layer anticyclonic is much weaker than the upper-

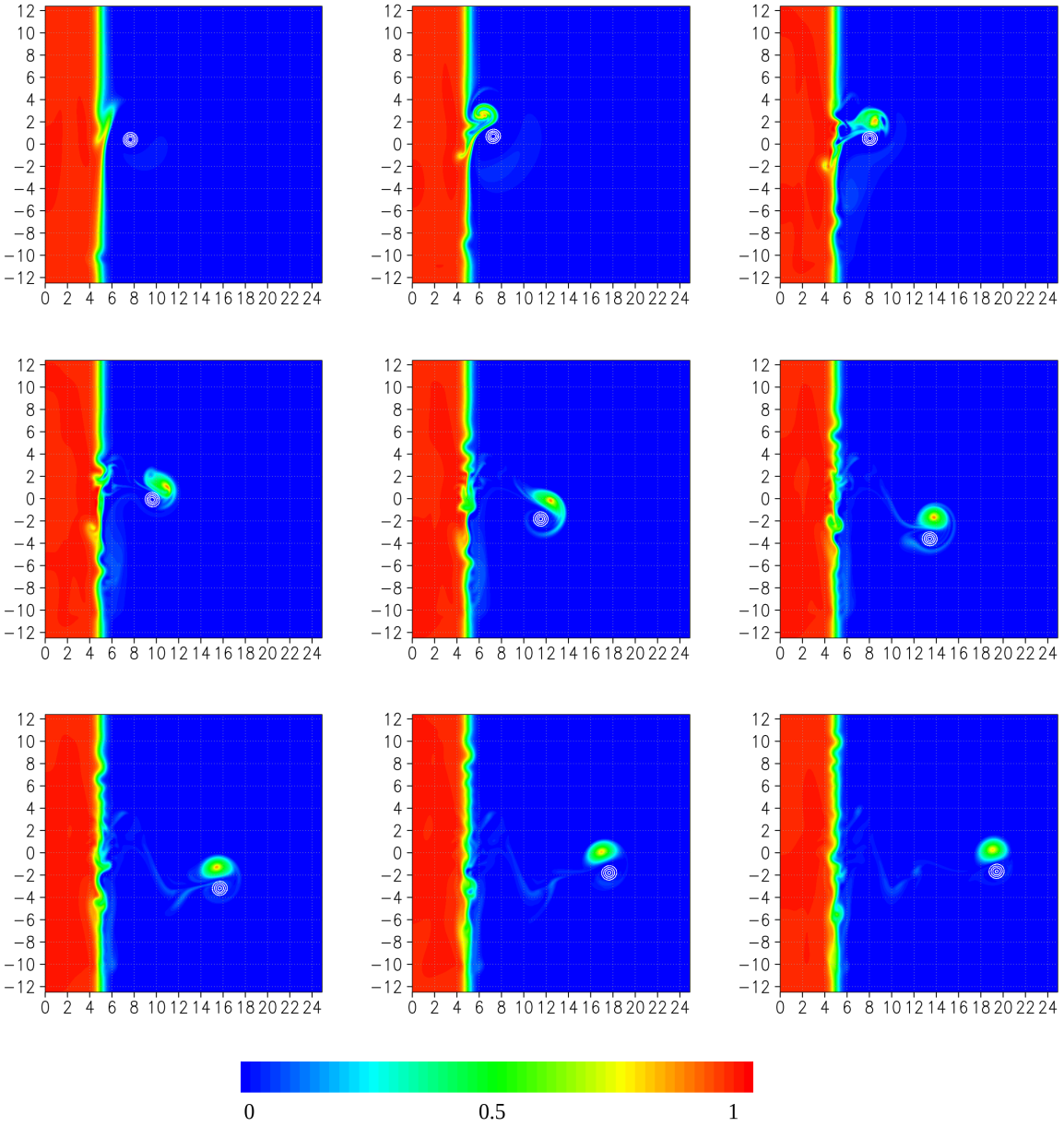

Fig. 3.15: The temporal evolution of the potential vorticity field in the lower layer, $q_2 - \beta y$, and the anticyclonic eddy with $\varepsilon = 1$ in the upper layer. White lines indicate the contour of $q_1 - \beta y = -2.4, -1.8, -1.2, -0.6$. As in figure 3.13, except for $\varepsilon = 3$.

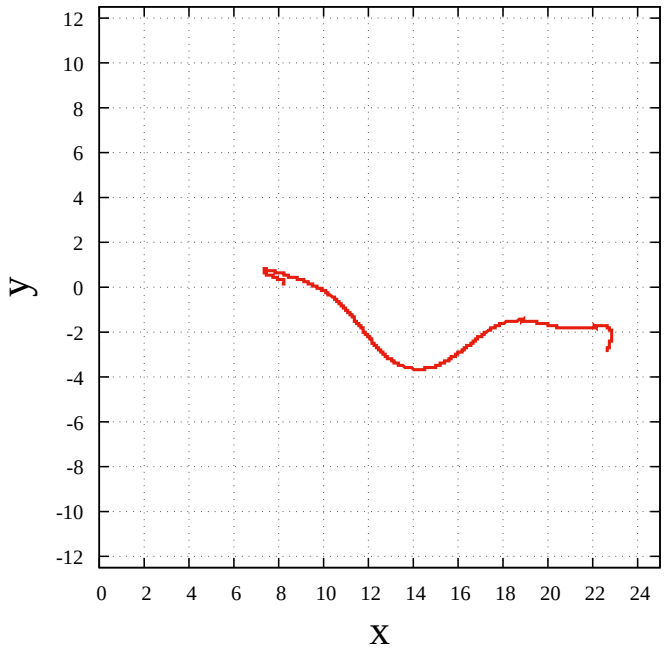

Fig. 3.16: As in Figure 3.14, except for $\varepsilon = 3$.

layer cyclonic eddy. Although the lower-layer eddy affects the upper-layer eddy motion, the upper-layer eddy propagates largely northwestward by the β-effect since the influence of the lower-layer eddy is small, even when ε is large. This result suggests that the influence of the sloping topography on the behaviour of a cyclonic upper-layer eddy on the β-plane is small.

3.4.3 Classification of the motion based on ε and β

In this subsection, we conduct numerical experiments with ε and β as parameters and classify the motion types in ε-β space. We consider the case of an anticyclonic eddy (i.e., $\mathrm{sgn}(\Gamma) = -1$), since we see that the motion of an anticyclonic eddy is significantly affected by the amplitude of ε and the presence or absence of a β-effect, in contrast to the case of a cyclonic eddy in a previous subsection. Figure 3.21 shows the distribution of the typical motion types in ε-β space, and that the

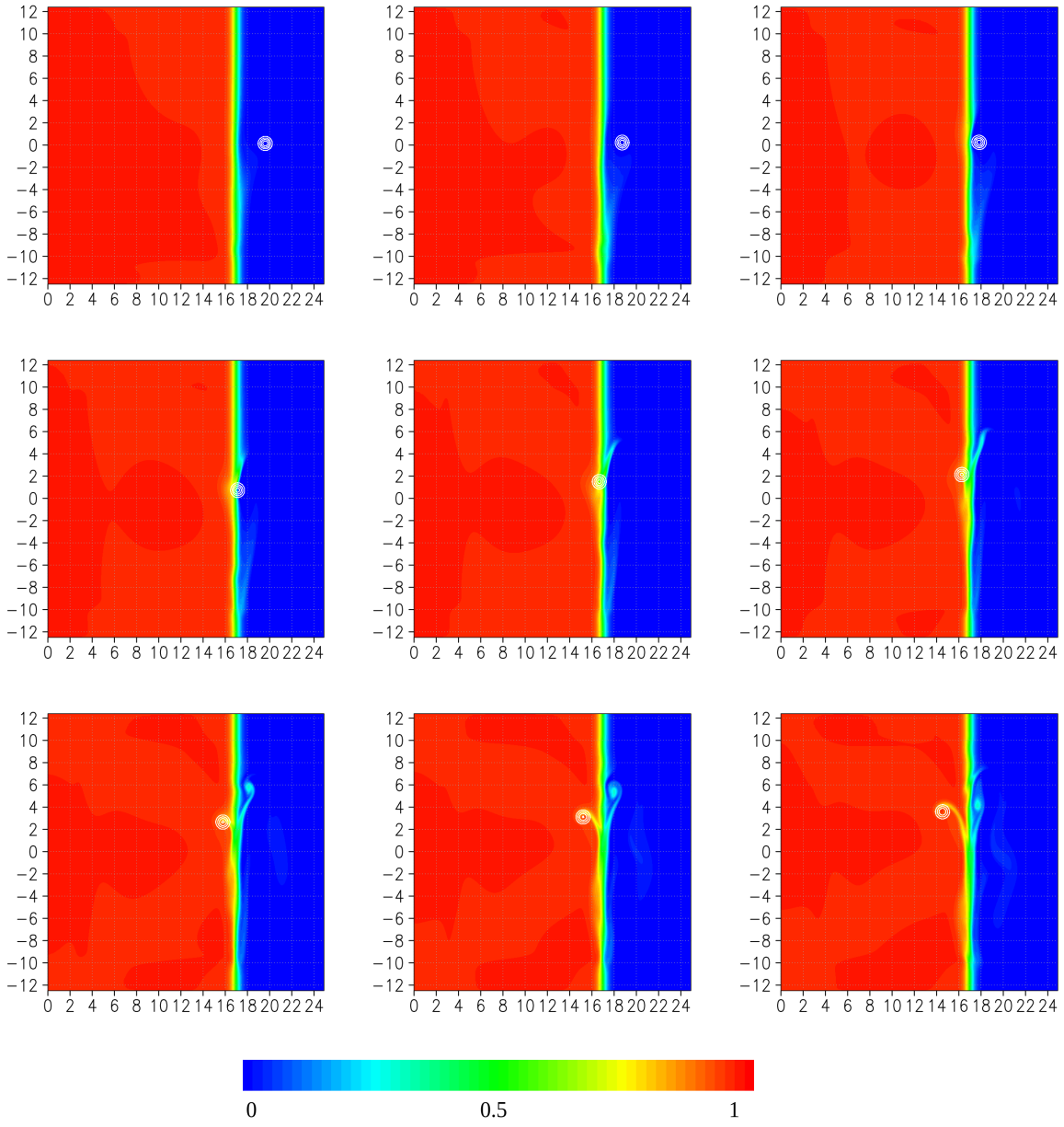

Fig. 3.17: The temporal evolution of the potential vorticity field in the lower layer, $q_2 - \beta y$, and the cyclonic eddy with $\varepsilon = 1$ in the upper layer. White lines indicate the contour of $q_1 - \beta y = 0.2, 0.4, 0.6, 0.8$. From left to right, (top) $t = 60$, $t = 120$, $t = 180$; (middle) $t = 240$, $t = 300$, $t = 360$; (bottom) $t = 420$, $t = 480$, $t = 540$. In this case, $x_h = 17$, $L_s = 0.5$, $L_d = 3$ and $\beta = 10^{-2}$.

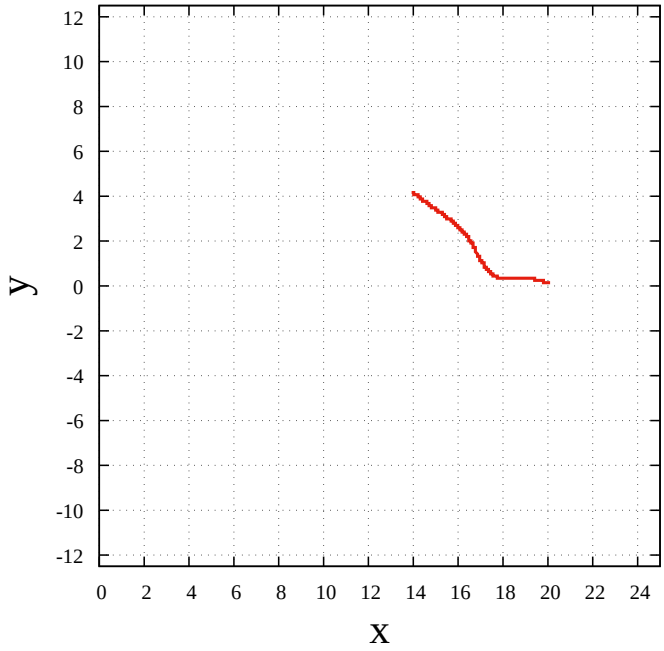

Fig. 3.18: The trajectory of the upper-layer eddy in figure 3.17. The initial position of the eddy is $(0, 20)$.

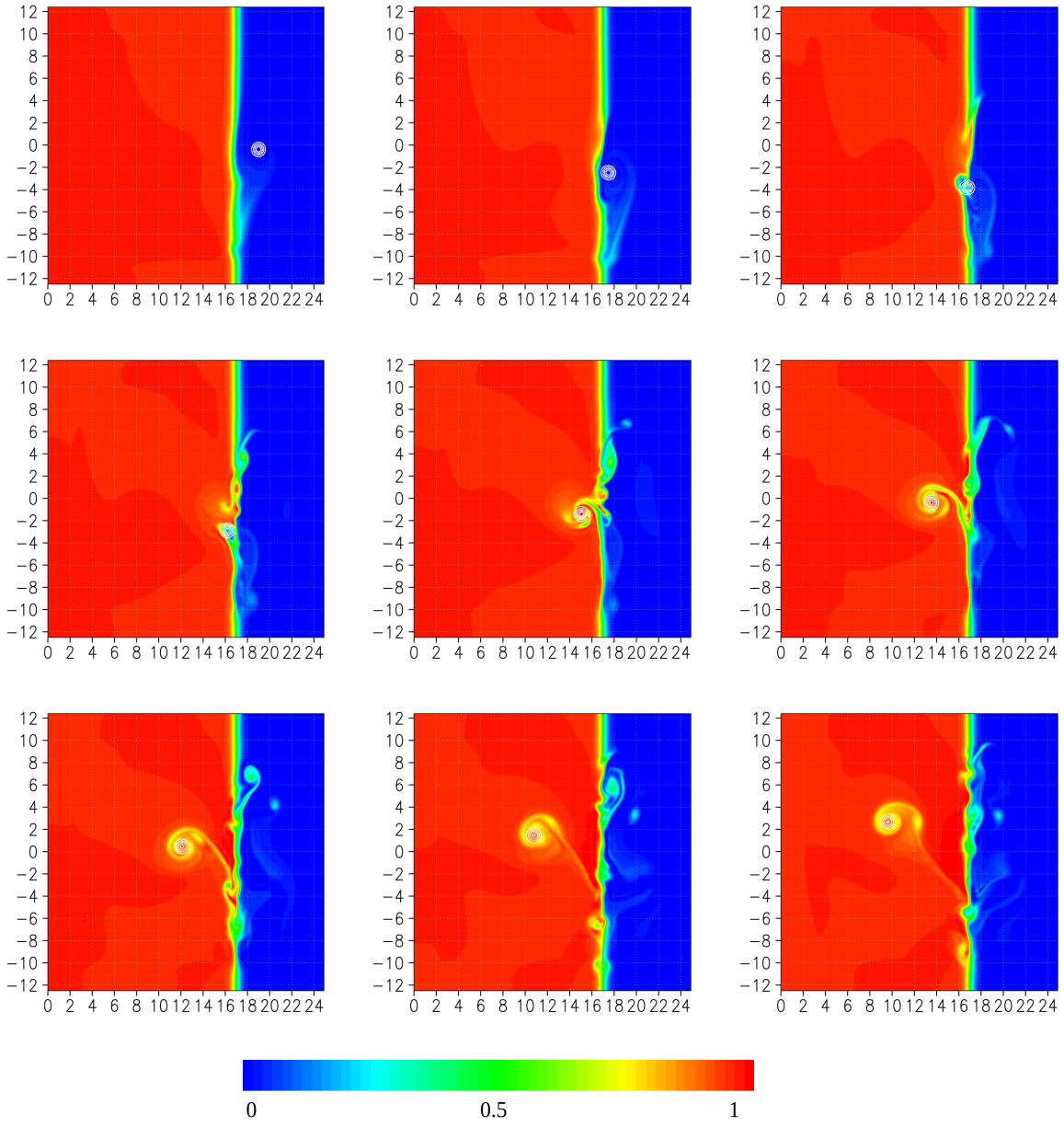

Fig. 3.19: The temporal evolution of the potential vorticity field in the lower layer, $q_2 - \beta y$, and the cyclonic eddy with $\varepsilon = 3$ in the upper layer. White lines indicate the contour of $q_1 - \beta y = 0.2, 0.4, 0.6, 0.8$. From left to right, (top) $t = 60$, $t = 120$, $t = 180$; (middle) $t = 240$, $t = 300$, $t = 360$; (bottom) $t = 420$, $t = 480$, $t = 540$. In this case, $x_h = 17$, $L_s = 0.5$, $L_d = 3$ and $\beta = 10^{-2}$.

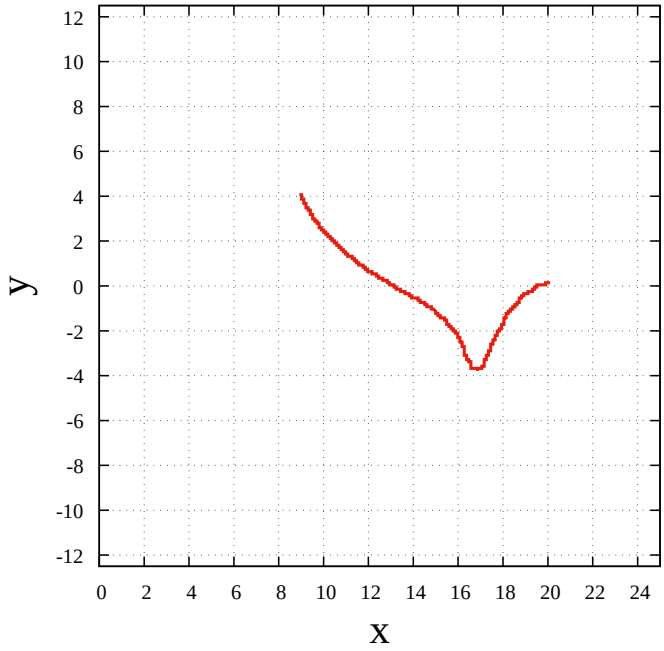

Fig. 3.20: The trajectory of the upper-layer eddy in figure 3.19. The initial position of the eddy is $(0, 20)$.

heton-type motion is more likely to occur for smaller β in the case that the upper-layer eddy has the same strength. The boundary between two motion types in ε-β space is linear. This suggests that this boundary is determined by the time scale on which the upper-layer eddy moves westward, which is proportional to $1/\beta$, and the time scale on which the upper-layer eddy advects the fluid in the lower layer, which is proportional to $1/\varepsilon$. In this model, the lower-layer velocity field has a maximum at $r \approx L_e$ due to the upper-layer eddy, where r is the distance from the centre of the eddy and is zero at the eddy centre in the lower layer. Since the eddy approaches the topography quickly if β is large, it reaches the topography before obtaining a sufficient amount of the high-potential vorticity fluid for the dipole structure to form.

The results obtained in the f-plane show that the heton-like dipole structure can be formed even when ε is small. However, on the β-plane, the region where the dipole is formed is limited within the ε-β space. In the case that the dipole is not formed, the eddy moves onto the shallow side and reaches the western boundary. Thus, this result suggests that the β effect prevents the upper-layer eddy from interacting with the topography and sustains the eastward motion of the dipole structure.

3.5 Summary

In this chapter, the interactions between a Gaussian eddy in the upper layer and a sloping bottom topography in the lower layer were investigated using the quasi-geostrophic system on the f-plane and the β-plane. In particular, we focused on the parameter dependence of the behaviour of the system with the upper-layer eddy and the sloping bottom topography in the lower layer. The results in the f-plane showed that the anticyclonic eddy moves away from the topography while

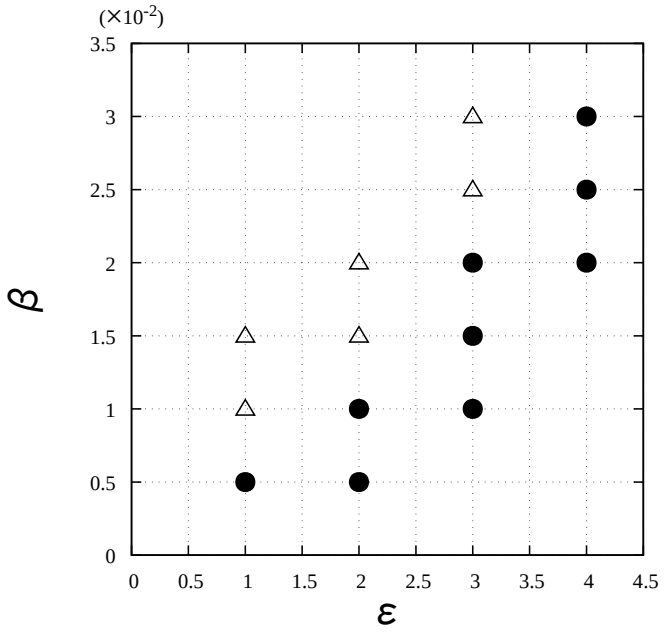

Fig. 3.21: Diagram of the motion classification in the ε-β space. The triangles and circles in the diagram indicate the southwestward and eastward motion of the upper-layer eddy, respectively. The remaining parameters are given by $L_s = 0.5$ and $L_d = 3$.

moving in the opposite direction of the topographic Rossby wave. The behaviour in the direction away from the topography was caused by the formation of the dipole structure consisting of the upper-layer eddy and the isolated eddy in the lower layer. This isolated eddy was generated by the advection of a low-potential vorticity fluid to the deep side of the slope. The motion of the upper-layer eddy with the dipole structure corresponds to the heton-type motion in the previous chapter. The heton-type dipole also occurs even for small ε, since there is always a region where advection due to the upper-layer eddy is dominant on the deeper side of the slope. Thus, the formation of the heton-like dipole structure is a common phenomenon in the interaction between the upper-layer eddy and the sloping bottom topography. Meanwhile, in the case of the cyclonic eddy in the upper layer, the eddy propagates along the topography in the same direction as the topographic Rossby wave, even when the eddy is strong since the presence of the slope width makes it difficult for the upper-layer eddy to advect the low potential vorticity fluid to the shallow side before the lower-layer structure is adjusted by the topographic Rossby wave. In both anticyclonic and cyclonic eddies, the effect of the bottom topography on the eddy approaches that of the step-like topography on the point vortex when the slope becomes steeper and the distance between the eddy and the topography becomes larger. We showed that the upper-layer anticyclonic eddy has two types of motion on the β-plane: southwestward motion over the topography when ε is small or β is large, and eastward motion due to the formation of a heton-like dipole structure when ε is large or β is small. In addition, the dipole formed in the latter case can propagate a long distance to the east, in contrast to the case of the f-plane. Therefore, we can conclude that the β-effect prevents the upper-layer eddy from interacting with the topography and sustains the eastward motion of the dipole structure. The cyclonic eddy in the upper layer propagates northwestward, moving onto the shallow side across the slope region.

Although a dipole structure is temporarily formed when it moves onto the shallow side, the eddy in the lower layer immediately dissipates. Hence, in the case of cyclonic eddies, the β-effect tends to prevents the upper-layer anticyclonic eddy from interacting with the topography, as in the case of anticyclonic eddies.

Chapter 4

Conclusion

Mesoscale eddies play an essential role in material transport. Owing to the westward motion of these eddies, they reach the western boundary and interact with the distinct topography of Western ocean regions, including continental shelves/slopes, thus highlighting the need for a deeper understanding of the interactions between eddies and the steep bottom topography. In this study, we investigated the eddy-topography interactions using two idealised models.

In chapter 2, the interaction between a point vortex in the upper layer and the step-like topography in the lower layer was investigated using a two-layer quasi-geostrophic model in the f-plane. We used a contour dynamics model to formulate the system. We then analytically derived the linear pseudo-image solution in the two-layer system within the limit that the point vortex is weak. We numerically obtained the nonlinear pseudo-image solution, which has a finite amplitude of the potential vorticity front, in the case that the strength of the point vortex is small but non-zero. The finite-amplitude nonlinear pseudo-image solution always has saddle-node points on the potential vorticity front in a coordinate system that moves with the solution. After conducting the numerical experiments in which the nonlinear solution was used as the initial derivation of the front, we

found that the symmetric structure of the front collapsed due to short frontal waves near the saddle-node points. In the numerical experiments with no initial frontal displacement, we showed that the point vortex has two motion types in this system using the strength of the point vortex, ε. The point vortex moves along the topography due to the pseudo-image in the case that ε is small and moves away from the topography due to the formation of a heton-like structure in the case that ε is large. We treated the initial distance, Y_0, as a control parameter and classified the motion types in the ε-Y_0 space. From this classification, we demonstrated that the motion types in this system are the two types mentioned above.

In chapter 3, the interaction between a Gaussian eddy in the upper layer and the sloping bottom topography in the lower layer was investigated using a two-layer quasi-geostrophic model. In the f-plane, the anticyclonic eddies move away from the topography, propagating along the topography in the opposite direction of the topographic Rossby wave. During this motion, the eddy attracts the fluid that is initially on the slope, forming a heton-like dipole structure. Since the heton-like dipole also occurs even for the weak eddy, this motion is a common phenomenon in the interactions between the anticyclonic eddies in the upper layer and the sloping bottom topography in the lower layer. Meanwhile, the cyclonic eddies propagate along the topography in the same direction as the topographic Rossby wave independent of their strength since the potential vorticity anomaly due to the eddy propagates as the topographic Rossby wave and cannot form the dipole structure with the eddy. Further, the motion of the upper-layer eddies was also investigated in the β-plane. On the one hand, the motion types of anticyclonic eddies caused by interacting with the sloping topography are southwestward motion when the strength of the eddy is small or the β-effect is large, and eastward motion due to the heton-like dipole structure when the strength of the eddy is large or the β-effect is small. On the other hand, the cyclonic eddies move onto the slope and north-

westward by the β-effect after entering the shallow side. This motion of cyclonic eddies occurs independent of its strength. These results show that the β-effect prevents eddies in the upper layer from interacting with the bottom topography and sustains the eastward motion of the heton-like dipole.

The results obtained in this study provide fundamental knowledge on the motion of eddies caused by the bottom topography. However, the study has some limitations. First, the conditions for the transitions in the motion types in the parameter space in the f-plane and β-plane (i.e., the condition for the dipole structure to be formed) are still unclear. The findings of this study are the first step towards understanding these transitions. The details of these transitions will be investigated in future work. Second, as the results of this study are obtained based on a variety of assumptions (e.g., the quasi-geostrophic framework, a simple structure of the topography and eddies, and no extra forcing), the applicability of the results to a more realistic environment seems to be restricted. However, the results in this study capture the fundamental processes in the interactions between oceanic eddies and the steep topography to some extent.

Using two idealised models to investigate the interactions between the upper-layer eddies and the steep bottom topography, we revealed the nature of the motion resulting from the interactions and, in particular, showed that the interactions result in the formation of heton-like dipoles. The results suggest that since the western boundary region with high eddy activity typically has a steep bottom topography, mass transport due to the dipole structure may have a non-negligible impact on the near-shore environment. Quantitative discussion of the impact of the dipole structure on the real ocean is left for future work.

Appendix A

Dependence on Initial Condition

In chapter 3, the initial eddy in the upper layer is given by (3.6) and (3.7), that is, the potential vorticity field in the upper layer has the Gaussian profile at the initial time. The initial stream function associated with q_j is obtained by solving

$$\nabla^2\psi_1 - \gamma_L\psi_1 - (\psi_1 - \psi_2) = q_1, \tag{A.1}$$

$$\nabla^2\psi_2 + \gamma_H(\psi_1 - \psi_2) = q_2. \tag{A.2}$$

However, in addition to this, we can choose other initial conditions that provide an eddy in the upper layer. In this appendix, we consider an initial condition that the stream function field in the upper layer has the Gaussian profile and show the behaviour of upper-layer eddies given this initial condition. In particular, we focus on the behaviour on the β-plane. The model configuration and the method of numerical calculation are the same as in chapter 3, except for the initial condition.

We consider the initial condition,

$$\psi_1(t=0,x,y) = -\mathrm{sgn}(\Gamma)\frac{L_e^2}{2}\exp\left(-\frac{(x-X_{c,0})^2+(y-Y_{c,0})^2}{2L_e^2}\right), \tag{A.3}$$

$$q_1(t=0,X_{c,0},Y_{c,0}) = \varepsilon\,\mathrm{sgn}(\Gamma), \tag{A.4}$$

$$q_2(t=0,x,y) = 0, \tag{A.5}$$

where L_e is the non-dimensional radius of an eddy at initial time, and $(X_{c,0}, Y_{c,0})$ is the initial position of the eddy centre. The initial stream function in the lower layer, ψ_2, is obtained by solving (A.1) and (A.2) to satisfy (A.3), (A.4), and (A.5). Figure A.1 shows the initial distribution of q_j, ψ_j and the eddy-induced velocity.

A.1 An anticyclonic eddy

We consider the case of an anticyclonic eddy, that is, $\mathrm{sgn}(\Gamma) = -1$, with $\varepsilon = 1$. Figures A.2 and A.3 show the temporal evolution of the potential vorticity, q_2, and the trajectory of the upper-layer eddy on the β-plane ($\beta = 10^{-2}$). Similar to the results in chapter 3, the weak eddy approaches and then passes the topography due to the β-effect. Figures A.4 and A.5 are the same as figures A.2 and A.3, except that $\varepsilon = 3$. In this case, after approaching the topography, the eddy attracts the low-potential vorticity fluid on the slope, moving eastward with the cyclonic eddy in the lower layer. The structure formed by the interaction between the upper-layer eddy and the topography is similar to the heton-type dipole structure in chapter 3. However, the upper-layer eddy moves westward again since this structure collapses as time elapses. The collapse of this structure is observed even when ε is larger. From figures 3.2 and A.1, it can be seen that the area affected by the upper-layer eddy varies depending on the initial conditions; the area in the present case is much smaller than that in chapter 3. Therefore, the dipole structure may collapse as the upper-layer eddy cannot obtain a sufficient amount of the high-potential vorticity fluid in the lower layer (compare Fig. A.4 with Fig. 3.15). Another possible reason is that the upper-layer eddy has a triple-pole structure after interacting the topography. Although there is a difference in the distance the upper-layer eddy can move eastward, the upper-layer eddy has two types of motion in this system, as in the result of chapter 3.

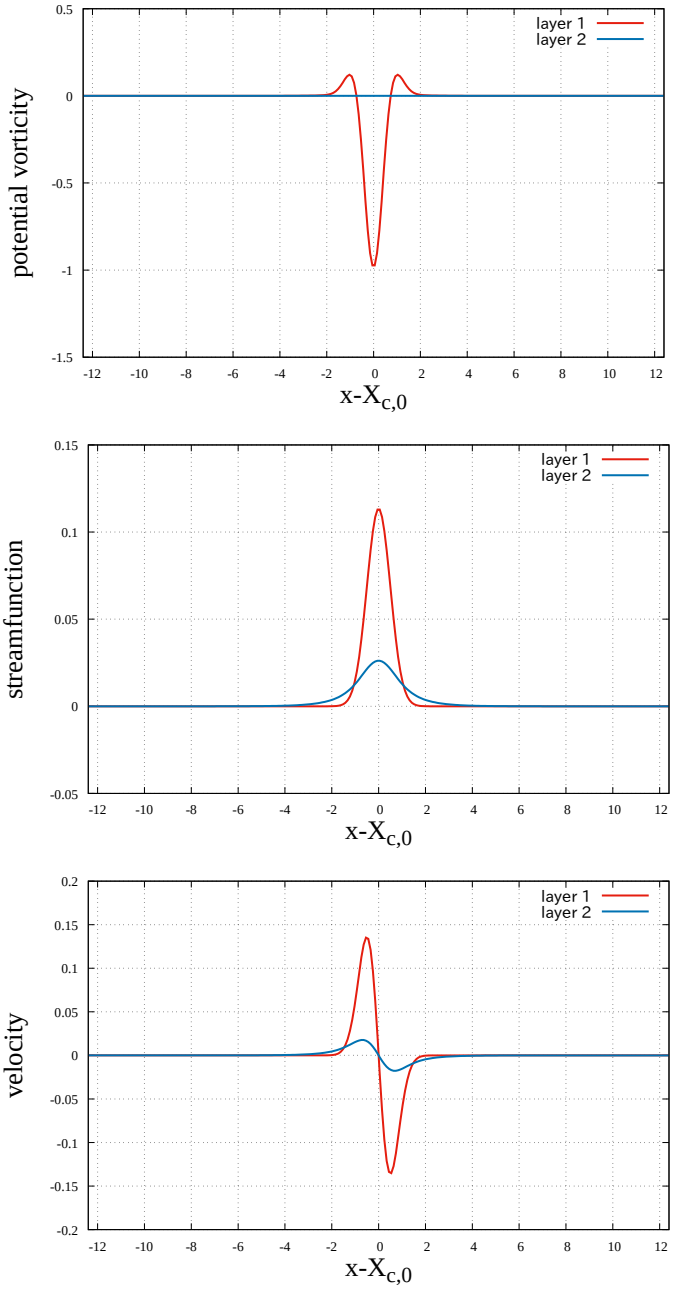

Fig. A.1: Initial profiles of q_j, ψ_j, and the eddy-induced velocity given by (A.3), (A.4), and (A.5) in the section at $y = Y_{c,0}$. The value of $|x - X_{c,0}|$ represents the distance from the eddy centre. The eddy-induced velocity is obtained by $\partial\psi_j/\partial x$. In all panels, the red (blue) lines indicate a profile in the upper (lower) layer. In this case, $\varepsilon = 1$, $L_e = 0.5$, and $(X_{c,0}, Y_{c,0}) = (12.5, 0)$.

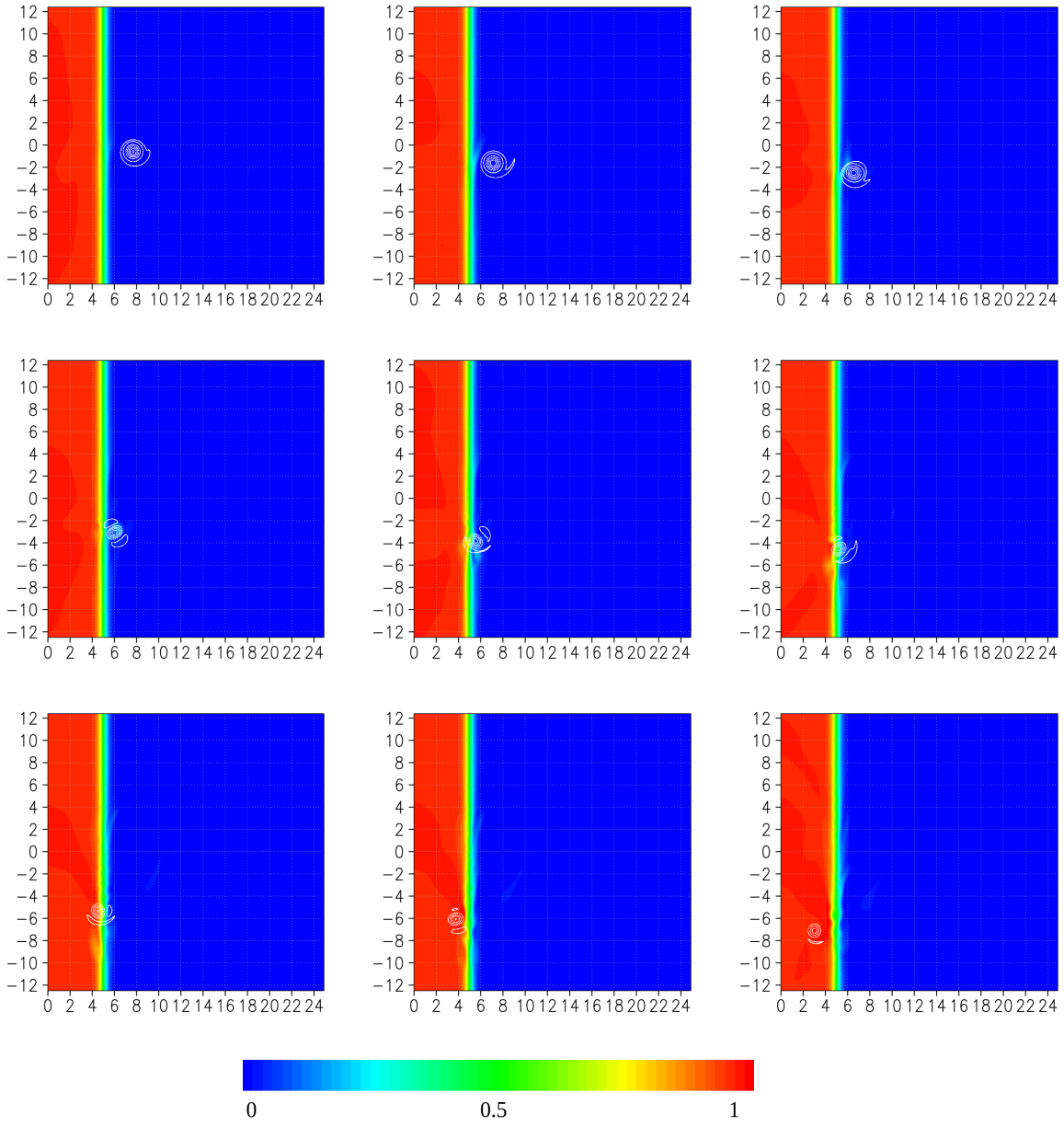

Fig. A.2: The temporal evolution of the potential vorticity field in the lower layer, $q_2 - \beta y$, and the anticyclonic eddy with $\varepsilon = 1$ in the upper layer. White lines indicate the contour of $q_1 - \beta y = -0.9, -0.7, -0.5, -0.3, -0.1, 0.1$. The positive and negative contours are indicated by the solid and dashed lines, respectively. From left to right, (top) $t = 120$, $t = 240$, $t = 360$; (middle) $t = 480$, $t = 600$, $t = 720$; (bottom) $t = 840$, $t = 960$, $t = 1080$. In this case, $x_h = 5$, $L_s = 1$, $L_d = 3$, and $\beta = 10^{-2}$.

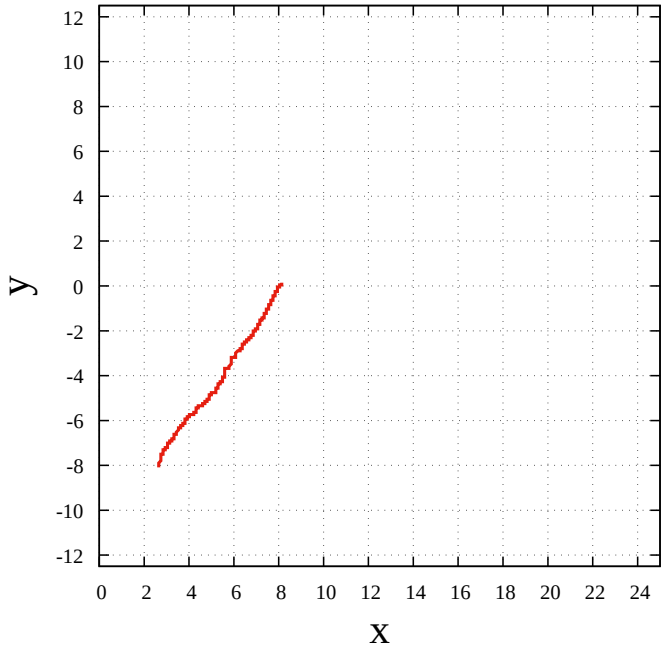

Fig. A.3: The trajectory of the upper-layer eddy in figure A.2. The initial position of the eddy is $(0, 8)$.

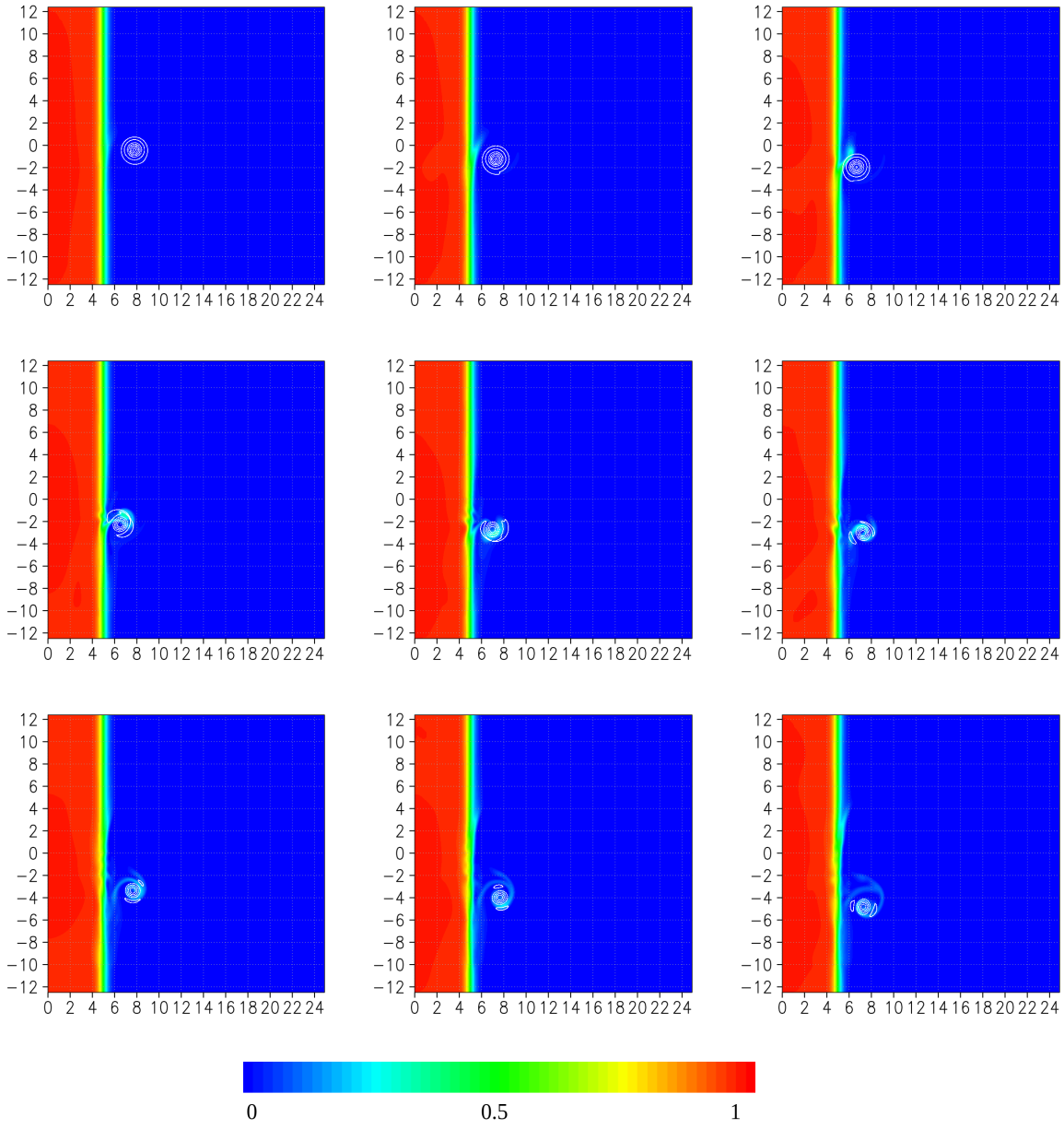

Fig. A.4: The temporal evolution of the potential vorticity field in the lower layer, $q_2 - \beta y$, and the anticyclonic eddy with $\varepsilon = 3$ in the upper layer. White lines indicate the contour of $q_1 - \beta y = -2.7, -2.1, -1.5, -0.9, -0.3, 0.3$. The positive and negative contours are indicated by the solid and dashed lines, respectively. From left to right, (top) $t = 60$, $t = 120$, $t = 180$; (middle) $t = 240$, $t = 300$, $t = 360$; (bottom) $t = 420$, $t = 480$, $t = 540$. In this case, $x_h = 5$, $L_s = 1$, $L_d = 3$, and $\beta = 10^{-2}$.

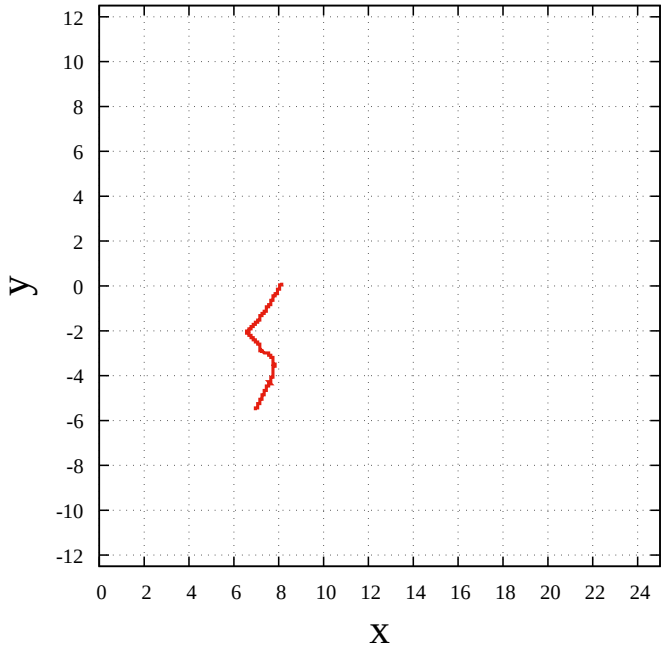

Fig. A.5: The trajectory of the upper-layer eddy in figure A.4. The initial position of the eddy is $(0, 8)$.

A.2 A cyclonic eddy

We consider the case of a cyclonic eddy, that is, $\mathrm{sgn}(\Gamma) = 1$, with $\varepsilon = 3$. Figures A.6 and A.7 show the temporal evolution of the potential vorticity, q_2, and the trajectory of the upper-layer eddy. On both the deep and shallow sides, the upper-layer eddy moves northwestward due to the β-effect. This motion is observed almost independent of ε, as in the result of chapter 3.

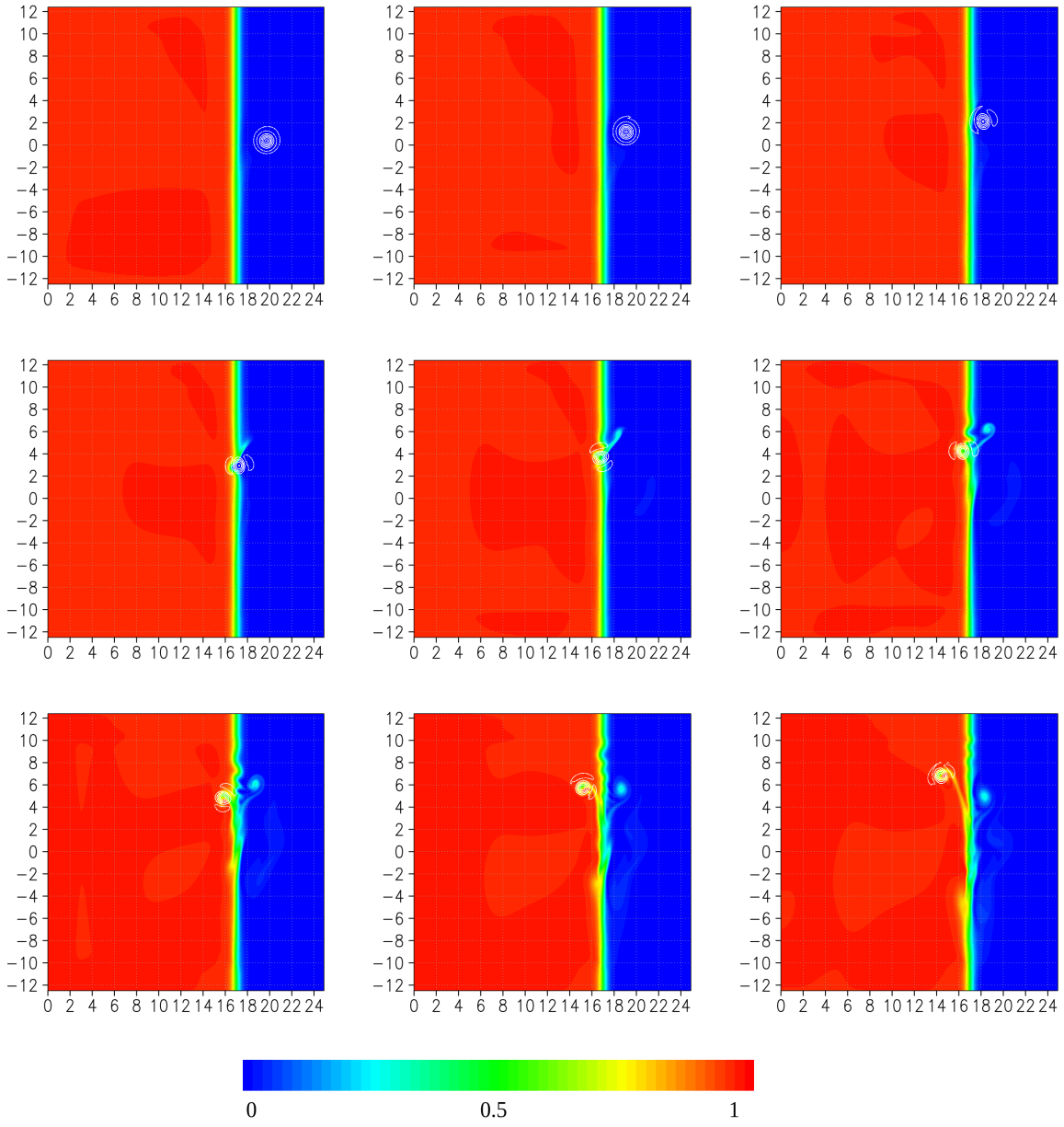

Fig. A.6: The temporal evolution of the potential vorticity field in the lower layer, $q_2 - \beta y$, and the cyclonic eddy with $\varepsilon = 3$ in the upper layer. White lines indicate the contour of $q_1 - \beta y = -0.3, 0.3, 0.9, 1.5, 2.1, 2.7$. The positive and negative contours are indicated by the solid and dashed lines, respectively. From left to right, (top) $t = 60$, $t = 120$, $t = 180$; (middle) $t = 240$, $t = 300$, $t = 360$; (bottom) $t = 420$, $t = 480$, $t = 540$. In this case, $x_h = 5$, $L_s = 1$, $L_d = 3$, and $\beta = 10^{-2}$.

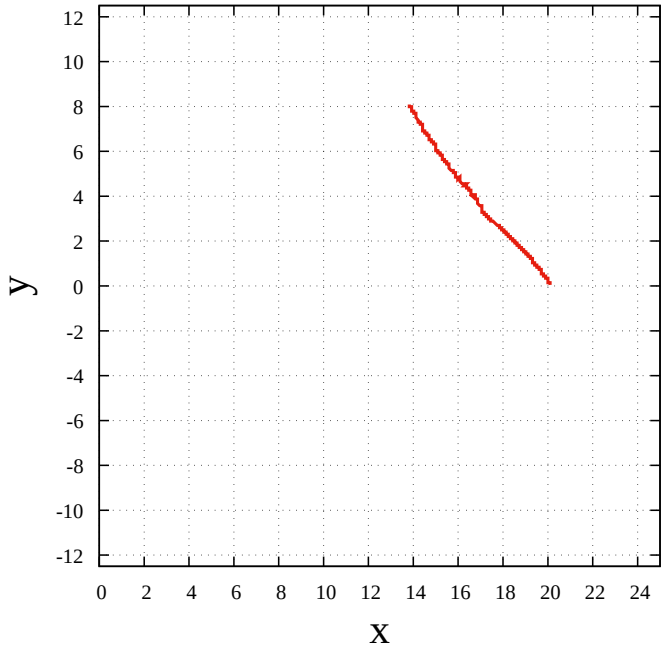

Fig. A.7: The trajectory of the upper-layer eddy in figure A.6. The initial position of the eddy is $(0, 20)$.

Acknowledgements

I would like to express my sincere gratitude to my supervisor, Prof. Atsushi Kubokawa. He supported my research throughout my graduate education with numerous helpful comments and discussions. His support and suggestions made it possible for me to enjoy my research. I would like to thank co-examiners Prof. Humio Mitsudera, Prof. Takeshi Horinouchi, Dr. Genta Mizuta, and Prof. Ichiro Yasuda. Their comments have improved many parts of my research. Prof. Humio Mitsudera and Prof. Ichiro Yasuda provided me with helpful comments on the application of this research to real environments. Prof. Takeshi Horinouchi made insightful comments that are important to deepen this research. Dr. Genta Mizuta provided many valuable comments on the fundamentals of this research, including theoretical and numerical results. I would also like to thank Prof. Koji Shimada for providing us with the contour surgery code.

I want to thank Mr. Yasuhide Kobayashi and Mr. Haruka Onishi. Mr. Yasuhide Kobayashi invited me to the field of geophysical fluid dynamics and showed me how interesting physical oceanography is. I gained a better understanding of physics and mathematics through discussions with Mr. Haruka Onishi. I would like to thank all the people who supported my research.

Finally, I would like to express my deepest gratitude to my mother for all the support and encouragement she has given me.

This research was funded by JST SPRING, Grant Number JPMJSP2119.

Bibliography

Anderson, E., Bai, Z., Bischof, C., Demmel, J., Dongarra, J., Du Croz, J., Greenbaum, A., Hammarling, S., McKenney, A., and Sorensen, D., 1999: LAPACK User's Guide. 3rd ed., Society for Industrial and Applied Mathematics, 407 pp.

Baird, M. E. and Ridgway, K. R., 2012: The southward transport of sub-mesoscale lenses of Bass Strait Water in the Centre of anti-cyclonic mesoscale eddies., *Geophys. Res. Lett.*, **39**, L02603.

Baker-Yeboah, S., Flierl, G. R., Sutyrin, G. G., and Zhang, Y., 2010: Transformation of an Agulhas eddy near the continental slope., *Ocean Sci.*, **6**, pp. 143-159.

Bell, G. I., 1989: Interaction between vortices and waves in a simple model of geophysical flow, *Phys. Fluids A.*, **2** pp. 575-586.

Bell, G. I. and Pratt, L. J., 1992: The Interaction of an Eddy with and Unstable Jet., *J. Phys. Oceanogr.*, **22** pp. 1229-1244.

Chelton, D. B., Schlax, M. G., and Samelson, R. M., 2011: Global observations of nonlinear mesoscale eddies., *Prog. Oceanogr.*, **92** pp. 167-216.

Chen, G., and Han, G., 2019: Contrasting Short-Lived With Long-Lived Mesoscale Eddies in the Global Ocean., *J. Geophys. Res.*, **124** pp. 3149-3167.

Capet, X. J., and Carton, X. J., 2004: Nonlinear Regimes of Baroclinic Boundary Currents., *J. Phys. Oceanogr.*, **34** pp. 1400-1409.

Carton, X., Daniault, N., Alves, J., Cherubin, L., and Ambar, I., 2010: Meddy dynamics and interaction with neighboring eddies southwest of Portugal: Observations and modeling., *J. Geophys. Res.*, **115**, C06017.

de Marez, C., Carton, X., Morvan, M., and Reinaud, J. N., 2017: The Interaction of Two Surface Vortices Near a Topographic Slope in a Stratified Ocean., *Fluids*, **2**, 57.

Dong, C., McWilliams, J. C., Liu, Y., and Chen, D., 2014: Global heat and salt transports by eddy movement., *Nat. Commun.*, **5** pp. 1-6.

Dunn, D. C., McDonald, N. R., and Johnson, E. R., 2001: The motion of a singular vortex near an escarpment., *J. Fluid Mech.*, **448** pp. 335-365.

Dunn, D. C., McDonald, N. R., and Johnson, E. R., 2002: The evolution of an initially circular vortex near an escarpment. Part I: analytical results., *Eur. J. Mech. B Fluids*, **21** pp. 657-675.

Dunn, D. C., 2002: The evolution of an initially circular vortex near an escarpment. Part II: numerical results., *Eur. J. Mech. B Fluids*, **21** pp. 677-699.

Dritschel, D. G., 1988: Contour surgery: A topological reconnection scheme for extended integrations using contour dynamics., *Comput. Phys.*, **77** pp. 240-266.

Everett, J., D., Baird, M. E., Oke, P. R., and Suthers, I. M., 2012: An avenue of eddies: Quantifying the biophysical properties of mesoscale eddies in the Tasman Sea., *Geophys. Res. Lett.*, **39** L16608.

Flierl, G. R, Larichev, V. D., McWilliams, J. C., and Reznik, G. M., 1980: The dynamics of baroclinic and barotropic solitary eddies., *Dyn. Atmos. Oceans*, **5** pp. 1-41.

Frolov, S. A., Sutyrin, G. G., Rowe, G. D., and Rothstein, L. M., 2004: Loop Current Eddy Interaction with the Western Boundary in the Gulf of Mexico., *J. Phys. Oceanogr.*, **34** pp. 2223-2237.

Hogg, N. G. and Stommel, H. M., 1985: The heton an elementary interaction between discrete baroclinic geostrophic vortices, and its implications concerning eddy heat-flow., *Proc. R. Soc. Lond.*, **A 397** pp. 1-20.

Hogg, A. M., Dewar, W. K., Killworth, P. D., and Blundell, J. R., 2003: A Quasi-Geostrophic Coupled Model (Q-GCM)., *Monthly Weather Review*, **131** pp. 2261-2277.

Huang, X. and Wang, G., 2022: Response of a Mesoscale Dipole Eddy to the Passage of a Tropical Cyclone: A Case Study Using Satellite Observations and Numerical Modeling., *Remote Sens.*, **14** 2865.

Hughes, C. W. and Miller, P. I., 2017: Rapid Water Transport by Long-Lasting Modon Eddy Pairs in the Southern Midlatitude Oceans., *Geophys. Res. Lett.*, **44** pp. 12375-12384.

Itoh, S. and Sugimoto, T., 2001: Numerical experiments on the movement of a warm-core ring with the bottom slope of a western boundary., *J. Geophys. Res.*, **106** pp. 26851-26861.

Itoh, S. and Yasuda, I., 2010: Characteristics of Mesoscale Eddies in the Kuroshio–Oyashio Extension Region Detected from the Distribution of the Sea Surface Height Anomaly., *J. Phys. Oceanogr.*, **40** pp. 1080-1034.

Ji, J., Dong, C., Zhang, B., Liu, Y., Zou, B., King, G. P., Xu, G., and Chen, D., 2018: Oceanic Eddy Characteristics and Generation Mechanisms in the Kuroshio Extension Region., *J. Geophys. Res.*, **123**.

Kamenkovich, V. M., Leonov, Y. P., and Nechaev, D. A., 1996: On the Influence of Bottom Topography on the Agulhas Eddy., *J. Phys. Oceanogr.*, **26** pp. 892-912.

Kaneko, H., Itoh, S., Kouketsu, S, Okunishi, T., Hosoda, S., and Suga, T., 2015: Evolution and modulation of a poleward-propagating anticyclonic eddy along the Japan and Kuril-Kamchatka trenches., *J. Geophys. Res.*, **120** pp. 4418-4440.

Kizner, Z., Berson, D., Reznik, G., and Sutyrin, G., 2003: The Theory of the Beta-Plane Baroclinic Topographic Modons., *Geophys. Astrophys. Fluid Dynamics*, **97** pp. 175-211.

Kurian, J., Colas, F., Capet, X., McWilliams, J. C., and Chelton, D. B., 2011: Eddy properties in the California Current System., *J. Geophys. Res.*, **116**. C08027.

Lahaye, N., and Zeitlin, V., 2012: Shock Modon: A New Type of Coherent Structure in Rotating Shallow Water., *Phys. Rev. Lett.*, **108** 04452.

Lutjeharms, J. R. E., and Roberts, H. R., 1998: The Natal Pulse: An Extreme Transient on the Agulhas Current., *J. Geophys. Res*, **93** pp. 631-645.

McDonald, N. R., 1998: Motion of an intense vortex near topography., *J. Fluid Mech.*, **367** pp. 359-377.

McWilliams, J. C., and Flierl, G. R., 1979: On the Evolution of Isolated, Nonlinear Vortices., *J. Phys. Oceanogr.*, **9** pp. 1155-1182.

McWilliams, J. C., Flierl, G. R., Larichev, V. D., and Reznik, G. M., 1981: Numerical studies of barotropic modons., *Dyn. Atmos. Oceans*, **5** pp. 219-238.

McWilliams, J. C., and Zabusky, N. J., 1982: Interactions of isolated vortices I: Modons colliding with modons., *Geophys. Astrophys. Fluid Dynamics*, **19** pp. 207-227.

Mied, R. P., and Lindemann, G. J., 1979: The Propagation and Evolution of Cyclonic Gulf Stream Rings., *J. Phys. Oceanogr.*, **9** pp. 1183-1206.

Moreé, J. J., Garbow, B. S., and Hillstrom, K. E., 1980: User Guide for MINPACK-1, *Technical Report ANL-80-74*, Argonne National Laboratory.

Morel, Y., and McWilliams, J., 2001: Effects of Isopycnal and Diapycnal Mixing on the Stability of Oceanic Currents., *J. Phys. Oceanogr.*, **31** pp. 2280-2296.

Ni, Q., Zhai, X., Wang, G., and Hughes, C. W., 2020: Widespread Mesoscale Dipoles in the Global Ocean., *J. Geophys. Res*, **125**.

Ribbe, J., Toaspern, L., Wolff, J. -O., and Azis Ismail, M. F., 2018: Frontal eddies along a western boundary current., *Cont. Shelf Res.*, **165** pp. 51-59.

Richardson, P. L., and Tychensky, A., 1998: Meddy trajectories in the Canary Basin measured during the SEMAPHORE experiment., *J. Geophys. Res.*, **103** pp. 25029-25045.

Rhines, P. B., 1977: The dynamics of unsteady currents., In *The Sea – Ideas and Observations of Progress in the Study of the Seas.*, ed Goldberg, E. D., McCave, I., O'Brien, J., and Steele, J., Vol 6, pp. 189-318. John Wiley and Sons.

Schaeffer, A., Gramoulle, A., Roughan, M., and Mantovanelli, A., 2017: Characterizing frontal eddies along the East Australian Current from HF radar observations., *J. Geophys. Res.*, **122** pp. 3964-3980.

Serra, N., and Ambar, I., 2002: Eddy generation in the Mediterranean undercurrent., *Deep-Sea Res. II*, **49** pp. 4225-4243.

Serra, N., Ambar, I., and Boutov, D., 2010: Surface expression of Mediterranean Water dipoles and their contribution to the shelf/slope - open ocean exchange., *Ocean Sci.*, **6** pp. 191-209.

Shimada, K., and Kubokawa, A., 1997: Nonlinear Evolution of Linearly Unstable Barotropic Boundary Currents., *J. Phys. Oceanogr.*, **27** pp. 1326-1348.

Smith, D. C., and O'Brien, J. J., 1983: The Interaction of a Two-Layer Isolated Mesoscale Eddy With Bottom Topography, *J. Phys. Oceanogr.*, **13** pp. 1681-1697.

Spall, M. A., Pickart, R. S., Fratantoni, P. S., and Plueddemann, A. J., 2008: Western Arctic shelfbreak eddies: Formation and transport., *J. Phys. Oceanogr.*, **38** pp. 1644-1668.

Stern, M. E., 1975: Minimal properties of planetary eddies., *J. Mar. Res.*, **40** pp. 57-74.

Stern, M. E. and Flierl, G. R., 1987: On the interaction of a vortex with a shear flow., *J. Geo. Res.*, **92** pp. 10733-10744.

Swarztrauber, P. N., 1982: Vectorizing the FFTs., *Parallel Computations*, Academic Press, pp. 51-83.

The MODE Group, 1978: The mid-ocean dynamics experiment., *Deep-Sea Res.*, **25** pp. 859-910.

Wang, X., 1991: Interaction of an eddy with a continental slope., school PhD thesis Massachusetts Institute of Technology/Woods Hole Oceanographic Institution.

White, A. J. and McDonald, N. R., 2004: The Motion of a Point Vortex near Large-Amplitude Topography in a Two-Layer Fluid., *J. Phys. Oceanogr.*, **34** pp. 2808-2824.

Yasuda, I., Okuda, K., and Hirai, M., 1992: Evolution of a Kurosio warm-core ring - variability of the hydrographic structure., *Deep-Sea Res.*, **39** pp. S131-S161.

Vandermeirsch, F. O., Carton, X. J., and Morel, Y. G., 2003: Interaction between an eddy and a zonal jet. Part I. One-and-a-half-layer model. *Dyn. Atmos. Oceans*, **36** pp. 247-270.

Zhang, Y., Pedlosky, J. and Flierl, G. R., 2011: Shelf Circulation and Cross-Shelf Transport out of a Bay Driven by Eddies from an Open-Ocean Current. Part I: Interaction between a Barotropic Vortex and a Steplike Topography, *J. Phys. Oceanogr.*, **41** pp. 889-910.

Zabusky, N. J., Hughes, M., and Roberts, K. V., 1979: Contour dynamics for the Euler equations in two dimensions, *J. Comput.*, **30** pp. 96-106.